



## University of North Dakota UND Scholarly Commons

---

Theses and Dissertations

Theses, Dissertations, and Senior Projects

---

2004

# A Boundary Element Method for Thermo-poroelasticity with Applications in Rock Mechanics

Qiang Zhang  
*University of North Dakota*

Follow this and additional works at: <https://commons.und.edu/theses>



Part of the [Geology Commons](#)

---

### Recommended Citation

Zhang, Qiang, "A Boundary Element Method for Thermo-poroelasticity with Applications in Rock Mechanics" (2004). *Theses and Dissertations*. 332.  
<https://commons.und.edu/theses/332>

This Thesis is brought to you for free and open access by the Theses, Dissertations, and Senior Projects at UND Scholarly Commons. It has been accepted for inclusion in Theses and Dissertations by an authorized administrator of UND Scholarly Commons. For more information, please contact [zeinebyousif@library.und.edu](mailto:zeinebyousif@library.und.edu).

A BOUNDARY ELEMENT METHOD FOR THERMO-POROELASTICITY WITH  
APPLICATIONS IN ROCK MECHANICS

by

Qiang Zhang  
Bachelor of Science, Nanjing University, 1996

A Thesis

Submitted to the Graduate Faculty

of the

University of North Dakota

in partial fulfillment of the requirements

for the degree of

Master of Science

Grand Forks, North Dakota

May  
2004

This thesis, submitted by Qiang Zhang in partial fulfillment of the requirements for the Degree of Master of Science from the University of North Dakota, has been read by the Faculty Advisory Committee under whom the work has been done and is hereby approved.

---

Chairperson

---

---

This thesis meets the standards for appearance, conforms to the style and format requirements of the Graduate School of the University of North Dakota, and is hereby approved.

---

Dean of the Graduate School

---

Date

## PERMISSION

Title            A Boundary Element Method for Thermo-poroelasticity with Applications  
                    in Rock Mechanics

Department    Geology/Geological Engineering

Degree         Master of Science

In presenting this thesis in partial fulfillment of the requirements for a graduate degree from the University of North Dakota, I agree that the library of this University shall make it freely available for inspection. I further agree that permission for extensive copying for scholarly purposes may be granted by the professor who supervised my thesis work or, in his absence, by the chairperson of the department or the dean of the Graduate School. It is understood that any copying or publication or other use of this thesis or part thereof for financial gain shall not be allowed without my written permission. It is also understood that due recognition shall be given to me and to the University of North Dakota in any scholarly use which may be made of any material in my thesis.

Signature \_\_\_\_\_

Date            \_\_\_\_\_

## TABLE OF CONTENTS

LIST OF FIGURES.....	vii
LIST OF TABLES.....	x
ACKNOWLEDGMENTS.....	xi
ABSTRACT.....	xii
CHAPTER	
1. INTRODUCTION.....	1
Thermal-poroelasticity.....	2
Literature Review.....	6
Objectives.....	9
Sign Convention.....	9
2. THERMO-POROELASTICITY.....	10
Assumptions.....	12
Governing Equations For Thermo-poroelasticity.....	12
Constitutive Equations.....	13
Transport Laws.....	14
Balance Laws.....	15
Field Equations for Thermo-poroelasticity.....	15
Field Equations for Poroelasticity and Thermoelasticity.....	16

3.	BOUNDARY ELEMENT METHOD.....	18
	Overview.....	18
	Fictitious Stress Method for Thermo-poroelasticity.....	23
	Boundary Integral Equations.....	24
	Fundamental Solutions.....	26
	Numerical Implementation.....	27
	Displacement Discontinuity Method for Thermo-poroelasticity.....	32
	Boundary Integral Equations.....	33
	Fundamental Solutions.....	34
	Numerical Implementation.....	35
	Combined FS-DD Method for Thermo-poroelasticity.....	36
4.	MODEL VERIFICATION AND TESTING.....	40
	Problem Description.....	40
	Borehole Under Non-hydrostatic Stress Loading.....	42
	Mode 1: Hydrostatic Stress Loading.....	44
	Mode 2: Pore Pressure Loading.....	45
	Mode 3: Deviatoric Stress Loading.....	49
	Borehole Under Thermal Loading.....	53
	Uniformly Pressurized Crack Problem.....	59
	Mode 1: Stress Loading.....	60
	Mode 2: Pore Pressure Loading.....	67
	Crack Under Thermal Loading.....	71

	Maximum Crack Opening.....	72
	Stress Intensity Factor.....	74
	Borehole With Pre-existing Cracks.....	77
	Tangential Stress Near a Borehole Intersected by a Crack.....	77
	Stress Intensity Factor of Cracks Intersecting with a Borehole.....	79
5.	ROCK MECHANICS APPLICATIONS.....	83
	Influence of Borehole Geometry on its Stability.....	83
	Drilling-induced Tensile Failure .....	88
	Influence of Thermal Stress on Injection Well Fracturing.....	91
	Maximum Crack Opening under Poro-thermo-mechanical Loading.....	100
6.	CONCLUSIONS AND FUTURE WORK.....	102
	APPENDICES.....	107
	NOMENCLATURE.....	125
	REFERENCES CITED.....	127

## LIST OF FIGURES

Figure	Page
1. Illustration of thermo-poroelasticity .....	5
2. Discretization in boundary element method.....	19
3. Spatial distribution of point forces on a straight-line segment in the fictitious stress method.....	22
4. Time marching scheme for a continuous heat source.....	29
5. Constant normal and shear displacement discontinuity.....	32
6. Discretization of combined FS-DD method.....	37
7. Circular borehole under non-hydrostatic stress loading.....	43
8. Stresses and pore pressure field under hydraulic stress loading.....	44
9. Pore pressure history at different points under pore pressure loading.....	46
10. Tangential stress field due to pore pressure loading at various times.....	47
11. Radial stress field due to pore pressure loading at various times.....	48
12. Pore pressure field due to deviatoric stress loading at various times.....	50
13. Tangential stress field due to deviatoric stress loading at various times.....	51
14. Radial stress field under deviatoric stress loading at various times.....	52
15. Circular borehole under thermal loading.....	53
16. Temperature field under thermal loading at various times.....	55
17. Pore pressure field under thermal loading at various times.....	56



18.	Tangential stress field under thermal loading at various times.....	57
19.	Radial stress field under thermal loading at various times.....	58
20.	Uniformly pressurized crack.....	59
21.	Short-term crack opening under uniformly stress loading.....	61
22.	Long-term crack opening under uniformly stress loading.....	62
23.	Normalized maximum crack opening under stress loading.....	63
24.	Sketch for stress intensity factor calculation.....	65
25.	Normalized crack stress intensity factor under stress loading.....	66
26.	Crack stress intensity factor under stress loading.....	67
27.	Normalized crack maximum opening under pore pressure loading.....	69
28.	Normalized crack stress intensity factor under pore pressure loading.....	70
29.	Crack stress intensity factor under pore pressure loading.....	71
30.	A crack under thermal loading.....	72
31.	Maximum crack opening under cooling condition, thermo-poroelastic solution.....	73
32.	Maximum crack opening under cooling condition, thermo-poroelastic solution and thermoelastic solution.....	74
33.	Crack stress intensity factor under cooling condition.....	75
34.	Normalized crack stress intensity factor under cooling condition.....	76
35.	Pressurization of a crack intersecting a borehole.....	77
36.	Tangential stress near a borehole intersected by a crack.....	78
37.	A borehole intersected by a crack, under biaxial tension.....	79
38.	A borehole intersected by two cracks, under biaxial tension.....	80

39.	A borehole intersected by two cracks, under internal pressurization on both borehole and crack.....	80
40.	A borehole intersected by two cracks, under internal pressurization on borehole only.....	81
41.	A borehole under combined poro-thermo-mechanical loading.....	85
42.	Effective hoop stress around a circular borehole and an elliptical borehole.....	86
43.	Effective hoop stress around a circular borehole, under poro-mechanical loading.....	87
44.	Effective hoop stress field induced by borehole drilling.....	89
45.	Effective radial stress field induced by borehole drilling.....	90
46.	Hydraulic fracturing of an injection well.....	91
47.	Temperature field around an injection well and a short fracture.....	95
48.	Difference between thermally induced principle stresses around an injection well with a short fracture.....	96
49.	Temperature field around an injection well and a long fracture.....	97
50.	Difference between thermal induced principle stresses around an injection well with a long fracture.....	98
51.	Difference between total principle stresses around an injection well and a short fracture.....	99
52.	Formation of secondary fractures within cooled region.....	99
53.	Maximum crack opening under poro-thermo-mechanical loading.....	101

## LIST OF TABLES

Table	Page
1. Input parameters for Westerly Granite.....	41
2. Stress intensity factor of cracks intersecting with a borehole.....	82
3. Input parameters for Gulf of Mexico Shale.....	85

## ACKNOWLEDGMENTS

I would like to express sincere thanks to the many people who have contributed to the completion of this study. Most of all I would like to thank Dr. Ahmad Ghassemi for his support and guidance through the duration of this work. Dr. Ahmad Ghassemi provided a motivating, enthusiastic, and critical atmosphere during the many discussions we had. It was a great pleasure to me to work with him and conduct this thesis under his supervision. Many thanks to my committee, Dr. Richard LeFever and Dr. Scott F. Korom for the encouragement, advice and assistance throughout the course of my graduate studies. Special thanks go to my family, for their constant love, understanding and many sacrifices, without which would have made this work impossible.

## ABSTRACT

Coupled thermal and poromechanical processes play an important role in many geomechanics problems, such as borehole stability analysis and studies of initiation and propagation of hydraulic fractures. Thermal effects, as well as hydraulic effects, can greatly change the stresses and pore pressure fields around an underground opening. This is due to the fact that thermal loading induces a volumetric deformation because of thermal expansion/contraction of both the pore fluid and the rock solid. Volumetric expansion can result in significant pressurization of the pore fluid. In order to take into account the influence of temperature gradients on pore pressure and stresses, it is necessary to use a non-isothermal poroelastic theory, or thermo-poroelasticity. Many problems formulated within the framework of thermo-poroelasticity are not amenable to analytical treatment and need to be solved numerically. The boundary element method (BEM) has proven suitable for the poroelastic and thermoelastic problems. In this thesis, a two-dimensional transient indirect BEM is developed to solve coupled thermo-poroelastic problems.

The indirect BEM has two sub-formulations, namely, the displacement discontinuity (DD) method and the fictitious stress (FS) method. The DD method has shown to be particularly suitable for crack-shaped problems (Crouch and Starfield, 1983). A combine FS-DD model is developed to take advantage of the strengths of both FS and

DD methods. The boundary integral equations, fundamental solutions, and the numerical implementations for the development of this model are described. The model is tested using some poroelastic and thermo-poroelastic examples. The numerical predictions show good agreement with analytical solutions or previously published results. The results indicate that the transient formulation of the indirect BEM (FS-DD) model is an accurate and suitable means for solving problems in thermo-poroelasticity.

In addition to verification of the numerical techniques, the model is applied to borehole stability and fracture problems in high temperature underground environments. Drilling-induced stress and pore pressure distributions around a borehole are analyzed. Effects of thermal loading and pore pressure loading are considered. The results indicate that cooling the borehole wall will induce a pore pressure reduction and additional tensile stresses in the formation. Therefore, the potential for tensile fracture at the wall and inside the rock increases. The influence of excavation geometry on borehole stability under combined poro-thermo-mechanical loading is also considered. It is found that an elliptical borehole will be more likely to fail in tension due to the pressure of the mud column and cooling. The examples also indicate that cooling increases crack opening and stress intensity, leading to crack growth. Fracturing is more likely to occur in the cooled zone. In general, cooling at the borehole wall can lead to fracturing and instability; cooling the crack surface can cause the crack to open up and further propagate. Pore pressure effects in these problems are far less important than thermal effects according to the study. However, thermal effects tend to develop slowly and can be neglected in hydraulic fracture propagation.

## CHAPTER 1

### INTRODUCTION

The stability of underground openings is of interest in geological, mining and petroleum engineering as well as many other disciplines. One of the major applications is the borehole stability analysis in the energy industry. Extraction of oil, gas and geothermal resources requires drilling through rock formations. Drilling operations can be costly and risky because of various geomechanical problems related to borehole instability. The practical consequences of borehole instability are often the collapse of borehole wall in shear or lost circulation caused by fracturing of the borehole. In the petroleum industry, it is estimated that at least 10% of the average well budget is used on unplanned operations resulting from borehole instability. This cost may approach one billion dollars per year worldwide (Aadnoy and Ong, 2003).

Having a good understanding of the mechanical behavior of the borehole and surrounding rock formation is the key points for borehole stability analysis. In the petroleum industry, the common practice of stress analysis around borehole uses classic theory of elasticity [e.g. Bradley, 1979]. Models based on this theory are popular because they assume the rock is a linear elastic continuum and thus are relatively easy to implement and require a modest number of input parameters. Factors contributing to borehole instability, such as trajectory of the borehole, orientation and magnitude of the

in-situ stress field, and rock properties, are normally considered in the analyses. Stresses computed from the model are compared to a rock strength criterion to determine if shear failure or tensile failure will occur. In addition to failure of the intact rock, borehole failure can also be initiated along pre-existing natural discontinuities, such as bedding planes and fractures, in rock masses. This factor has also been considered in some borehole stability models within the framework of elasticity.

#### Thermo-poroelasticity

Due to the complexity of the rock formation, in many cases pure elastic models alone are inadequate to provide accurate stress analysis. One of the reasons is because rock, as a porous medium, is usually saturated with fluid. Drilling in fluid saturated rock disturb the initial state of pore pressure. The stress analysis must take into account the influence of pore pressure gradient induced by fluid flow and those by induced stresses. In addition, pore pressure changes induce stress in the rock. The first detailed studies of the coupling between the fluid pressure and solid stress fields were described by Biot (1941). In the poroelastic theory, the time dependent fluid flow is incorporated by combining the fluid mass conservation with Darcy's law; the basic constitutive equations relate the total stress to both the effective stress given by deformation of the rock matrix and the pore pressure arising from the fluid. From then on, the theory of poroelasticity has been developed by a number of investigators (e.g. Geertsma, 1957; Rice and Cleary, 1976). The coupled poroelastic effects can be summarized as follows (Vandamme et.al, 1989):



- (1) a volumetric expansion of the porous rock is induced by an increase of the pore pressure;
- (2) if the fluid is prevented from escaping (undrained condition), an increase of the pore pressure results from the application of a confining pressure;
- (3) the volumetric deformation of the rock is sensitive to the rate of isotropic loading (the rock appears to be stiffer under faster loading rates).

Another factor that plays an important role in borehole stability is the temperature variations. In many situations, there is a significant temperature difference between the drilling mud and the formation. This thermal loading on the borehole wall can induce additional stresses and pore pressure around the borehole. Thermally induced stresses have attracted the attention of many researchers in the context of thermoelasticity (e.g. Carslaw and Jaeger, 1959; McTigue, 1986). However, thermal induced pore pressure change is not considered in this theory.

As mentioned above, the practice of drilling causes perturbations of the initial stresses, pore pressure and temperature equilibriums. Hydraulic and thermal gradients developed between the drilling mud and the formation result in a modification of the stress state near the borehole. Therefore, it is necessary to consider both the hydraulic effects and the thermal effects in borehole stress analysis. In order to achieve this goal, the theory of thermal-poroelasticity is developed on the basis of poroelasticity by coupling the time-dependent processes of fluid diffusion and heat diffusion to the mechanical behavior of the rock. Constitutive equations for this theory were first introduced by Palciauskas and Domenico (1982) by extending the classic Biot's

poroelastic theory for the non-isothermal case. Whereas the equations of poroelasticity are fully coupled, in the sense that the pore pressure influences the deformation and the deformation influences the pore pressure, coupling in thermoelasticity is usually unidirectional. Temperatures will have a large influence on the stresses and strains, but the deformation does not lead to significant temperature change. This is also the case when one looks at the relationship between pore pressure and temperature. So, temperature field and heat flux can usually be calculated independently. The relationships of these three main components in thermo-poroelasticity are indicated in Figure 1.

It should be noted that convective heat transport is often neglected in low permeable rocks like shale and granite. This is because in such rocks heat conduction dominates the heat transfer process and heat convection is negligible due to the extremely low fluid flow velocity. This approach has been justified by Delany (1982).

A few analytical procedures have been developed and used to solve geomechanics problems of interest involving coupled thermal and poromechanical problems (Ghassemi and Diek, 2002; Wang and Papamichos, 1994). However, many problems formulated within the framework of thermo-poroelasticity are not amenable to analytical treatment and need to be solved numerically. The boundary element method (BEM) or the boundary integral equation formulation has been used extensively for the poroelastic and thermoelastic problems (e.g., Cheng et al. 2001; Ghassemi et al. 2001). The advantage of the method is that it reduces the problem dimensionality by one, thereby reducing the computational efforts significantly. There are two types of BEM formulations: direct and indirect. In the former, the unknowns in the integral equations are physical variables (e.g.

displacements or stresses). It is realized by using the reciprocal theorem. In contrast, the unknowns in the indirect BEM are fictitious terms which usually do not represent the physical variables of the problem. The indirect approach can be developed based on the principle of superposition or using a rigorous mathematical approach.

The indirect BEM has two sub-formulations, namely, the displacement discontinuity (DD) method and the fictitious stress (FS) method. The former is particularly useful for modeling fractures and fracture propagation. Its advantages stem from the fact that in this method the two surfaces of a thin crack are treated as one entity, and the relative displacements between these surfaces are the unknown physical parameters.

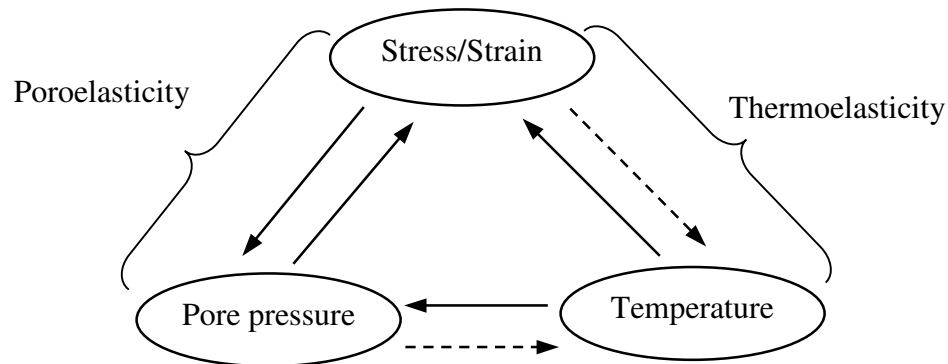


Figure 1. Illustration of thermo-poroelasticity

Although the coupled diffusion-deformation problems are essentially three-dimensional (3-D), they can be analyzed in 2-D using the concept of plane strain as long as the length of the excavation is much larger than its dimension in the plane

perpendicular to its axis. The plane strain concept can also be used when the long axis of the opening is not in the direction of a principle stress (Cheng, 1998; Ghassemi et al., 2001), which is often practiced in engineering. In this thesis, a plane strain 2-D indirect boundary element model is developed and applied to a number of transient thermo-poroelastic problems.

### Literature Review

Analysis of mechanical failure of underground openings has been the subject of rock mechanics for a long time. As one of the major applications, during the last two decades, the borehole stability issue has been seriously addressed due to the increasing complexity of drilling operations by the petroleum and gas industry.

Drilling into a deeply buried rock formation involves perturbation of the natural stresses around the drilled zone. To examine the borehole stability, the stress and pore pressure fields around the well must be determined. Assuming linear elastic material behavior, equations for stress distributions around a circular hole are given by various authors (e.g., Timoshenko and Goodier, 1951; Jaeger and Cook, 1979). Numerous borehole stability models have been proposed based on the theory of linear elasticity, e.g. Bradley (1979), Aadnoy and Chenevert (1987), and Hsaio (1987). However, these traditional models are inadequate for fluid saturated rocks because they do not take into account the poroelastic and thermal effects.

Biot (1941) developed the theory of linear poroelasticity to study coupled diffusion-deformation phenomena in porous media. This theory was later reformulated by Rice and Cleary (1976), who presented the poroelasticity with parameters used in rock

and soil mechanics. The coupling phenomena between the pore pressure and rock stress changes are discussed under undrained and drained conditions by Rice and Cleary (1976) and later by Detournay and Cheng (1988). Detournay and Cheng (1993) applied poroelasticity to a number of problems in petroleum and civil engineering. Detournay and Cheng (1988) and Cui et al. (1995, 1997) introduced poroelastic effects to investigate the stability of vertical and inclined wells, respectively. With the reduction of pore pressure around the borehole, the effective stress becomes more compressive, thus the potential of compressive failure at the wall increases. Fluid flow into the formation induces pore pressure rise and an effective tensile stress zone around the borehole, which implies a higher potential of tensile failure. It was also found that shear failure could be initiated inside the rock rather than at the borehole wall due to deviatoric stress loading, as is predicted on the basis of an elastic analysis (Detournay and Cheng, 1988).

Thermal stresses develop when there are differences in temperature between formation and borehole fluids. Thermal stresses have also been examined by a number of researchers, e.g., Carslaw and Jaeger (1959) and McTigue (1986). The latter studied several problems of thermal loadings of a fluid-saturated porous media. The contribution of the thermal effects to fluid flow and rock deformation is considered using a linear non-isothermal poroelastic theory. Kurashige (1989) developed a theory that fully couples heat transfer to the poroelastic process. Coussy (1991), Wang and Papamichos (1994), and Li et al. (1998) among others applied the theory of thermo-poroelasticity in borehole stress analysis (Wolfe, 2002). Ghassemi and Diek (2002) extended this theory to include the influence of a chemical potential in a nonisothermal setting. Borehole stability and

time-delayed formation failure under cooling or heating conditions are discussed. Heating increases the potential of shear failure, because the volume expansion during heating increases the compressive stress as well as the stress difference. Cooling increases the potential of tensile failure because of the tensile stress induced by material shrinkage. It was found that with cooling, a tensile stress zone would develop inside the formation with time, which can facilitate the time-delayed fracture growth.

Due to geometric complexity, many problems formulated within the framework of thermo-poroelasticity do not have analytical solutions, e.g., when studying elliptical boreholes and boreholes intersected by fractures. This calls for the development of numerical solutions.

The applications of boundary element method in poroelastic and thermoelastic problems can also be found in literature. Direct and indirect boundary element methods for poroelasticity have been presented by Ghassemi et al. (2001), Cheng and Detourney (1988), and Curran and Carvalho (1987), respectively. Prasad et al. (1996) developed a dual boundary element method for transient thermoelastic crack problems. Green's functions for a fully coupled thermo-poroelasticity have been presented by Smith and Booker (1993) in the Laplace space. Transient BEM has the following advantages: first, it is relatively easy to formulate since Laplace transform inversion is avoided in this method; second, it is suitable for simulations of problems in which the problem boundary changes with time such as crack propagation. However, there are no transient indirect boundary element methods for thermo-poroelasticity.

## Objectives

The objective of this thesis is to develop a two dimensional transient indirect Boundary Element Method (BEM) to solve coupled thermo-poroelastic problems. Two sub-formulations of the indirect BEM, both displacement discontinuity (DD) model and fictitious stress (FS) model are developed in order to treat different problems. To further examine the interactions of an underground opening and fractures under thermo-hydro-mechanical loading, the two models are combined into one mixed FS-DD model.

The model for poroelasticity is developed first; then, the influence of temperature gradient is added in to make it a thermo-poroelastic model. The model is verified by various cases and compared with published results by other researchers. At last, several applications in geomechanics are studied.

## Sign Convention

Most previously published papers concerning poroelasticity and thermo-poroelasticity consider tensile stress as positive. However, in rock mechanics, compressive stresses are generally considered as positive for the convenience of engineering use. In this thesis, in order to be consistent with the thermo-poroelasticity literature, all equations are presented using the tension positive convention, whereas all graphics are plotted with the compressive positive convention used in rock mechanics. This sign convention is adopted for the remainder of this thesis unless otherwise specified.

## CHAPTER 2

### THERMO-POROELASTICITY

Drilling can cause temperature contrasts between the formation and the borehole because of the drilling fluid circulation. This results in heat transfer into or out of the formation, which may be referred to as thermal loading. In a fluid-saturated porous rock, thermal loading can significantly alter the surrounding stress field and pore pressure field. Thermal loading induces volumetric deformation because of thermal expansion/contraction of both the pore fluid and the rock solid. If the rock is heated, expansion of the fluid can lead to a significant increase in pore pressure when the pore space is confined. The tendency is reversed in the case of cooling. Therefore, the time-dependent poromechanical processes should be fully coupled to the transient temperature field. This can be studied in the framework of thermo-poroelasticity.

In order to study the pore pressure and stress field under the thermal and poromechanical loading, the theory of thermo-poroelasticity was first developed by Palciauskas and Domenico (1982). This theory was later established by other investigators, e.g., McTigue (1986), and Coussy (1991). They introduced the constitutive equations by extending the Biot's poroelastic theory for the non-isothermal case. The transient heat transfer process is coupled with the poroelastic behavior in the theory.



Although heat transfer can result in significant changes in pore pressure and volumetric stress, influences of fluid and rock matrix deformation on the temperature field are usually negligible. This means that heat flux and temperature can be calculated separately without the contribution of pore pressure and stresses.

From the foregoing discussion, the three mechanisms that play a key role in the thermo-poroelastic process are:

- (1) an increase of pore pressure induces volumetric deformation of the rock;
- (2) rock compression leads to a rise in pore pressure;
- (3) heating of the rock increases pore pressure and volumetric stresses.

Due to the time dependency of both fluid diffusion and heat conduction, the changes of pore pressure and stress fields are transient processes. Undrained and drained deformations are two limiting behaviors for a fluid-saturated material. The undrained response characterizes the case when there is no fluid moving out of the porous solid. This denotes the instantaneous behavior of a poroelastic material under a suddenly applied loading. Pore pressure change is exclusively related to the variation of pore volume under isothermal conditions and also to a mismatch of the thermal expansivity of fluid and bulk solid under non-isothermal conditions (Berchenko, 1998). While the drained response characterizes the long-term behavior when the pore pressure vanished everywhere or has reached steady-state conditions.

## Assumptions

It should be noted that for rocks with low permeability, heat conduction dominates the heat transfer process. This has been confirmed by Delaney(1982). Heat convection can usually be neglected because of the extremely low fluid flow velocity in such rocks. This thesis is concerned with low permeable rocks like shale and granite only, so effects of heat transported by convection are neglected and linear thermal conductive behavior is assumed in the thermo-poroelastic analysis.

The theory of thermo-poroelasticity incorporates the typical linear elastic assumptions as well as the following ones:

- Homogeneous, isotropic, infinite porous medium
- Constant material parameters
- Transient fluid flow governed by Darcy's Law
- Fluid pressure acts equally in all directions
- No shear stress at the interface of pore fluid and the rock matrix
- Transient linear heat conduction

## Governing Equations For Thermo-poroelasticity

The governing equations for thermo-poroelasticity can be found in the works of McTigue (1986) and Coussy (1991). Following is a brief review of the equations, which consist of constitutive equations, transport laws and balance laws.

### Constitutive Equations

In isotropic thermo-poroelasticity, the constitutive equations can actually be separated into a deviatoric response and a volumetric one. The later includes volumetric response of the solid matrix and the fluid.

Deviatoric response is given by:

$$\varepsilon_{ij} = \frac{\sigma_{ij}}{2G}, i \neq j \quad (1)$$

where  $\varepsilon_{ij}$  denotes the components of the deviatoric strain tensor,  $\sigma_{ij}$  denotes the components of the deviatoric strain stress tensor, and  $G$  is the shear modulus. Throughout this thesis, subscript indices  $i$  and  $j$  have values in the range  $\{1,2\}$  and the summation convention is used over repeated indices.

The volumetric response of the solid contains both hydraulic and thermal coupling terms:

$$\varepsilon_{kk} = \frac{\sigma_{kk}}{3K} + \frac{\alpha p}{K} + \beta_s T \quad (2)$$

where  $\varepsilon_{kk}$  is volumetric strain, also denoted as  $\varepsilon$ ,  $\frac{\sigma_{kk}}{3}$  is volumetric stress (mean stress),  $p$  is pore pressure change,  $T$  is temperature change. The constant  $K$  is the rock's bulk modulus;  $\alpha$  is Biot's effective stress coefficient and can be computed using  $\alpha = 1 - (K/K_s)$ , where  $K_s$  is the bulk modulus of solid grains;  $\beta_s$  is the volumetric thermal expansion coefficient of the bulk solid under constant pore pressure and stress. Note that without the pore pressure term and temperature term, equation (2) degenerates to the classical elastic relation.

Equation (2) can also be written as a stress form:

$$\sigma_{ij} = 2G\varepsilon_{ij} + \frac{2G\nu}{1-2\nu}\varepsilon_{kk}\delta_{ij} - \alpha p\delta_{ij} + K\beta_s T\delta_{ij} \quad (3)$$

in which  $\nu$  is Possion's ratio.

The volumetric response of the fluid can be written as:

$$\zeta = \frac{\alpha}{3K}\sigma_{kk} + \frac{\alpha p}{BK} - n(\beta_f - \beta_s)T \quad (4)$$

where  $\zeta$  is the variation of the fluid content per unit volume of the porous material (Biot, 1941),  $B$  is Skempton's pore pressure coefficient,  $\beta_f$  is volumetric thermal expansion coefficient of the fluid and  $n$  is porosity. Physical meaning of  $B$  is the increase in pore pressure due to an increase of mean stress under isothermal undrained condition ( $\zeta = 0$ ).

Equation (4) can also be written in term of pore pressure:

$$p = M(\zeta - \alpha\sigma_{kk} + \beta_m T) \quad (5)$$

where  $M$  is the Biot modulus given as  $M = \frac{BK}{\alpha(1-B\alpha)}$ ,  $\beta_m$  is hydro-thermal expansion

coefficient given as  $\beta_m = \alpha\beta_s + n(\beta_f - \beta_s)$ .

### *Transport Laws*

The transient fluid flow in porous rocks is governed by the well-known Darcy's law, which can be described as:

$$q_i = -k\mathcal{P}_{,i} \quad (6)$$

where  $q_i$  is the fluid flux (units of fluid volume per unit area);  $\kappa$  is defined as  $\kappa = k / \mu$  ( $k$  is the intrinsic permeability having dimension of length squared, and  $\mu$  the fluid dynamic viscosity).

The heat flow is governed by Fourier law, which is written as:

$$q_i^T = -\kappa^T T_{,i} \quad (7)$$

where  $q_i^T$  is the heat flux,  $\kappa^T$  is the thermal conductivity.

One can see that the transport laws for fluid flow and heat flow are analogous to each other.

### *Balance Laws*

For local stress balance, standard considerations of static equilibrium lead to the equilibrium equation used in elasticity:

$$\sigma_{ij,j} = 0 \quad (8)$$

Considerations of mass conservation for a compressible fluid yield the local continuity equation:

$$\frac{\partial \zeta}{\partial t} + q_{i,i} = 0 \quad (9)$$

## Field Equations For Thermo-poroelasticity

From the constitutive, balance, and transport laws, the field equations can be derived for temperature  $T$ , displacement  $u_i$ , and pore pressure  $p$ :

Navier Equation:

$$G\nabla^2 u_i + \frac{1}{3}(G + 3K)\epsilon_{,i} = \alpha p_{,i} + K\beta_s T_{,i} \quad (10)$$

Diffusion equation for pore pressure  $p$ :

$$\kappa\nabla^2 p = \frac{1}{M} \frac{\partial p}{\partial t} + \alpha \frac{\partial \epsilon}{\partial t} - \beta_m \frac{\partial T}{\partial t} \quad (11)$$

Diffusion equation for temperature  $T$ :

$$c^T \nabla^2 T = \frac{\partial T}{\partial t} \quad (12)$$

In the above equations,  $u_i$  denotes the solid displacement vector,  $\epsilon_{ij}$  the total strain tensor,  $p$  the pore pressure change, and  $T$  the temperature change. The constant  $c^T$  represents thermal diffusivity.

As mentioned above, heat transfer is calculated separately because stress and pressure changes do not significantly alter the temperature field. Also, note that convective heat transport is neglected.

Totally ten independent parameters are needed for thermo-poroelastic theory, they are  $\{K, G, \alpha, B, \kappa, \beta_s, \beta_f, c^T, \kappa^T, \gamma_f\}$ . Among them, five parameters  $\{K, G, \alpha, B, \kappa\}$  are from poroelasticity, with  $\{K, G\}$  as the pure elastic parameters.

## Field Equations for Poroelasticity and Thermoelasticity

Poroelasticity and thermoelasticity can be considered as two special cases for thermo-poroelasticity. Derivations of field equations for isothermal poroelasticity can be found in the literature (e.g. Detourney and Cheng, 1993). These equations can also be obtained from the thermo-poroelastic ones by neglecting the thermal effect.

Letting  $T = 0$  in equation (10) and (11), one can get the field equations for poroelasticity:

Navier Equation for solid displacement:

$$G\nabla^2 u_i + \frac{1}{3}(G + 3K)\epsilon_{,i} = \alpha p_{,i} \quad (13)$$

Diffusion equation for pore pressure  $p$ :

$$\kappa\nabla^2 p = \frac{1}{M} \frac{\partial p}{\partial t} + \alpha \frac{\partial \epsilon}{\partial t} \quad (14)$$

Similarly, neglecting the pore pressure term from the field equations of thermo-poroelasticity will result in field equations for thermoelasticity:

Navier Equation:

$$G\nabla^2 u_i + \frac{1}{3}(G + 3K)\epsilon_{,i} = K\beta_s T_{,i} \quad (15)$$

Diffusion equation for temperature  $T$  is the same as the thermo-poroelastic equation (12) because actually no pore pressure and stress effects are considered.

Derivations of thermoelasticity equations and poroelasticity equations are parallel. The analogies between these two theories have been discussed in references (Rice and Cleary, 1976; Norris, 1992).

## CHAPTER 3

### BOUNDARY ELEMENT METHOD

#### Overview

Thermo-poroelastic problems, as well as poroelastic and thermoelastic ones, can be described by a set of partial differential equations mentioned above. Unfortunately, analytical solutions for coupled diffusion-deformation problems exist only for very simple problems. In general the geometry and boundary conditions of real problems are quite complex and require the use of numerical methods.

Boundary element method (BEM) is a powerful numerical tool for solving systems governed by linear partial differential equations (Brebbia et al., 1984). It has been used extensively for the poroelastic and thermoelastic problems (e.g., Cheng et al. 2001; Ghassemi et al. 2001). BEM is based on fundamental solutions, which are analytical solutions corresponding to some sort of singular impulse at a point in an infinite region. For example, in solid mechanics, the impulse can represent a point force applied within an elastic solid. The impulse could also represent a point fluid source, a point heat source or a displacement discontinuity in different problems. The fundamental solutions are also called singular solutions because, mathematically speaking, they are well behaved everywhere in the region except at the point of the impulse, where there is a mathematical singularity.



Partial differential equations plus certain conditions specified on the boundary of region of interest,  $R$ , enclosed within a boundary  $\Gamma$ , defines a boundary value problem. Other than finite difference and finite element methods which make approximations on the whole region  $R$ , BEM makes approximations only on the boundary  $\Gamma$  by dividing it into  $N$  elements, as shown in Figure 2 (after Crouch and Starfield, 1983). Singular impulses (e.g. point force, heat source, fluid source, or displacement discontinuity) are distributed on the elements along the boundary so that the combined effects of all the impulses satisfy the prescribed boundary conditions. At any one element, combined effects of all  $N$  singular impulses can be expressed in terms of the strengths of the impulses. Therefore, a system of  $N$  linear algebraic equations can be written down, in which the unknowns are the strengths of the impulses. Once these equations have been solved, the solution at any point in  $R$  can be constructed.

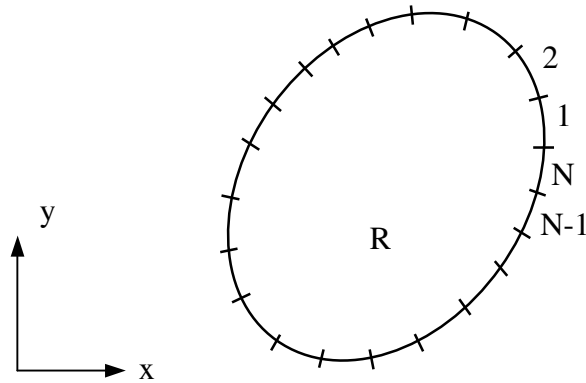


Figure 2. Discretization in boundary element method

The main advantage of BEM is that the boundary-only discretization significantly simplifies modeling. The system of equations need to be solved is much smaller than the system needed to solve the same boundary value problem by finite element method. However, this smaller system of equations is no longer sparse as each singular impulse plays a part in every equation (Crouch and Starfield, 1983). Another major advantage is that BEM can generate solutions at *any* point in the region  $R$ , instead of a number of fixed mesh points in finite element method. This is because BEM exploits analytical solutions that hold true for the whole region. Therefore, BEM is potentially more accurate than finite element method, where approximations are made in every subdivision of  $R$  (Crouch and Starfield, 1983).

The boundary element method can be of direct and indirect nature. The direct method is from integral equations based on the generalized Green's theorem, which are sometimes expressed in the form of an energy reciprocity theorem (Cheng and Detournay 1998). Solution of the integral equations for the elements into which a boundary is discretised directly yields the desired values of the unknown variables on the boundary.

In the indirect method, singular impulses (e.g., point force, heat source, fluid source, or displacement discontinuity) are distributed on the elements along the boundary so that the combined effects of all the impulses satisfy the prescribed boundary conditions. At any one element, combined effects of all  $N$  singular impulses can be expressed in terms of the strengths of the impulses. Therefore, a system of  $N$  linear algebraic equations can be written down, in which the unknowns are the strengths of the impulses.

The indirect methods are based on the distribution of influence functions such as source, point force, etc. with “fictitious densities”. They can be determined from the boundary integral equations for a set of prescribed boundary conditions. Displacements and stresses on the boundaries, as well as in the domain, can then be obtained indirectly from the fictitious variables.

The indirect form as applied to the problems of our interest has two sub-formulations, namely, the *fictitious stress method* (FSM) and the *displacement discontinuity method* (DDM). The fictitious stress method is based on the analytic solution of a point force in an infinite solid. It is a versatile method of modeling underground openings of arbitrary shape. The displacement discontinuity method makes use of the fundamental solution for a constant discontinuity of displacement in an infinite solid. The displacement jump inherent in the fundamental solution of displacement discontinuity method are not fictitious quantities, this makes it a natural choice for modeling fractures. The fictitious stress method is not suitable for such problems, because the effects of elements placed along one crack surface are indistinguishable from the effects of elements placed along the other surface (Crouch and Starfield, 1983).

When developing the fictitious stress boundary element method for thermo-poroelasticity, fundamental solutions for a *point force*, a fluid source and a heat source are needed. The displacement discontinuity method requires fundamental solutions for a *displacement discontinuity*, a fluid source and a heat source. The fundamental solutions are integrated over a desired element shape to form the building block of each method.

Since the formulation of displacement discontinuity method is exactly the same with the fictitious stress method, only the former is described in detail in this thesis.

In order to model problems with both underground openings and fractures, fictitious stress method and displacement discontinuity method can be combined in one model, due to the fact that they share the same structure of formulation.

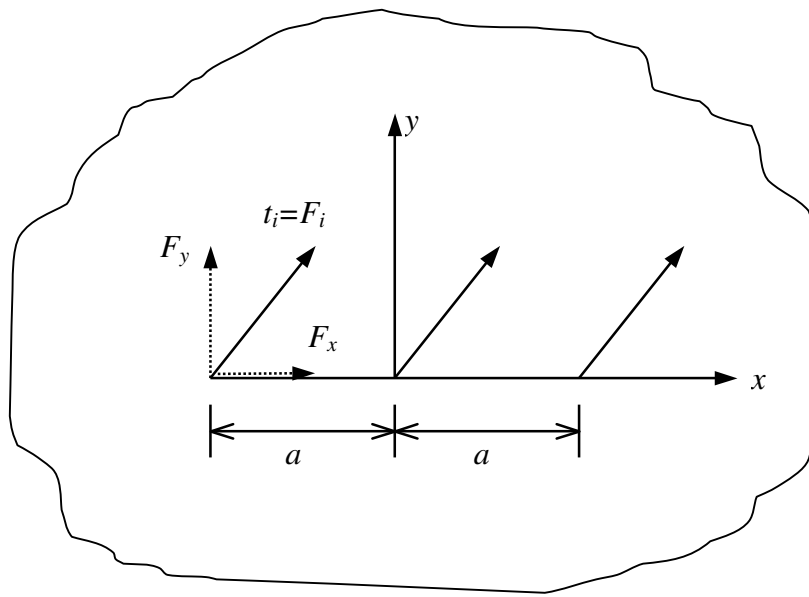


Figure 3. Spatial distribution of point forces on a straight-line segment in the fictitious stress method

### Fictitious Stress Method For Thermo-poroelasticity

The elastic fictitious stress method is based on the analytic solution to the problem of a point force in an infinite solid, which is also called Kelvin's problem (Crouch and Starfield, 1983). Suppose constant tractions  $t_x=F_x$  and  $t_y=F_y$  applied to the line segment  $|x| \leq a, y=0$  in an infinite elastic solid, as shown in Figure 3 (after Crouch and Starfield, 1983). The solution of spatial distribution of the point forces along the segment can be obtained by integrating the Kelvin's point force solution. Therefore, the displacement and the stress components can be computed everywhere. Fictitious stress method can be extended to thermo-poroelasticity using the following methodology.

At any given time  $t$ , temperature, pore pressure and stresses fields on the boundary can be approximated by the following methodology in the fictitious stress method (note that the heat equation is not coupled to others, thus it can be solved independently first):

- (1) Distribute point forces, fluid sources and heat sources on the boundary elements.
- (2) Temperature at each element is the sum of all temperatures caused by all heat sources taking place at time  $\tau \leq t$ . (The temperature field is decoupled from pore pressure and stresses because fluid sources and point forces do not contribute to temperature change.) The strengths of heat sources, which are functions of time, are calculated to satisfy the temperature boundary condition.

- (3) Pore pressure at each element is the sum of all pore pressures caused by all point forces, fluid sources and heat sources taking place at time  $\tau \leq t$ . Among them strengths of heat sources have been known from step (2).
- (4) Stresses at each element are the sum of all corresponding stresses induced by all point forces, fluid sources and heat sources taking place at time  $\tau \leq t$ . Among them strengths of heat sources have been known from step (2).
- (5) To satisfy the boundary conditions of pore pressure and stresses, strengths of point forces and fluid sources can be solved since contributions from heat sources have been known. The strengths of point forces and fluid sources are also functions of time.

### *Boundary Integral Equations*

With the fundamental solutions, one can get stresses, pore pressure and temperature at any point by conducting spatial integral along the boundary  $\Gamma$  and temporal integral along time  $t$  because of the time-dependent nature of the heat and fluid diffusion problems. The strengths of heat sources, fluid sources and point forces can be solved, as a function of time, from the known history of temperature, pore pressure and stress along the boundary. The determination of these unknowns requires the solution of a set of three singular integral equations. They are called integral equations because the unknowns appear inside the integral sign. These integral equations can be obtained by a heuristic approach, using the principle of superposition, or in a rigorous fashion based on the reciprocal theorem (Cheng and Detournay, 1998; Ghassemi and Zhang, 2004).

$$\sigma_{ij}(\mathbf{x}, t) = \int_0^t \int_{\Gamma} \left\{ \begin{aligned} &\sigma_{ijk}^{ip}(\mathbf{x}, \boldsymbol{\chi}; t - \tau) \psi_k(\boldsymbol{\chi}, \tau) \\ &+ \sigma_{ij}^{is}(\mathbf{x}, \boldsymbol{\chi}; t - \tau) \phi(\boldsymbol{\chi}, \tau) \\ &+ \sigma_{ij}^{ih}(\mathbf{x}, \boldsymbol{\chi}; t - \tau) \varphi(\boldsymbol{\chi}, \tau) \end{aligned} \right\} d\Gamma(\boldsymbol{\chi}) d\tau \quad (16)$$

$$p(\mathbf{x}, t) = \int_0^t \int_{\Gamma} \left\{ \begin{aligned} &p_k^{ip}(\mathbf{x}, \boldsymbol{\chi}; t - \tau) \psi_k(\boldsymbol{\chi}, \tau) \\ &+ p^{is}(\mathbf{x}, \boldsymbol{\chi}; t - \tau) \phi(\boldsymbol{\chi}, \tau) \\ &+ p^{ih}(\mathbf{x}, \boldsymbol{\chi}; t - \tau) \varphi(\boldsymbol{\chi}, \tau) \end{aligned} \right\} d\Gamma(\boldsymbol{\chi}) d\tau \quad (17)$$

$$T(\mathbf{x}, t) = \int_0^t \int_{\Gamma} \left\{ T^{ih}(\mathbf{x}, \boldsymbol{\chi}; t - \tau) \varphi(\boldsymbol{\chi}, \tau) \right\} d\Gamma(\boldsymbol{\chi}) d\tau \quad (18)$$

In the above equations,  $\Gamma$  is the boundary.  $\mathbf{x}$  and  $\boldsymbol{\chi}$  are two-dimensional co-ordinate tensors.  $\sigma_{ij}(\mathbf{x}, t)$  is the stress component at co-ordinates  $\mathbf{x}$  and at time  $t$ . The influence function  $\sigma_{ijk}^{ip}(\mathbf{x}, \boldsymbol{\chi}; t - \tau)$  represents stress component  $\sigma_{ij}(\mathbf{x}, t)$  due to an instantaneous unit point force, located at  $\boldsymbol{\chi}$  and taking place at time  $\tau$ . Similarly, symbols  $\sigma_{ij}^{is}(\mathbf{x}, \boldsymbol{\chi}; t - \tau)$  and  $\sigma_{ij}^{ih}(\mathbf{x}, \boldsymbol{\chi}; t - \tau)$  represents stress components induced by an instantaneous fluid source and an instantaneous heat source, respectively.  $p_i^{ip}$ ,  $p^{is}$  and  $p^{ih}$  are pore pressure induced by an instantaneous unit point force, fluid source and heat source.  $T^{ih}$  is temperature induced by a instantaneous unit heat source.  $\psi_k(\boldsymbol{\chi}, \tau)$ ,  $\phi(\boldsymbol{\chi}, \tau)$ , and  $\varphi(\boldsymbol{\chi}, \tau)$  are strengths of the point force, fluid source and heat source, respectively. Superscripts “ip”, “is” and “ih” denotes instantaneous force, fluid source

and heat source, respectively. Subscript  $i, j, k$  can take number 1 or 2, which denotes the two directions.

### *Fundamental Solutions*

In the boundary integral equations for thermo-poroelastic fictitious stress method described in equation (16), (17) and (18), terms  $\sigma_{ijk}^{ip}$ ,  $\sigma_{ij}^{is}$ ,  $\sigma_{ij}^{ih}$ ,  $p_i^{ip}$ ,  $p^{is}$ ,  $p^{ih}$  and  $T^{ih}$  are fundamental solutions corresponding to instantaneous singular impulses. Fundamental solutions for continuous impulses can be obtained by integrating the corresponding solutions for instantaneous impulses with respect to time. Stress tensor induced by a unit continuous point force is denoted as  $\sigma_{ijk}^{cp}$ , with superscript “cp” representing continuous point force. Similarly, symbols  $\sigma_{ij}^{cs}$ ,  $\sigma_{ij}^{ch}$ ,  $p_i^{cp}$ ,  $p^{cs}$ ,  $p^{ch}$  and  $T^{ch}$  are used to represent stresses, pore pressure and temperature due to certain kind of unit continuous impulse. Superscript “cs” and “ch” represent continuous fluid source and heat source, respectively.

Among them,  $\sigma_{ij}^{ch}$ ,  $p^{ch}$  and  $T^{ch}$  are stress, pore pressure and temperature induced by a continuous unit heat source, which represent the thermal effects in the non-isothermal poroelasticity, or thermo-poroelasticity. The derivation of fundamental solutions for continuous heat source in thermo-poroelasticity is given by Berchenko (1998) and listed in Appendix A. Spatial integrations of the fundamental solutions over a straight-line element were performed and are also included in Appendix A.



$\sigma_{ijk}^{cp}$ ,  $\sigma_{ij}^{cs}$ ,  $p_i^{cp}$ , and  $p^{cs}$  are poroelastic terms, which represents the coupling

between stresses and pore pressure. These four fundamental solutions are exactly the same with those used in the isothermal poroelastic fictitious stress method, and can be found in literature (e.g., Cheng and Detournay, 1988; Ghassemi et al., 2001). They are listed in Appendix B together with the expressions for their spatial integrations over a straight-line element. The fundamental solutions for a continuous heat source in thermoelasticity are also listed in Appendix C.

### *Numerical Implementation*

Numerical implementation of the boundary integral equations of transient thermo-poroelasticity requires spatial and temporal discretization. Spatial discretization is achieved by dividing the boundary of the problem into a number of elements and replacing the integrals over the boundary by a sum of integrals over these elements. Temporal discretization is realized by dividing the time domain into a number of time increments and utilizing a time marching scheme. In the present implementation, the following approximations are made:

- (1) the boundary elements are straight-line segments
- (2) the singular impulses (point force, displacement discontinuity, fluid source, heat source) are located at the midpoint of each element
- (3) the intensity of the impulses is constant over each element
- (4) the time increments,  $\Delta t$ , are constant

Suppose  $p+1$  is the number of time increments used, then the boundary integral equations for induced stresses, pore pressure and temperature expressed in equation (16), (17) and (18) can be rewritten as:

$$\sigma_{ij} = \sum_{\ell=0}^p \int_{\Gamma} \{ \sigma_{ijk}^{cp} \psi_k^{\ell} + \sigma_{ij}^{cs} \phi^{\ell} + \sigma_{ij}^{ch} \varphi^{\ell} \} d\Gamma \quad (39)$$

$$p = \sum_{\ell=0}^p \int_{\Gamma} \{ p_k^{cp} \psi_k^{\ell} + p_{ij}^{cs} \phi^{\ell} + p_{ij}^{ch} \varphi^{\ell} \} d\Gamma \quad (40)$$

$$T = \sum_{\ell=0}^p \int_{\Gamma} \{ T_{ij}^{ch} \varphi^{\ell} \} d\Gamma \quad (41)$$

where  $\psi_k^{\ell}$ ,  $\phi^{\ell}$  and  $\varphi^{\ell}$  are strengths of continuous point force, fluid source and heat source in time increment  $\ell$ .

Suppose  $N$  is the number of elements used to discretize the boundary. The spatial integrals over the boundary are replaced by a sum of integrals over these elements. Then, the induced stresses, pore pressure, and temperature on element  $m$  due to a constant spatial distribution of continuous force, fluid source and heat source on element  $r$  are given by:

$$\sigma_{ij}^m = \sigma_{ijk}^{cp} \psi_k^r + \sigma_{ij}^{cs} \phi^r + \sigma_{ij}^{ch} \varphi^r \quad (42)$$

$$p^m = p^{cp} \psi_k^r + p^{cs} \phi^r + p^{ch} \varphi^r \quad (43)$$

$$T_{ij}^m = T^{ch} \varphi^r \quad (44)$$

where  $\psi_k^r$ ,  $\phi^r$  and  $\varphi^r$  are strengths of continuous point force, fluid source and heat source on element  $r$ . The superscripts  $m$  and  $r$  refer to the influenced and influencing elements,

respectively. Influence coefficients  $\sigma_{ijk}^{cp}$ ,  $\sigma_{ij}^{cs}$ ,  $\sigma_{ij}^{ch}$ ,  $p_i^{cp}$ ,  $p^{cs}$ ,  $p^{ch}$  and  $T^{ch}$  now denote the influences of the element  $r$ , which are obtained by integrating the fundamental solutions for continuous point impulses over the influencing element  $r$ . The spatial integration over the straight-line constant elements is a relatively easy process in two-dimensional system. Integrations of the fundamental solution for a continuous heat source over an element of length  $2a$  are listed in Appendix A.

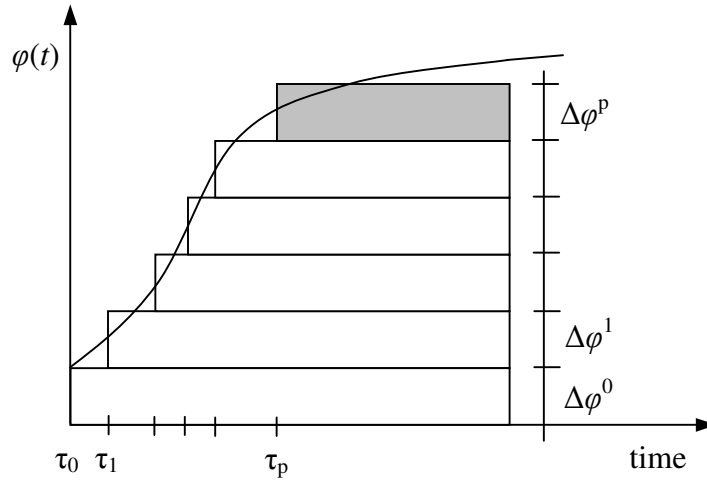


Figure 4. Time marching scheme for a continuous heat source

There are different approaches to temporal solution of the problem. One approach is solving the problem at the end of a time step and then using the results as the initial conditions for the next time step, marching forward in time. The disadvantage of this method is that it requires discretizing the spatial domain of the problem. The second approach is a time marching technique which solves the problem at the end of a time step

but keeps a solution history (Banerjee and Butterfield, 1981). This allows for strengths of singular impulses to vary with time. It involves incrementing the strengths of singular impulses at each time step and including the influence of all previous increments. This technique eliminates the need for internal discretization of the spatial domain. But it has the disadvantage that the coefficient matrix must be kept to be used as required. The scheme is illustrated with heat source  $\varphi(t)$  as an example in Figure 4 (after Curran and Carvalho, 1987).

The implementation of this time marching scheme is possible because it is the time interval between loading and receiving that affects the response rather than the absolute times. This is the so-called “time translation” property of the fundamental solutions. For example, the stress at a point  $\mathbf{x}$  and time  $t$  due to a heat source taking place at point  $\boldsymbol{\chi}$  and at time  $\tau$  is equal to the stress at point  $\mathbf{x}$  and time  $t-\tau$  due to a heat source occurring at time zero at the point  $\boldsymbol{\chi}$ . That is:

$$\sigma_{ij}^{ch}(\mathbf{x}, t; \boldsymbol{\chi}, \tau) = \sigma_{ij}^{ch}(\mathbf{x}, t - \tau; \boldsymbol{\chi}, 0) \quad (52)$$

Due to this property of the fundamental solutions, the evaluation time and loading time can be shifted along the time axis without affecting the values of the fundamental solutions. Therefore, the influence coefficient can be calculated only once during the calculation history.

From the above discussion, the induced stresses, pore pressure and temperature of element  $m$  are given by:

$$\begin{aligned}\sigma_{ij}^m(\mathbf{x}, t) = & \sum_{r=1}^N \left[ \sigma_{ijk}^{cp}(\mathbf{x}, \boldsymbol{\chi}, t - \tau_p) \Delta \psi_k^{rp} + \sigma_{ij}^{cs}(\mathbf{x}, \boldsymbol{\chi}, t - \tau_p) \Delta \phi^{rp} + \sigma_{ij}^{ch}(\mathbf{x}, \boldsymbol{\chi}, t - \tau_p) \Delta \varphi^{rp} \right] \\ & + \sum_{\ell=0}^{p-1} \sum_{r=1}^N \left[ \sigma_{ijk}^{cp}(\mathbf{x}, \boldsymbol{\chi}, t - \tau_\ell) \Delta \psi_k^{r\ell} + \sigma_{ij}^{cs}(\mathbf{x}, \boldsymbol{\chi}, t - \tau_\ell) \Delta \phi^{r\ell} + \sigma_{ij}^{ch}(\mathbf{x}, \boldsymbol{\chi}, t - \tau_\ell) \Delta \varphi^{r\ell} \right]\end{aligned}\quad (53)$$

$$\begin{aligned}p^m(\mathbf{x}, t) = & \sum_{r=1}^N \left[ p_k^{cp}(\mathbf{x}, \boldsymbol{\chi}, t - \tau_p) \Delta \psi_k^{rp} + p^{cs}(\mathbf{x}, \boldsymbol{\chi}, t - \tau_p) \Delta \phi^{rp} + p^{ch}(\mathbf{x}, \boldsymbol{\chi}, t - \tau_p) \Delta \varphi^{rp} \right] \\ & + \sum_{\ell=0}^{p-1} \sum_{r=1}^N \left[ p_k^{cp}(\mathbf{x}, \boldsymbol{\chi}, t - \tau_\ell) \Delta \psi_k^{r\ell} + p^{cs}(\mathbf{x}, \boldsymbol{\chi}, t - \tau_\ell) \Delta \phi^{r\ell} + p^{ch}(\mathbf{x}, \boldsymbol{\chi}, t - \tau_\ell) \Delta \varphi^{r\ell} \right]\end{aligned}\quad (54)$$

$$T^m(\mathbf{x}, t) = \sum_{r=1}^N \left[ T^{ch}(\mathbf{x}, \boldsymbol{\chi}, t - \tau_p) \Delta \varphi^{rp} \right] + \sum_{\ell=0}^{p-1} \sum_{r=1}^N \left[ T_{ij}^{ch}(\mathbf{x}, \boldsymbol{\chi}, t - \tau_\ell) \Delta \varphi^{r\ell} \right] \quad (55)$$

where  $p+1$  is the number of time increments.  $\Delta \psi_k^{rp}$ , and  $\Delta \phi^{r\ell}$ , et al. are the increments of strengths of certain kind of continuous impulse occurring on element  $r$ . It should be noted that co-ordinate of influencing point  $\boldsymbol{\chi}$  is also changing with each element along the boundary.

Equation (53), (54) and (55) constitute a set of linear algebraic equations which can be solved by applying the boundary conditions.

It should be noted that procedures described above are only used to solve boundary conditions specified by stresses, pore pressure and temperature. For boundary conditions described in displacement, fluid flux and heat flux, corresponding fundamental solutions are needed. However, the process of numerical implementation remains the same, which means the method used here can be easily adopted for other diffusion-deformation boundary element models provided the fundamental solutions are available.

## Displacement Discontinuity Method For Thermo-poroelasticity

As mentioned before, the fictitious stress method and displacement discontinuity method share similar principles in formulation. The major difference is in the analytical solutions which they are based on, and which control the formation of the influence coefficients.

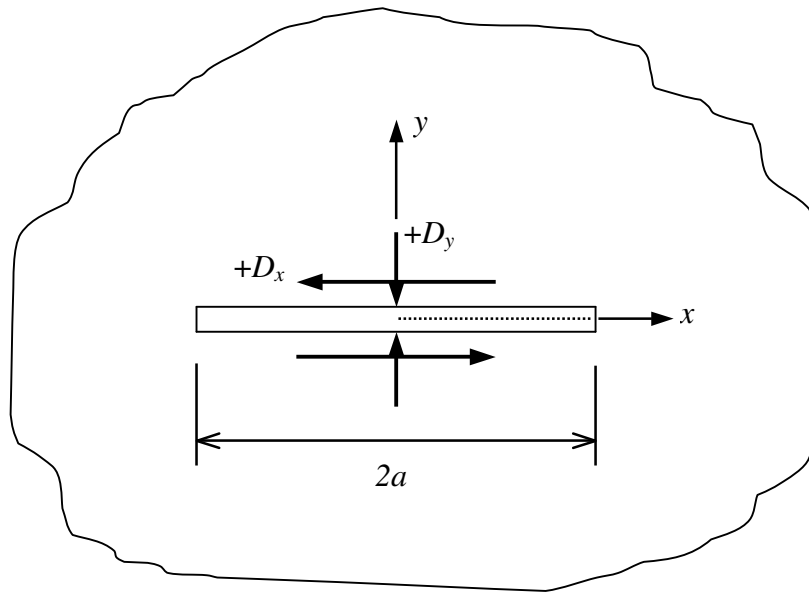


Figure 5. Constant normal and shear displacement discontinuity

The displacement discontinuity method is based on the fundamental solution for the problem of constant normal and shear discontinuities in displacement over a finite line segment in the  $x, y$  plane of an infinite elastic solid in plane strain, as shown in Figure 5 (after Crouch and Starfield, 1983). The line segment is chosen to occupy a

certain portion  $|x| \leq a, y = 0$ , Consider this segment to be a line crack with two surfaces, one is on the positive side of  $y=0$ , denoted  $y=0^+$ , and the other is on the negative side, denoted  $y=0^-$ . From one side of the line segment to the other, the displacements undergo a constant specified change in value  $D_i=(D_x, D_y)$ . Define the displacement discontinuity  $D_i$  as the difference in displacement between the two sides of the segment as follows:

$$D_x = u_x(x, 0^-) - u_x(x, 0^+) \quad (56)$$

$$D_y = u_y(x, 0^-) - u_y(x, 0^+) \quad (57)$$

The elastic solution to this problem is given by Crouch and Starfield (1983). The displacements and the stress components are then defined everywhere with function of  $D_x$  and  $D_y$ . The displacement discontinuity method can be extended to thermo-poroelasticity using a methodology similar to that used for the fictitious stress method by replacing the fictitious point force  $F_i$  with displacement discontinuity  $D_i$ .

### *Boundary Integral Equations*

Parallel to fictitious stress method, in displacement discontinuity method thermo-poroelastic problems can be modeled by distributing displacement discontinuity and fluid and heat sources on the boundary surface and requiring that the superposition of their effects satisfy the prescribed boundary conditions. The boundary integral equations for induced stresses, pore pressure and temperature can be written in the following forms:

$$\sigma_{ij}(\mathbf{x}, t) = \int_0^t \int_{\Gamma} \left\{ \begin{aligned} &\sigma_{ijk}^{id}(\mathbf{x}, \boldsymbol{\chi}; t - \tau) D_k(\boldsymbol{\chi}, \tau) \\ &+ \sigma_{ij}^{is}(\mathbf{x}, \boldsymbol{\chi}; t - \tau) \phi(\boldsymbol{\chi}, \tau) \\ &+ \sigma_{ij}^{ih}(\mathbf{x}, \boldsymbol{\chi}; t - \tau) \varphi(\boldsymbol{\chi}, \tau) \end{aligned} \right\} d\Gamma(\boldsymbol{\chi}) d\tau \quad (58)$$

$$p(\mathbf{x}, t) = \int_0^t \int_{\Gamma} \left\{ \begin{aligned} & p_k^{id}(\mathbf{x}, \boldsymbol{\chi}; t - \tau) D_k(\boldsymbol{\chi}, \tau) \\ & + p^{is}(\mathbf{x}, \boldsymbol{\chi}; t - \tau) \phi(\boldsymbol{\chi}, \tau) \\ & + p^{ih}(\mathbf{x}, \boldsymbol{\chi}; t - \tau) \varphi(\boldsymbol{\chi}, \tau) \end{aligned} \right\} d\Gamma(\boldsymbol{\chi}) d\tau \quad (59)$$

$$T(\mathbf{x}, t) = \int_0^t \int_{\Gamma} \left\{ T^{ih}(\mathbf{x}, \boldsymbol{\chi}; t - \tau) \varphi(\boldsymbol{\chi}, \tau) \right\} d\Gamma(\boldsymbol{\chi}) d\tau \quad (60)$$

where “*id*” denotes instantaneous displacement discontinuity.  $\sigma_{ijk}^{id}$  and  $p_k^{id}$  are the stress tensor and the pore pressure caused by an instantaneous displacement discontinuity, respectively.  $D_k$  is the strength (magnitude) of the displacement discontinuity in  $k$  direction. Other terms have the same meanings with those described in fictitious stress method in equation (16), (17) and (18). It can be seen that the temperature part remains the same in the two methods, because temperature is calculated separately while pore pressure and stress are fully coupled.

### *Fundamental Solutions*

The corresponding fundamental solutions for continuous impulses required in displacement discontinuity method are  $\sigma_{ijk}^{cd}$ ,  $\sigma_{ij}^{cs}$ ,  $\sigma_{ij}^{ch}$ ,  $p_i^{cd}$ ,  $p^{cs}$ ,  $p^{ch}$  and  $T^{ch}$ .

Among them, only  $\sigma_{ijk}^{cd}$  and  $p_i^{cd}$  are special for this method, the rest are the same with

those in fictitious stress method.  $\sigma_{ijk}^{cd}$ ,  $\sigma_{ij}^{cs}$ ,  $p_i^{cd}$ , and  $p^{cs}$  are poroelastic terms, and

have been given in Curran and Carvalho (1987). Thermally induced effects

$\sigma_{ij}^{ch}$ ,  $p^{ch}$  and  $T^{ch}$  are described in the previous section.



### Numerical Implementation

Due to the complete similarity in structure of displacement discontinuity method and fictitious stress method, details of numerical procedures for displacement discontinuity method can be easily obtained by modifying the foregoing discussion for fictitious stress method and therefore are omitted here.

In displacement discontinuity method, the induced stresses, pore pressure and temperature of element  $m$  are given by:

$$\begin{aligned} \sigma_{ij}^m(\mathbf{x}, t) = & \sum_{r=1}^N [\sigma_{ijk}^{cd}(\mathbf{x}, \boldsymbol{\chi}, t - \tau_p) \Delta D_k^{rp} + \sigma_{ij}^{cs}(\mathbf{x}, \boldsymbol{\chi}, t - \tau_p) \Delta \phi^{rp} + \sigma_{ij}^{ch}(\mathbf{x}, \boldsymbol{\chi}, t - \tau_p) \Delta \varphi^{rp}] \\ & + \sum_{\ell=0}^{p-1} \sum_{r=1}^N [\sigma_{ijk}^{cd}(\mathbf{x}, \boldsymbol{\chi}, t - \tau_\ell) \Delta D_k^{r\ell} + \sigma_{ij}^{cs}(\mathbf{x}, \boldsymbol{\chi}, t - \tau_\ell) \Delta \phi^{r\ell} + \sigma_{ij}^{ch}(\mathbf{x}, \boldsymbol{\chi}, t - \tau_\ell) \Delta \varphi^{r\ell}] \end{aligned} \quad (53)$$

$$\begin{aligned} p^m(\mathbf{x}, t) = & \sum_{r=1}^N [p_k^{cd}(\mathbf{x}, \boldsymbol{\chi}, t - \tau_p) \Delta D_k^{rp} + p^{cs}(\mathbf{x}, \boldsymbol{\chi}, t - \tau_p) \Delta \phi^{rp} + p^{ch}(\mathbf{x}, \boldsymbol{\chi}, t - \tau_p) \Delta \varphi^{rp}] \\ & + \sum_{\ell=0}^{p-1} \sum_{r=1}^N [p_k^{cd}(\mathbf{x}, \boldsymbol{\chi}, t - \tau_\ell) \Delta D_k^{r\ell} + p^{cs}(\mathbf{x}, \boldsymbol{\chi}, t - \tau_\ell) \Delta \phi^{r\ell} + p^{ch}(\mathbf{x}, \boldsymbol{\chi}, t - \tau_\ell) \Delta \varphi^{r\ell}] \end{aligned} \quad (54)$$

$$T^m(\mathbf{x}, t) = \sum_{r=1}^N [T^{ch}(\mathbf{x}, \boldsymbol{\chi}, t - \tau_p) \Delta \varphi^{rp}] + \sum_{\ell=0}^{p-1} \sum_{r=1}^N [T_{ij}^{ch}(\mathbf{x}, \boldsymbol{\chi}, t - \tau_\ell) \Delta \varphi^{r\ell}] \quad (55)$$

where  $p+1$  is the number of time increments,  $N$  is the number of elements.  $\Delta D_k^{rp}$ , and  $\Delta \phi^{r\ell}$ , et al. are the increments of strengths of certain kind of continuous impulse occurring on element  $r$ . Subscript  $k$  takes value from  $\{1, 2\}$ , which denotes the two directions.

The influence coefficient  $\sigma_{ijk}^{cd}$  and  $p_k^{cd}$  are obtained from spatial integration of fundamental solutions of a displacement discontinuity on the influencing element  $r$ . Other influence coefficients like  $\sigma_{ij}^{cs}$ , et al. have the same meaning with those in fictitious stress

method. It should be noted that equation (63) for induced temperature is exactly the same with equation (55).

Equation (61), (62) and (63) constitute a set of linear algebraic equations with the unknowns are the increments of the singular impulses. They can be solved by applying the boundary conditions.

#### Combined FS-DD Method For Thermo-poroelasticity

In order to model problems that involve both openings and cracks/fractures, the fictitious stress method and displacement discontinuity method are combined in one model in this thesis. It is relatively easy due to the similarity of the two methods. In thermo-poroelastic system, the difference between fictitious stress method and displacement discontinuity method lies in the poroelastic part only and the thermal effect can always be calculated separately.

The whole problem boundary is divided into two types: boundaries of opening and crack-type boundaries. The entire boundary is then discretized into  $N$  straight-line elements in the following way, as shown in Figure 6. The opening boundary is divided by  $M$  elements with a point force, a fluid source and a heat source applied on each element. These elements are used in fictitious stress method and thus are denoted as “FS” elements. Whereas the crack boundaries are divided by  $N-M$  elements with a displacement discontinuity, a fluid source and a heat source applied on each element. Similarly, these elements are called “DD” elements.

From principle of superposition, the induced stresses and pore pressure are the sum of the effects of all  $M$  fictitious point forces,  $N-M$  displacement discontinuities,  $N$

fluid sources and  $N$  heat sources. The induced temperature are the sum of the effects of all  $N$  heat sources.

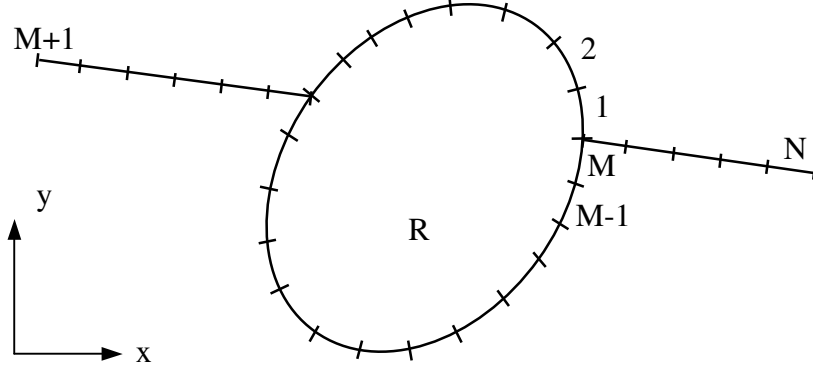


Figure 6. Discretization of combined FS-DD method

Therefore, using  $p+1$  as the number of time increments and the time marching scheme described before, the induced stresses, pore pressure and temperature of element  $m$  are given by:

$$\begin{aligned}
 \sigma_{ij}^m(\mathbf{x}, t) = & \sum_{r=1}^M \sigma_{ijk}^{cp}(\mathbf{x}, \boldsymbol{\chi}, t - \tau_p) \Delta \psi_k^{rp} + \sum_{r=M+1}^{N-M} \sigma_{ijk}^{cd}(\mathbf{x}, \boldsymbol{\chi}, t - \tau_p) \Delta D_k^{rp} \\
 & + \sum_{r=1}^N \left[ \sigma_{ij}^{cs}(\mathbf{x}, \boldsymbol{\chi}, t - \tau_p) \Delta \phi^{rp} + \sigma_{ij}^{ch}(\mathbf{x}, \boldsymbol{\chi}, t - \tau_p) \Delta \varphi^{rp} \right] \\
 & + \sum_{\ell=0}^{p-1} \left[ \sum_{r=1}^M \sigma_{ijk}^{cp}(\mathbf{x}, \boldsymbol{\chi}, t - \tau_\ell) \Delta \psi_k^{r\ell} + \sum_{r=M+1}^{N-M} \sigma_{ijk}^{cd}(\mathbf{x}, \boldsymbol{\chi}, t - \tau_\ell) \Delta D_k^{r\ell} \right] \\
 & + \sum_{\ell=0}^{p-1} \sum_{r=1}^N \left[ \sigma_{ij}^{cs}(\mathbf{x}, \boldsymbol{\chi}, t - \tau_\ell) \Delta \phi^{r\ell} + \sigma_{ij}^{ch}(\mathbf{x}, \boldsymbol{\chi}, t - \tau_\ell) \Delta \varphi^{r\ell} \right]
 \end{aligned} \tag{66}$$

$$\begin{aligned}
p^m(\mathbf{x}, t) = & \sum_{r=1}^M p_k^{cp}(\mathbf{x}, \boldsymbol{\chi}, t - \tau_p) \Delta \psi_k^{rp} + \sum_{r=M+1}^{N-M} p_k^{cd}(\mathbf{x}, \boldsymbol{\chi}, t - \tau_p) \Delta D_k^{rp} \\
& + \sum_{r=1}^N \left[ p^{cs}(\mathbf{x}, \boldsymbol{\chi}, t - \tau_p) \Delta \phi^{rp} + p^{ch}(\mathbf{x}, \boldsymbol{\chi}, t - \tau_p) \Delta \varphi^{rp} \right] \\
& + \sum_{\ell=0}^{p-1} \left[ \sum_{r=1}^M p_k^{cp}(\mathbf{x}, \boldsymbol{\chi}, t - \tau_\ell) \Delta \psi_k^{r\ell} + \sum_{r=M+1}^{N-M} p_k^{cd}(\mathbf{x}, \boldsymbol{\chi}, t - \tau_\ell) \Delta D_k^{r\ell} \right] \\
& + \sum_{\ell=0}^{p-1} \sum_{r=1}^N \left[ p^{cs}(\mathbf{x}, \boldsymbol{\chi}, t - \tau_\ell) \Delta \phi^{r\ell} + p^{ch}(\mathbf{x}, \boldsymbol{\chi}, t - \tau_\ell) \Delta \varphi^{r\ell} \right]
\end{aligned} \tag{67}$$

$$T^m(\mathbf{x}, t) = \sum_{r=1}^N \left[ T^{ch}(\mathbf{x}, \boldsymbol{\chi}, t - \tau_p) \Delta \varphi^{rp} \right] + \sum_{\ell=0}^{p-1} \sum_{r=1}^N \left[ T_{ij}^{ch}(\mathbf{x}, \boldsymbol{\chi}, t - \tau_\ell) \Delta \varphi^{r\ell} \right] \tag{68}$$

where  $\Delta \psi_k^{rp}$ ,  $\Delta D_k^{rp}$ ,  $\Delta \phi^{rp}$  and  $\Delta \varphi^{rp}$  are unknowns, meaning singular impulse increments in current time step  $p$ .  $\Delta \psi_k^{r\ell}$ ,  $\Delta D_k^{r\ell}$ ,  $\Delta \phi^{r\ell}$  and  $\Delta \varphi^{r\ell}$  are previous increments that have already been calculated. All influence coefficients are defined in the foregoing discussions.

Equation (66), (67) and (68) are  $N$  linear algebraic equations and can be solved using classic mathematical techniques. These three equations are the basis of combined FS-DD method for thermo-poroelasticity.

It should be noted that in order to avoid the singularity at the midpoints of the FS elements, the opening boundary is divided such that the intersection points with the crack boundary occur at the ends of FS elements, as shown in Figure 6.

A computer code was developed based on the above discussion. It provides a flexible tool for modeling of stress and pore pressure fields around underground openings and pre-existing cracks. It can handle thermo-poroelastic problems as well as isothermal

poroelastic problems. The isothermal poroelastic problems were simulated in this model by simply disabling the part producing the thermal effects.

## CHAPTER 4

### MODEL VERIFICATION AND TESTING

In order to verify the FS model, DD model and the combined FS-DD model developed in this thesis, an array of examples concerning poroelasticity and thermo-poroelasticity has been considered. The results are compared to closed forms or previously published results.

#### Problem Description

The pore pressure and stress distributions around a borehole are an important concern in drilling and hydraulic fracturing operations for production of petroleum and geothermal energy. Prior to drilling, a rock formation at depth exists in a state of initial stress, pore pressure and temperature. Drilling removes the rock and the stresses that were previously acting at the location. This action results in redistribution of stresses. Hydraulic and thermal gradients developed between the drilling mud and the formation cause additional modification of the stress state near the borehole. The additional stresses caused by these effects are referred to as “induced stresses”. The stress at any point is the sum of in-situ stresses and induced stresses.

Stress fields and pore pressure fields around a borehole are predicted using the FS model. Behaviors of cracks in fluid-saturated porous rock are examined by the DD

model. Openings and stress intensity factors of the cracks are calculated. For problems of a borehole with pre-existing cracks, the combined FS-DD model is used.

The rock is assumed to be Westerly Granite this chapter to simulate rocks encountered in Coso geothermal field. Input parameters for Westerly Granite are listed in Table 1 (Data are taken from McTigue, 1986).

Table 1. Input parameters for Westerly Granite

Variable	Physical meaning	Value	Unit
$E$	Modulus of elasticity	$3.75 \times 10^4$	MPa
$\nu$	Poisson's ratio	0.25	-
$\nu_u$	Undrained Poisson's ratio	0.33	-
$K_s$	Solid bulk modulus	$4.5 \times 10^4$	MPa
$K_f$	Fluid bulk modulus	$2.5 \times 10^3$	MPa
$c^T$	Thermal diffusivity	$5.1 \times 10^{-6}$	M <sup>2</sup> /sec
$C$	Heat capacity	790.0	Joule/(kg·°C)
$\beta_s$	Solid thermal expansion coef.	$2.4 \times 10^{-5}$	1/°C
$\beta_f$	Fluid thermal expansion coef.	$3.00 \times 10^{-4}$	1/°C
$n$	Porosity	0.01	-
$\gamma_f$	Unit weight of fluid	$9.8 \times 10^3$	N/m <sup>3</sup>
$k$	Intrinsic permeability	$4.053 \times 10^{-7}$	Darcy
$B$	Skempton's constant	0.815	-
$\mu$	Fluid viscosity	$3.547 \times 10^{-4}$	kg/(m·sec)

## Borehole Under Non-hydrostatic Stress Loading

This example is considered to verify the poroelastic FS model. Consider drilling a vertical circular borehole with radius  $R$  in a fluid saturated Westerly Granite rock subjected to a uniform in-situ anisotropic stress and a pore pressure. This is an isothermal poroelastic problem, and can be analyzed in two dimensions by assuming plane strain conditions.

The loadings can be described as (see Figure 7):

$$\sigma_{xx} = -(P_0 - S_0) \quad (40)$$

$$\sigma_{yy} = -(P_0 + S_0) \quad (41)$$

$$\sigma_{xy} = 0 \quad (42)$$

$$p = P_0 \quad (43)$$

where  $P_0$  is the hydrostatic stress (mean stress),  $S_0$  is the deviatoric stress, and  $p_0$  is the virgin pore pressure.

The loading condition can be decomposed into three fundamental modes. Among them, Mode 1 and 2 are axisymmetric loadings; Mode 3 is asymmetric loading (Detournay and Cheng, 1988):

Mode 1: hydrostatic stress loading

$$\begin{aligned} \sigma_{xx} &= \sigma_{yy} = -P_0 \\ p &= 0 \end{aligned} \quad (44)$$

Mode 2: pore pressure loading

$$\begin{aligned} \sigma_{xx} &= \sigma_{yy} = 0 \\ p &= p_0 \end{aligned} \quad (45)$$



Mode 3: deviatoric stress loading

$$\begin{aligned}\sigma_{xx} &= S_0, \sigma_{yy} = -S_0 \\ p &= 0\end{aligned}\tag{46}$$

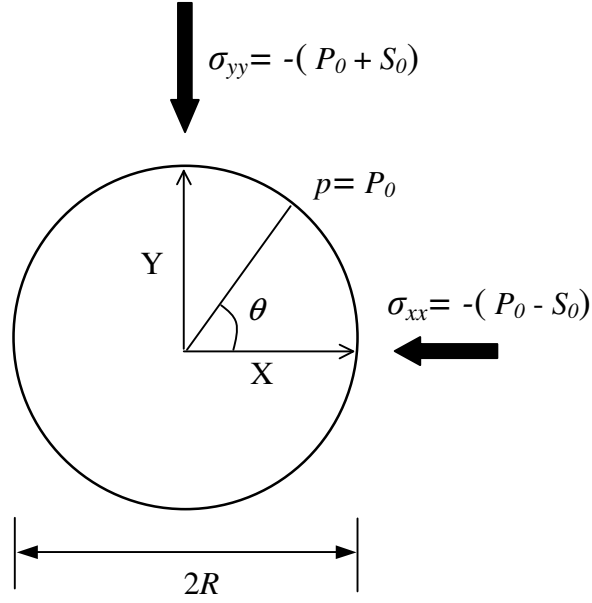


Figure 7. Circular borehole under non-hydrostatic stress loading

For each of the above loading mode, induced stress field and pore pressure field are examined and analyzed using the FS model. This problem is solved by dividing the boundary into 25 elements for a quarter of the borehole wall. Symmetry with respect to both  $x$ -axis and  $y$ -axis are considered. Time is normalized by  $t^* = tc^f / R^2$ . The number of time steps is 10 for each computation and the time step length,  $\Delta t$ , is adjusted accordingly. To compare with Detournay and Cheng's work (1988), *tension positive* convention is used in plots of this section.

### Mode 1: Hydrostatic Stress Loading

The mode 1 loading case is hydrostatic stress loading. The far field stress field is considered to be -10 MPa everywhere. That is, magnitude of hydrostatic stress  $P_0 = 10$  MPa. There is no pore pressure in the far field and the initial temperature is zero. Stresses on boundary are considered to be reduced to zero. The pressure and temperature on boundary are maintained at the initial values.

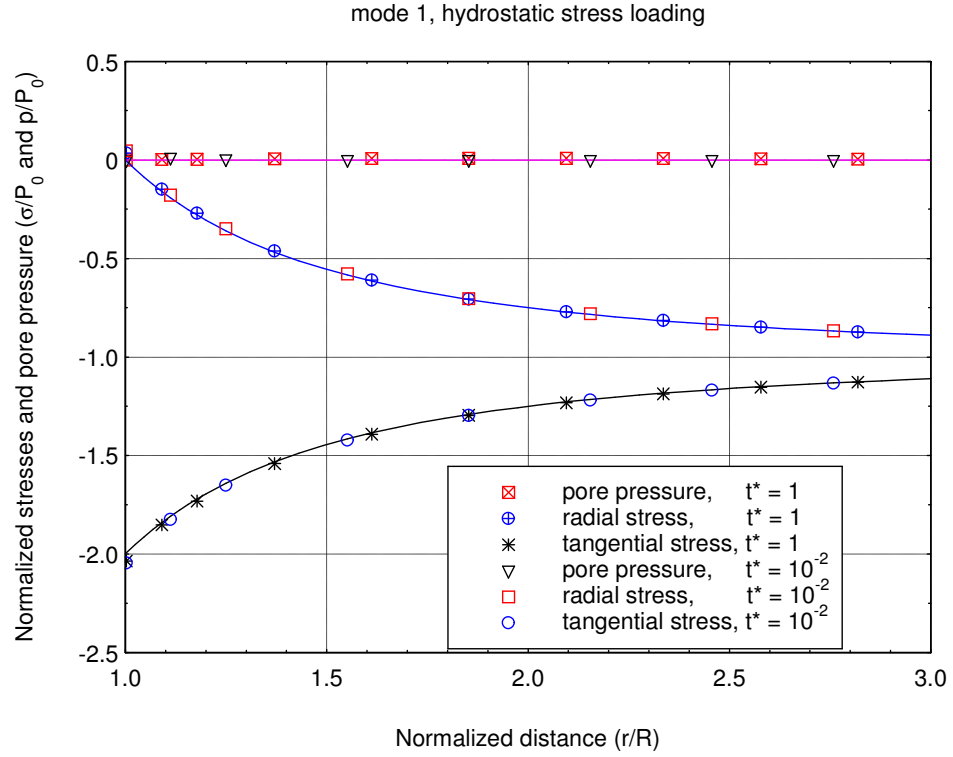


Figure 8. Stresses and pore pressure field under hydraulic stress loading

Tangential stress, radial stress and pore pressure near the borehole at normalized time  $t^* = 0.01$  and  $t^* = 1$  are plotted in Figure 8. The field points plotted in the figure are located along the line  $\theta = 0$ , and their distance from the borehole wall is normalized by  $r/R$ .

One can see excellent agreement between the FS results and the analytical solutions, which are represented using curves in the plot. Under this loading mode, no pore pressure change is induced as the stress field is identical to the classical elastic solution and leads to no volumetric strain:

$$\frac{\sigma_{\theta\theta}}{P_0} = -1 - \frac{R^2}{r^2} \quad (47)$$

$$\frac{\sigma_{rr}}{P_0} = -1 + \frac{R^2}{r^2} \quad (48)$$

### *Mode 2: Pore Pressure Loading*

In the case of mode 2 loading, the pore pressure at the boundary is reduced from initial value. Far field stress field is considered to be zero everywhere. Virgin pore pressure is  $p_0 = 4\text{MPa}$ . Far field temperature is zero. Stresses and pressure on boundary are considered to be zero. The temperature on boundary is also zero.

Figure 9 shows the pore pressure history at various distances from the borehole predicted by FS model and closed forms. They agree very well in the plot.

Figure 10 and 11 are the plots for tangential stress field and radial stress field, respectively. Stresses are normalized by  $\sigma/\eta p_0$ , where  $\eta$  is a poro-elastic coefficient given by:

$$\eta = \frac{3(\nu_u - \nu)}{2B(1 - \nu)(1 + \nu_u)} = \alpha \frac{1 - 2\nu}{2(1 - \nu)}$$

Both plots indicates perfect match between FS results and closed solutions. The work also agrees with those of Detournay and Cheng (1988).

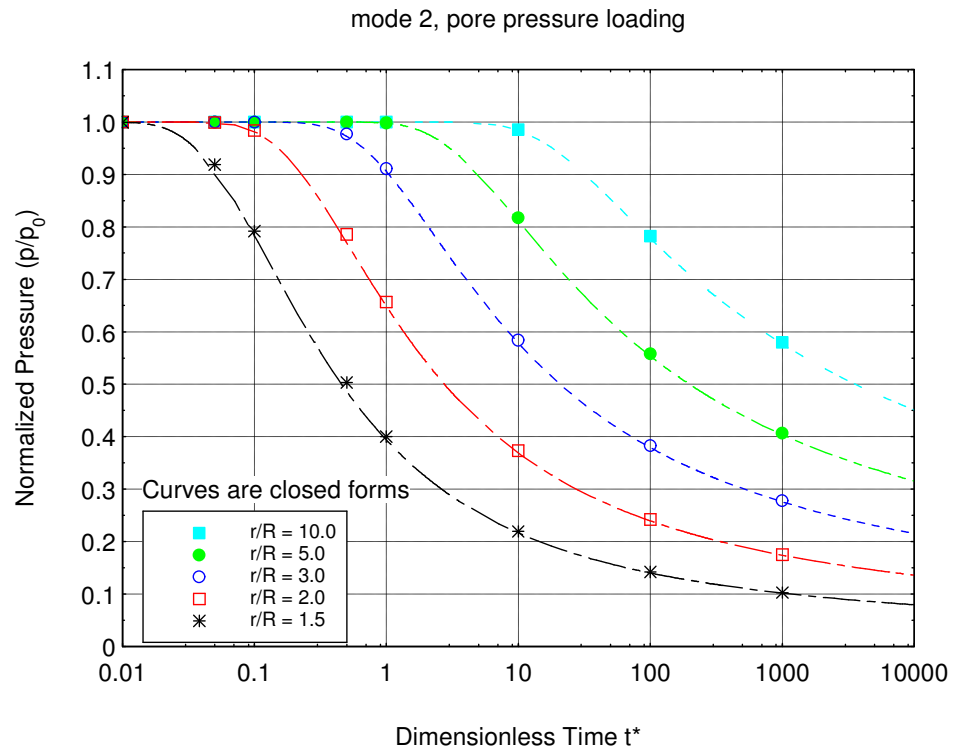


Figure 9. Pore pressure history at different points under pore pressure loading

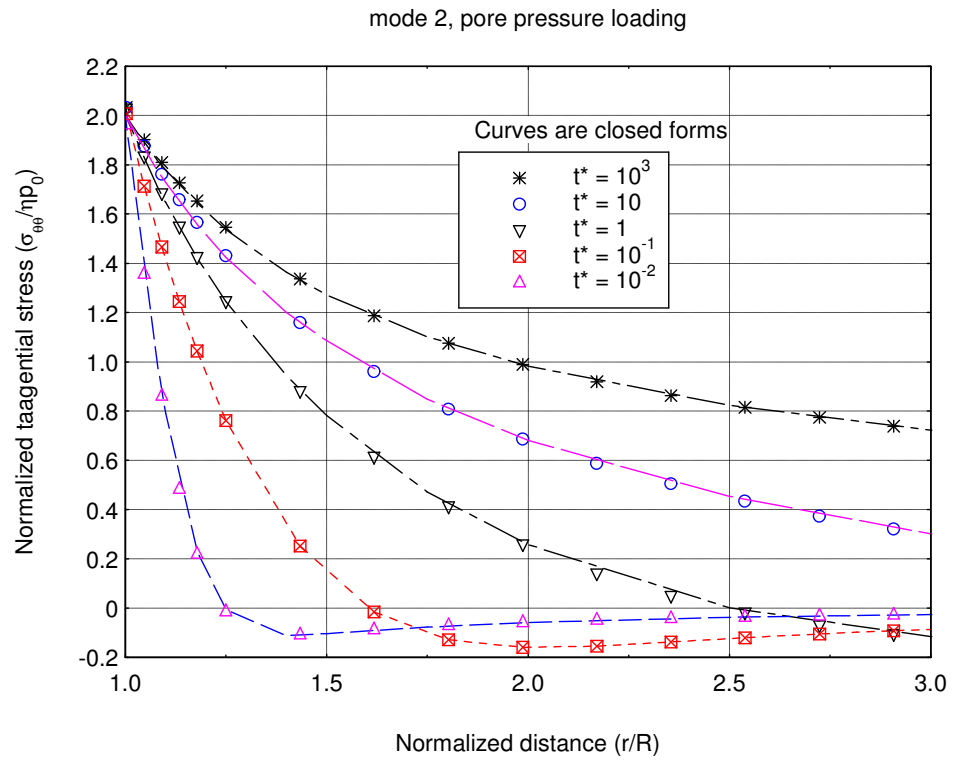


Figure 10. Tangential stress field due to pore pressure loading at various times

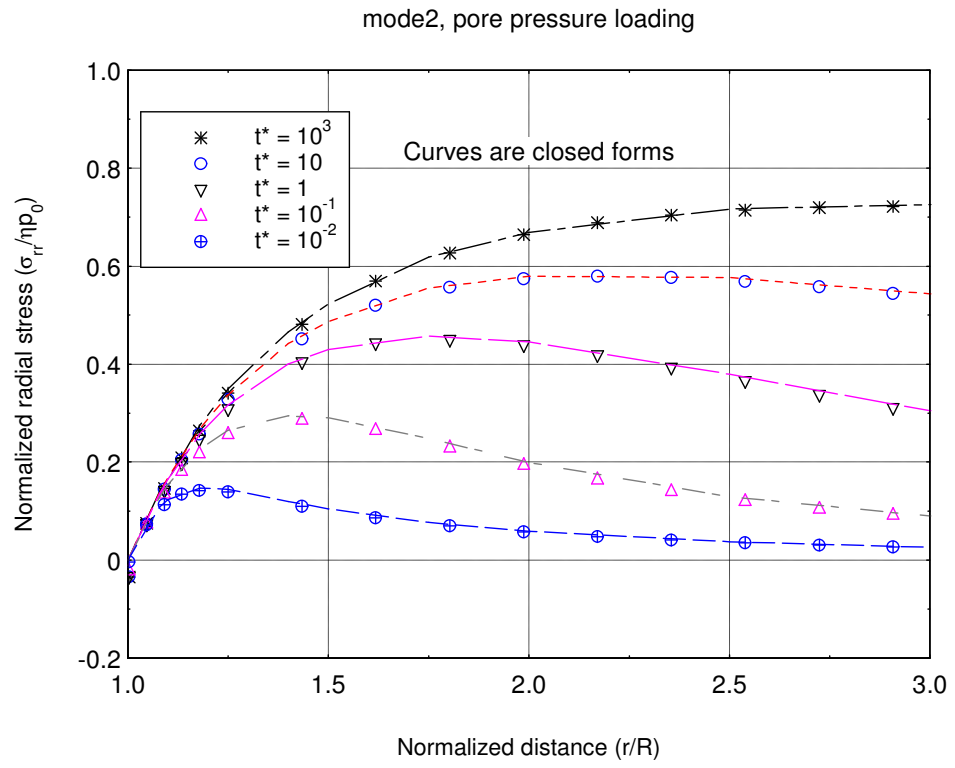


Figure 11. Radial stress field due to pore pressure loading at various times

### Mode 3: Deviatoric Stress Loading

Mode 3 loading is deviatoric stress loading without pore pressure and temperature loading. Assume in-situ stresses are  $\sigma_{xx} = 2$  MPa and  $\sigma_{yy} = -2$  MPa, that is, magnitude of stress deviator  $S_0 = 2$  MPa.

Under pure deviatoric stress loading, the induced pore pressure, tangential stress and radial stress fields for  $\theta = 0$  are plotted in Figure 12, 13 and 14 respectively. In Figure 12, the dash line represents the closed form instantaneous (for  $t^* < 10^{-2}$ ) pore pressure distribution given by (Detournay and Cheng, 1988):

$$p^{0+} = \frac{4}{3} S_0 B (1 + \nu_u) \frac{R^2}{r^2} \cos 2\theta \quad (49)$$

in which  $r$  is the distance from center of the borehole. It should be noted that only the field points at  $\theta = 0$  are examined in this section.

One can see there exist a steep radial gradient of the pore pressure at early times, which is triggered by the rapid drainage of fluid at the wall. The pore pressure peak decays with time, and moves away from the borehole wall.

Figure 13 shows the tangential stress field in various times. The dash line is closed form solution at the instance of drilling given by (Detournay and Cheng, 1988):

$$\sigma_{\theta\theta}^{0+} = - \left( 1 + 3 \frac{R^4}{r^4} \right) S_0 \cos 2\theta \quad (50)$$

However, the tangential stress at the borehole wall, is instantaneously reduced to  $-4 \frac{1-\nu_u}{1-\nu} S_0 \cos 2\theta$ . As a result, at very small time (here shows at  $t^* = 10^{-4}$ ), the peak of the tangential stress occurs inside the rock instead of the borehole wall, as predicted by

the elastic analysis. This phenomenon is caused by the stiffness contrast at the borehole wall and the rock further away due to rapid drainage (Detournay and Cheng, 1988). As time increases, the tangential stress decreases monotonically with distance. At  $t^* = 1$  the tangential stress at the wall is pretty close to the long-term elastic value  $-4S_0 \cos 2\theta$ .

From Figure 14, it is clear that unlike the tangential stress, the radial stress experiences little variation with time. Figure 12, 13 and 14 agree very well with Detournay and Cheng's work in 1988.

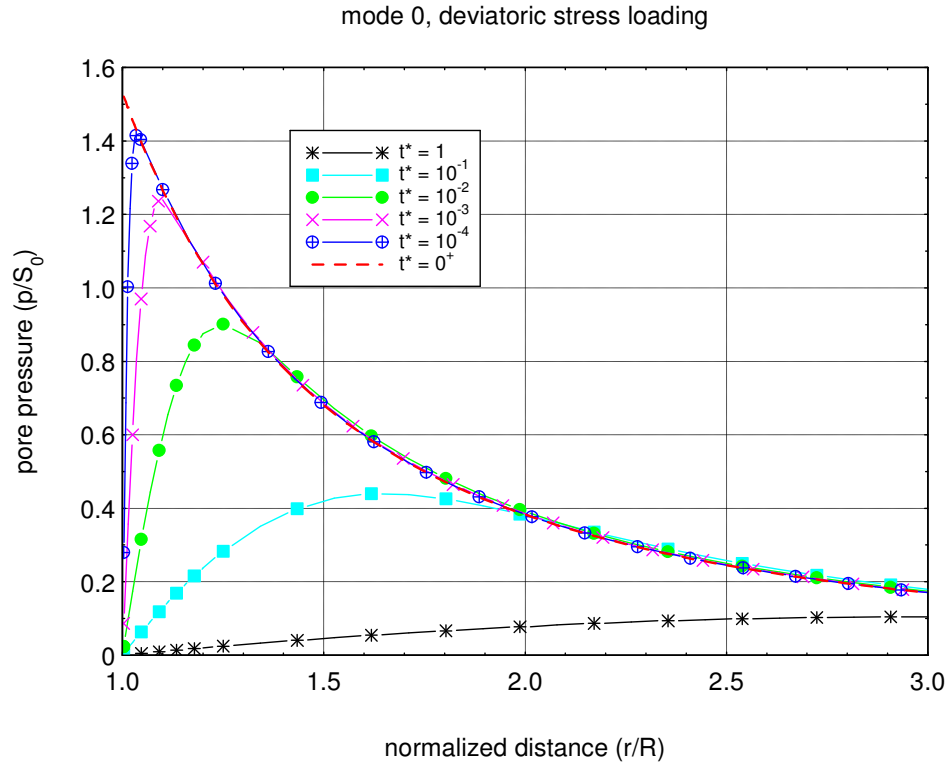


Figure 12. Pore pressure field due to deviatoric stress loading at various times



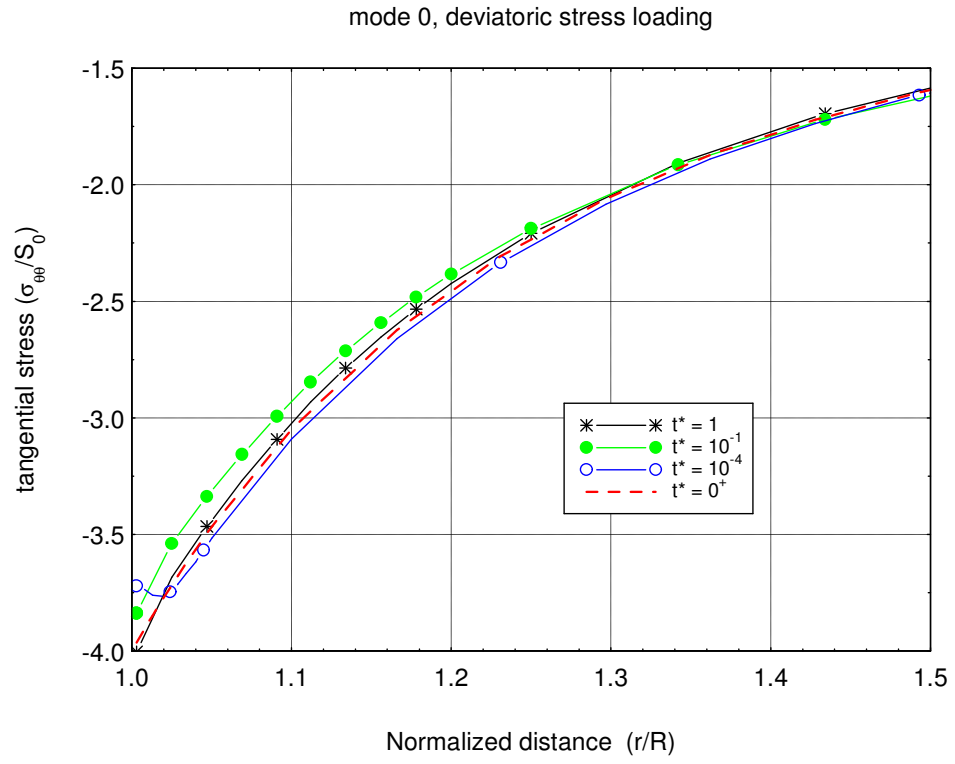


Figure 13. Tangential stress field due to deviatoric stress loading at various times

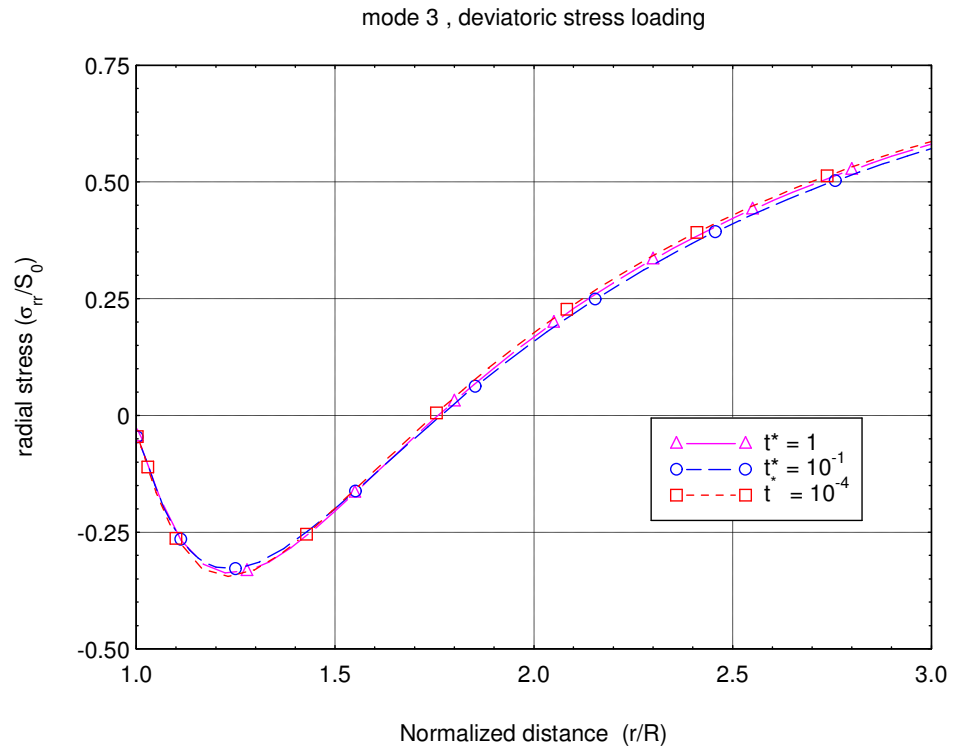


Figure 14. Radial stress field under deviatoric stress loading at various times

### Borehole Under Thermal Loading

Consider a borehole with radius  $R = 0.1\text{m}$  as shown in Figure 15 in a reservoir with a temperature  $T_0$  of  $200^\circ\text{C}$ . The borehole wall is suddenly cooled by water and maintained  $T_w$  at  $80^\circ\text{C}$ . For clarity of presentation and investigation of the role of temperature, only induced stress and pore pressure are studied. Thus, no pore pressure and no stress loadings are considered meaning that the far field pore pressure and stresses are considered to be zero. Due to symmetry only a quarter of the borehole boundary is modeled and 25 elements are used to approximate one-quarter of the circular boundary. Number of time steps is 10 for each computation and the time step length,  $\Delta t$ , is adjusted accordingly.

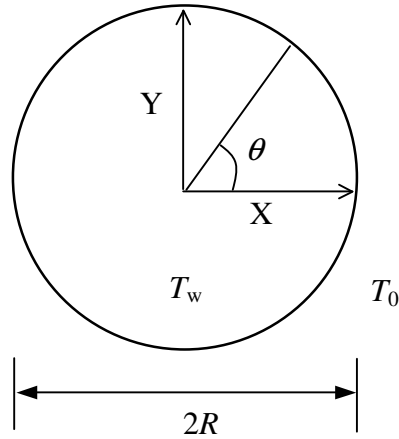


Figure 15. Circular borehole under thermal loading

Figures 16-19 illustrate the profiles of temperature, induced pore pressure, induced tangential stress, and radial stress around the borehole. Analytical results are also shown for comparison. As can be observed, the numerical results agree well with the analytic solution, which verifies the numerical procedure used in the FS model for thermo-poroelastic problems.

Figure 16 shows the transient temperature distribution; it is typical of a conductive heat transfer situation. Rock formation is gradually cooled off as the borehole temperature is kept constant.

Figure 17 is the distribution of the induced pore pressure. One can see that a pressure drop is generated near the borehole at early time. With time, the pore pressure will gradually recover toward its original state.

Figure 18 presents the thermally induced tangential stress. With cooling, a significant tangential tensile stress is induced around the borehole. This is caused by the tendency of the rock to shrinkage near the borehole wall. Away from the borehole wall, the magnitude of the induced tensile stress decreases and at some point inside the formation it changes sign, turning into a compressive stress. This is because the shrinkage of the material at the inner face of the borehole geometry, due to cooling, tends to pull on the outer rock thus inducing a compressive stress on the outer rock. The compressive zone fades away with distance and gradually moves away from the borehole.

Figure 19 illustrates the thermally induced radial stress. A significant radial tensile stress peak is produced inside the formation. At later times, the tensile stress zone moves inside the formation while the magnitude of the “peak” increases.

From the above observations, one can see cooling increases the potential of fracturing because of the tangential tensile stress induced by the material shrinkage. The fracture will always be initiated from the borehole wall because the maximum tensile stress always occurs there. However, a tensile stress zone will develop around the borehole with time, which can encourage the time-delayed fracture development.

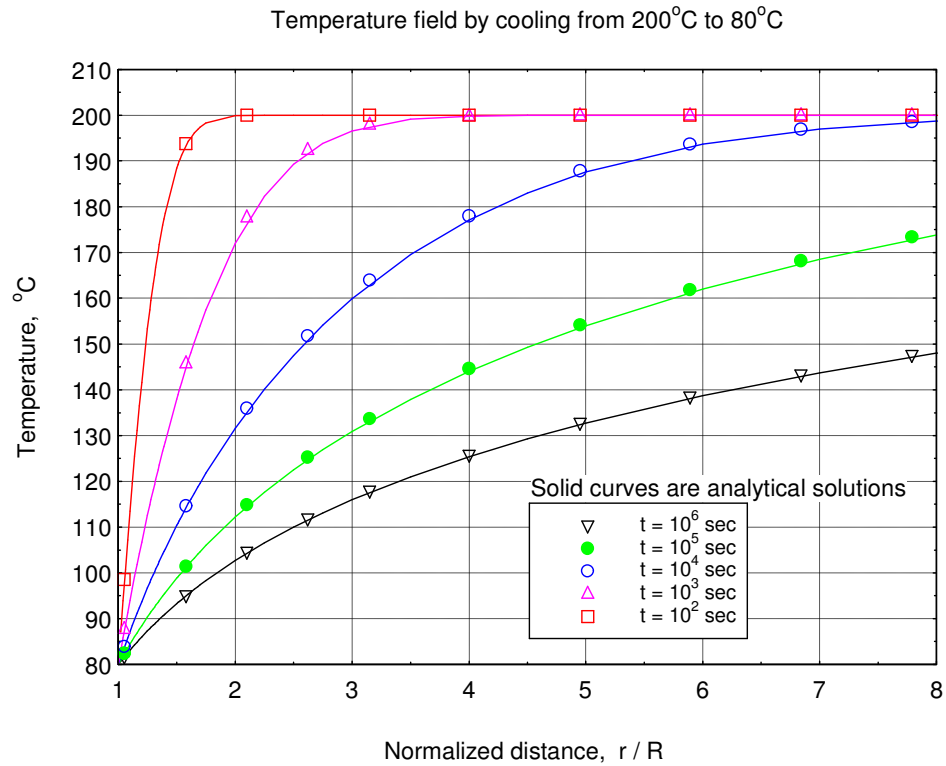


Figure 16. Temperature field under thermal loading at various times

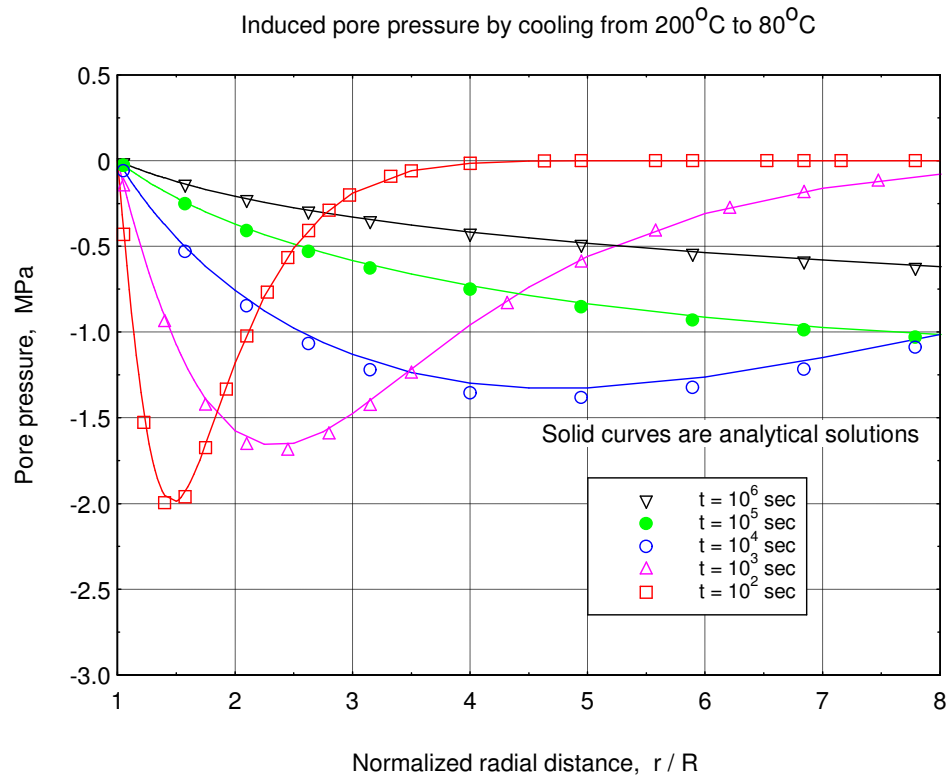


Figure 17. Pore pressure field under thermal loading at various times

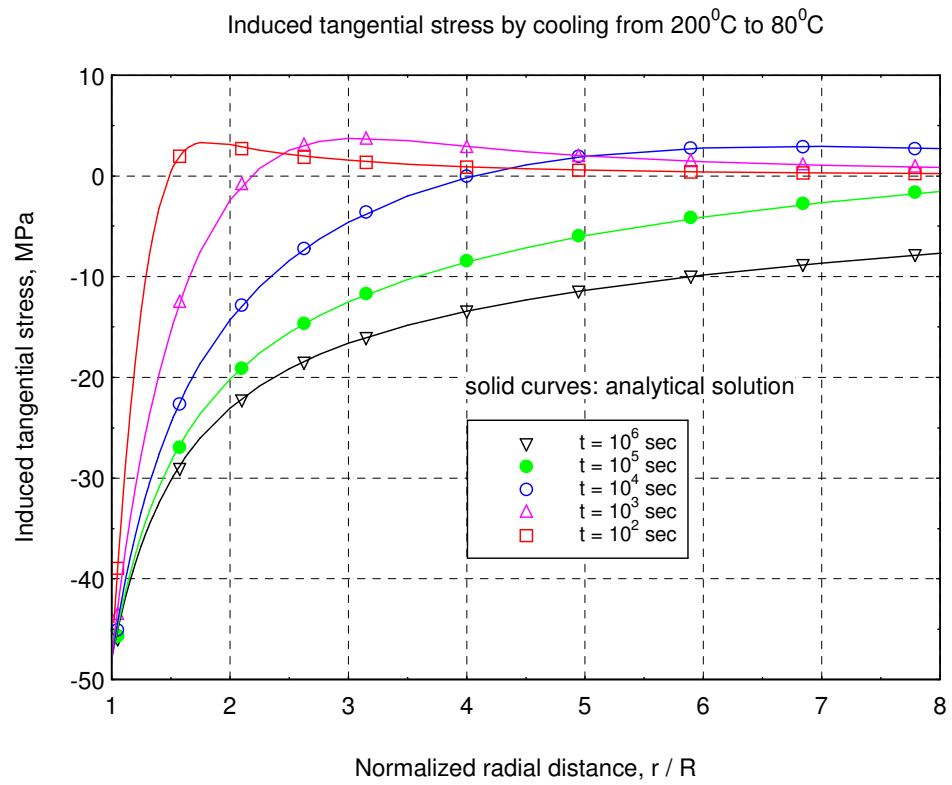


Figure 18. Tangential stress field under thermal loading at various times

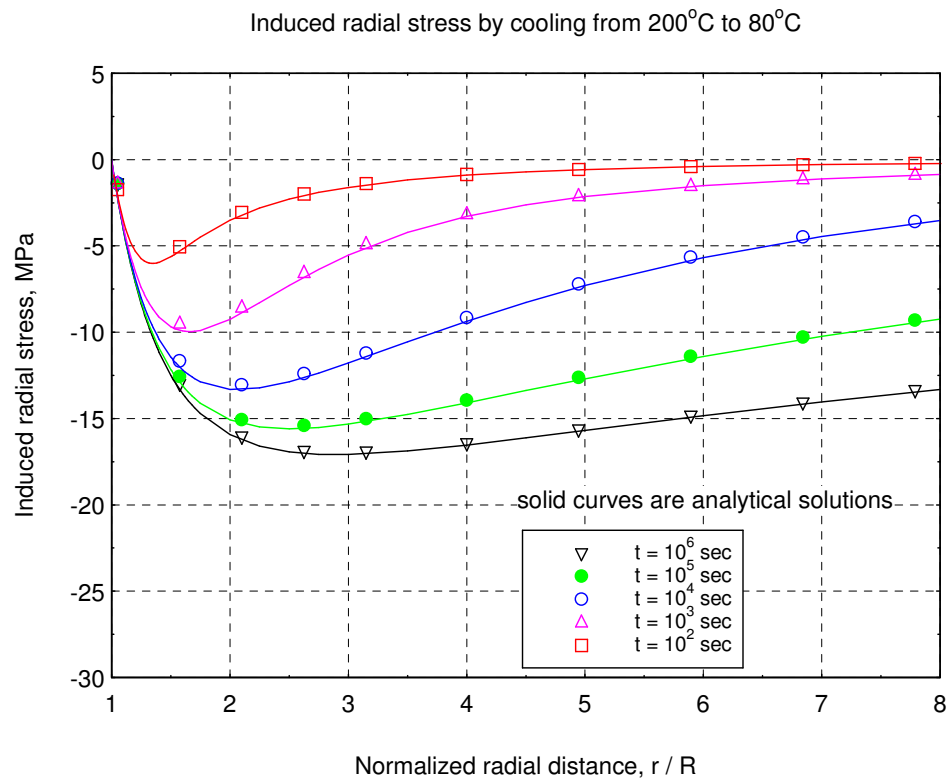


Figure 19. Radial stress field under thermal loading at various times



### Uniformly Pressurized Crack Problem

This example is used to verify the poroelastic DD model. The problem studied here is the response of a suddenly pressurized crack of length  $2L$  (shown in Figure 20). This pressurization by a fluid pressure  $P$  may be decomposed into two fundamental modes of loading (Detournay and Cheng, 1991), namely a normal stress loading and a pore pressure loading as shown below:

Mode 1: stress loading

$$\sigma_n(x, t) = -PH(t) \quad (51)$$

$$p(x, t) = 0 \quad (52)$$

Mode 2: pressure loading

$$p(x, t) = PH(t) \quad (53)$$

$$\sigma_n(x, t) = 0 \quad (54)$$

where  $H(t)$  denotes Heaviside step function. The initial conditions for both problems are zero stress and pore pressure everywhere.

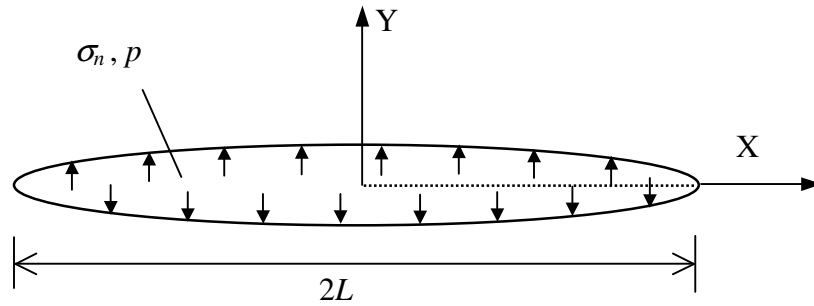


Figure 20. Uniformly pressurized crack

In this section, normal stress applied on the crack surface is assumed to be  $-15$  MPa, and pore pressure inside the crack is  $15$  MPa. The crack extends from  $(-1.0, 0.0)$  to  $(1.0, 0.0)$ , with its center at  $(0.0, 0.0)$  so that its length is  $2.0$  m. Temperature is considered to be  $0^\circ\text{C}$  everywhere.

### *Mode 1: Stress Loading*

#### Initial And Final Crack Opening

Mode 1 loading is responsible for a time-dependent opening of the crack. At time  $t=0^+$ , the crack opens according to the well known Sneddon's solution (Detourney and Cheng, 1991) with undrained Poisson ratio  $\nu_u$ :

$$D_n(x) = -\frac{2PL(1-\nu_u)}{G} \left(1 - \frac{x^2}{L^2}\right) \quad (55)$$

At  $t = 1$  sec, (normalized time  $\tau = t \cdot c^f / L^2 = 6.48 \times 10^{-3}$ ), the crack profile is computed by the DD model and is plotted in Figure 21, with the analytical short-term solution predicted from equation (55).

As time increases, the crack opens and reaches the steady-state solution given by the previous equation but with drained material properties. That is, at time  $t = \infty$ , the crack opens according to (Detourney and Cheng, 1991):

$$D_n(x) = -\frac{2PL(1-\nu)}{G} \left(1 - \frac{x^2}{L^2}\right) \quad (56)$$

The crack opening calculated by the DD model at  $t = 10^7$  sec is plotted in Figure 22 along with the analytic long-term solution.

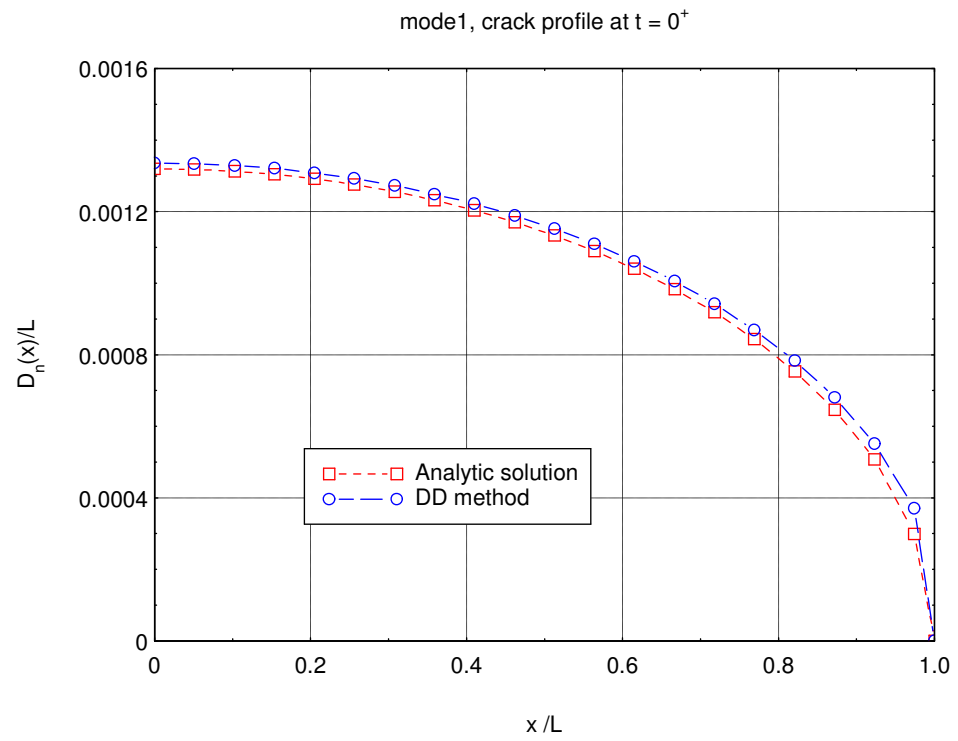


Figure 21. Short-term crack opening under uniformly stress loading

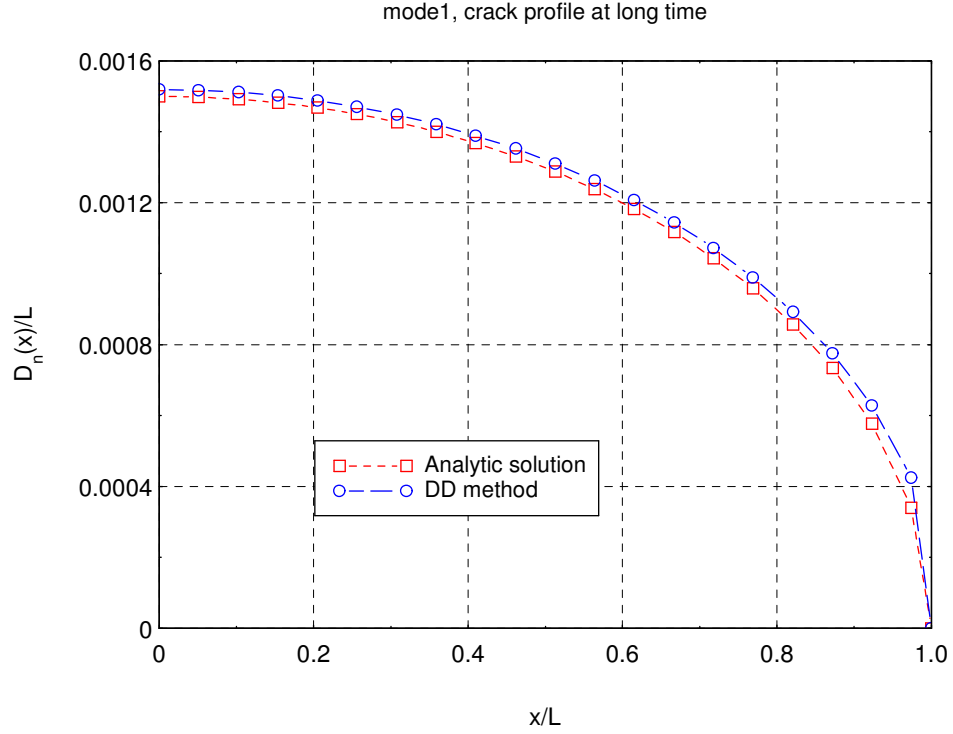


Figure 22. Long-term crack opening under uniformly stress loading

Figure 21 and Figure 22 show that overall, the results of the DD model agree well with the analytic solution. The DD model slightly overestimates the crack opening by less than 4% for most elements far from the tip. The results are the least accurate near the tip. At the tip element, the error goes up for both short-term and long-term calculations. Crouch and Starfield (1983) obtained a comparable error when modeling a pressurized crack with constant-strength DD elements over its whole length (Crouch and Starfield, 1983). The discrepancy can be attributed to the use of constant DD elements, that is, constant displacement and fluid flux approximation on each element. The results will be more accurate if the element number is increased. To obtain good results near the crack tips, a special higher-order tip DD element should be used to replace the current constant

DD element in the future study. The tip element approach gives reasonably good results according to Crouch and Starfield(1983).

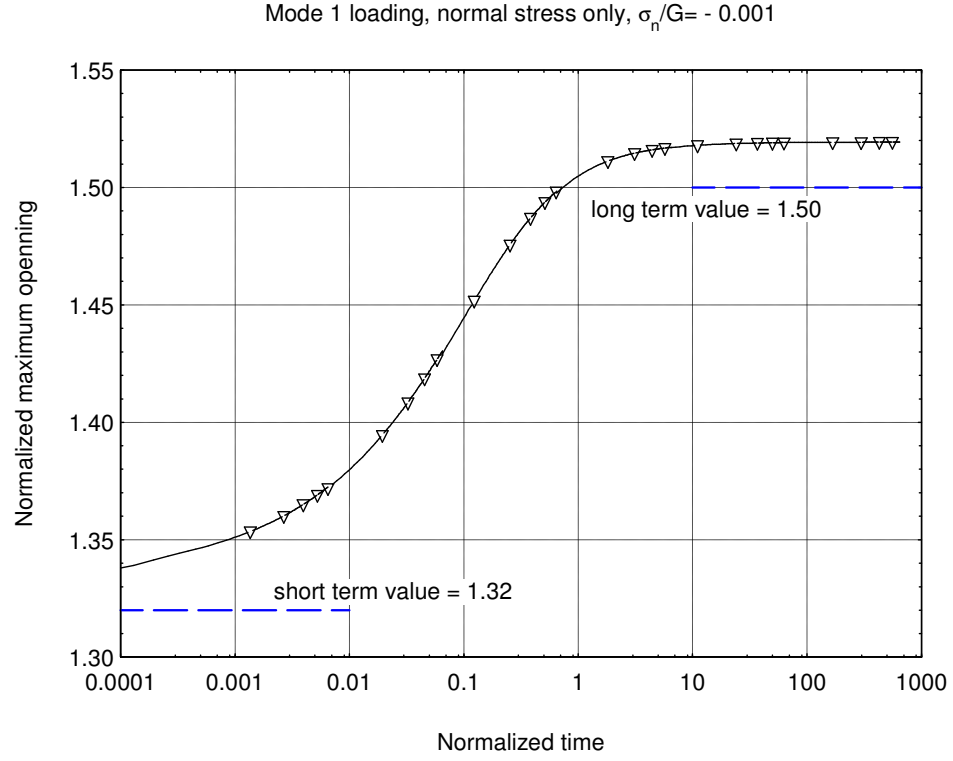


Figure 23. Normalized maximum crack opening under stress loading

### Maximum Crack Opening

At any time, the maximum opening along the crack occurs at the center. The maximum normalized opening is defined as:

$$(\hat{D}_n)_{\max} = \frac{D_n(0,t)G}{|\sigma_n|L} \quad (57)$$

It should evolve with time from an initial value of  $2(1 - \nu_u) = 1.32$  to a final value of  $2(1 - \nu) = 1.50$  (Vandamme et al. 1989).

In Figure 23,  $(\hat{D}_n)_{\max}$  is plotted as a function of the normalized time  $\tau = tc^f / L^2$ . One can see that the normalized maximum opening predicted by the DD model agrees with the closed forms. It tends to slightly overpredict the maximum crack opening in both initial and final conditions. Similar results have been obtained by other researchers. (e.g. Vandamme et al. 1989).

### Stress Intensity Factor

The Stress Intensity Factors (SIFs) are used to define the magnitude of the singular stress and displacement fields (local stresses and displacements near the crack tip). Although the concept originated from studies of elastic materials, it can be used to poroelastic materials. The  $1/\sqrt{r}$  singularity characteristic is inherent in the nature of the elastic stresses around a crack tip from which  $r$  is measured (Sih et.al., 1962). *That is to say, the form of stress singularity around the tip does not change in the presence of temperature and pore pressure field. Therefore, one can use the typical calculation method for the elastic SIFs in thermo-poroelastic problems.*

The classical elastic relationship between the crack opening displacement and the SIF is given by (Detournay and Cheng, 1991):

$$K_I = \frac{\sqrt{\pi}G}{\sqrt{8(1-\nu)}} \lim_{|x| \rightarrow L} \frac{D_n(x)}{\sqrt{L-|x|}}, \quad -L < x < L \quad (58)$$

where  $G$  is shear modulus,  $D_n$  is crack opening at a point  $S(x, 0)$  near the crack tip as shown in Figure 24. And  $(L - |x|)$  is the distance from this point to the tip.  $K_I$  has unit  $(\text{MPa} \cdot \text{m}^{1/2})$ .

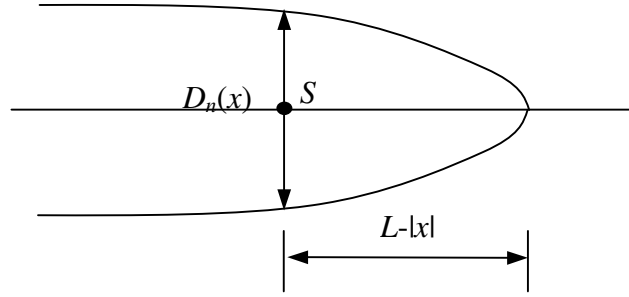


Figure 24. Sketch for stress intensity factor calculation

In this thesis we use the point  $S$  at  $(0.88, 0)$ , where  $(L - |x|)/L = 12\%$ . As mentioned above, the calculated crack opening  $D_n(x)$  is least accurate near the tip. Previous discussions show that  $D_n(x)$  at this point yields an acceptable error of about 5%. As a result of, this point is chosen to calculate the SIF. The SIF is normalized by

$$\hat{K}_I = \frac{K_I}{|P|}, \text{ where } P = -\sigma_n \text{ in mode I loading.}$$

The short-term value (initial value) of the SIF is given by (Detournay and Cheng, 1991):

$$\hat{K}_I(0^+) = \frac{1 - \nu_u}{1 - \nu} \sqrt{\pi L} \quad (59)$$

The long-term value (final value) of the SIF is (Detournay and Cheng, 1991):

$$\hat{K}_I(\infty) = \sqrt{\pi L} \quad (60)$$

The evolution of the normalized SIF with time is plotted in Figure 25 with closed forms for initial and final values. It shows that the DD models can predict accurate SIF values. In order to compare with crack SIFs under other loading modes, the plot of the absolute value of SIF vs. time is shown in Figure 26.

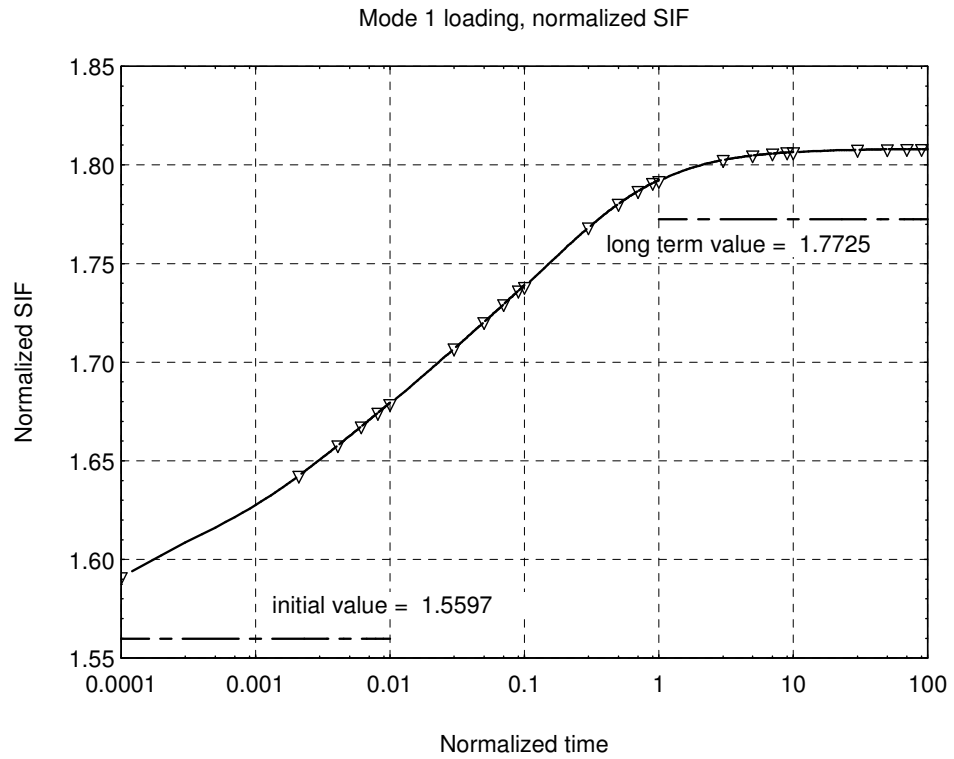


Figure 25. Normalized crack stress intensity factor under stress loading



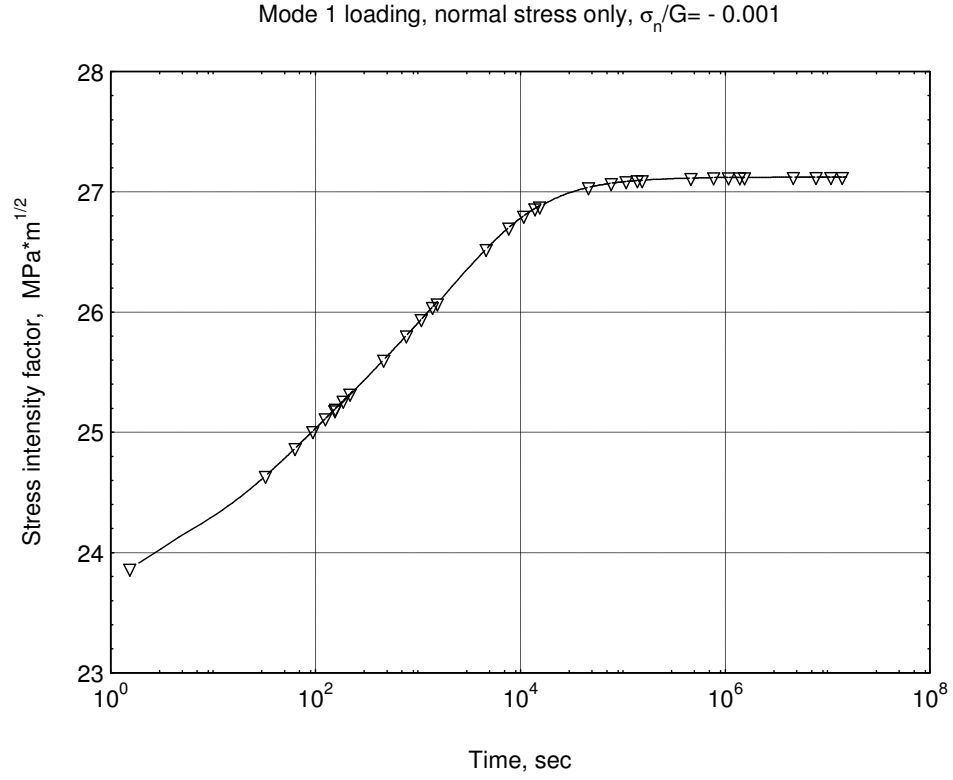


Figure 26. Crack stress intensity factor under stress loading

### *Mode 2: Pore Pressure Loading*

#### Maximum Crack Opening

In mode 2, the maximum normalized opening is defined as:

$$(\hat{D}_n)_{\max} = \frac{D_n(0,t)G}{|P|L} \quad (61)$$

The crack closes progressively, starting from a zero displacement discontinuity at time  $t=0^+$ . The final value of the normalized maximum opening  $(\hat{D}_n)_{\max}$  is given by (Vandamme et al, 1989):

$$(\hat{D}_n)_{\max} = -2\eta(1-\nu) \quad (62)$$

where  $\eta$  is the poroelastic stress parameter defined as  $\eta = \frac{3(\nu_u - \nu)}{2B(1 + \nu_u)(1 - \nu)}$ .

Normalized maximum opening in Mode 2 loading is illustrated in Figure 27. As can be seen, the crack closes with time. Because the two crack surfaces will not overlap, this closure is physically possible only if the crack remains open, under appropriate combination of Mode 1 and Mode 2 loading. The comparison between the DD solution and the close solution is good. Small discrepancy develops at large time simulation. The numerical results are lower than the long-term close form, because the later one represents the ideal state of complete draining out of the formation, which actually is impossible for the assumed infinite media. Vandamme et al (1989) observed comparable error in their work.

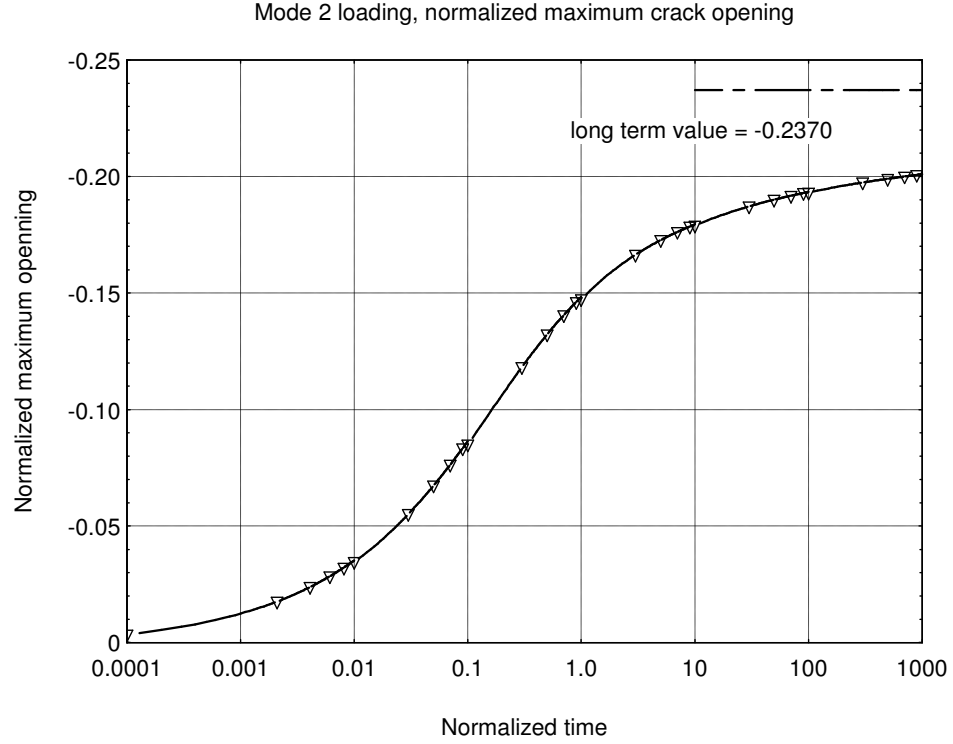


Figure 27. Normalized crack maximum opening under pore pressure loading

### Stress Intensity Factor

SIF is computed using displacement method. There is no displacement on the crack surface induced by Mode 2 at time  $t=0^+$ , so the initial value of the SIF is zero. The final value of normalized SIF is given by (Detournay and Cheng, 1991)

$$\hat{K}_1(\infty) = -\eta\sqrt{\pi L} \quad (63)$$

The calculated SIF is normalized using  $\hat{K}_1 = \frac{K_1}{|P|}$ . Figure 28 shows a plot of the normalized SIF with time. A small divergence between the DD solution and the close form solution is developing near the end. This is partly because the close form solution represents the ideal “completely drained” condition, which is actually impossible to reach

numerically. Also note in this thesis, constant-strength elements are adopted through all the calculations. Detournay and Cheng (1991) got better result for long-term SIF calculation by using edge dislocation solution and tip element. Figure 29 plots the absolute value of SIF changing with time under pressure loading.

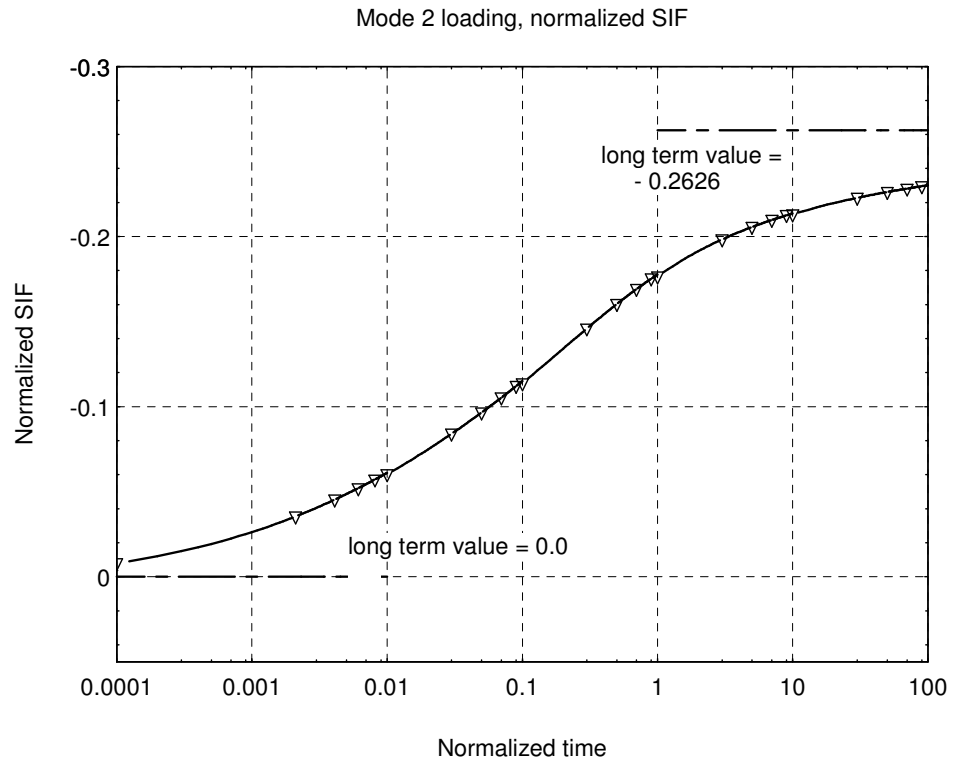


Figure 28. Normalized crack stress intensity factor under pore pressure loading

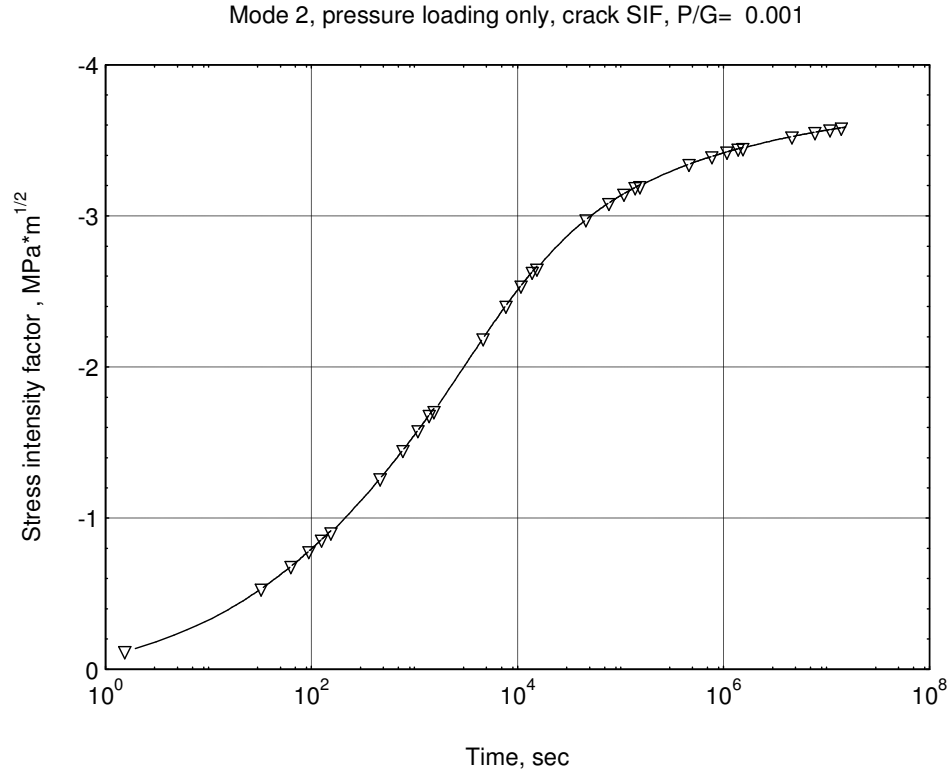


Figure 29. Crack stress intensity factor under pore pressure loading

### Crack Under Thermal Loading

Consider a crack of length  $2L$  subject to a sudden uniform temperature change (cooling or heating) on its surface as shown in Figure 30. This problem can be solved by DD model. In this example, the hot formation of Westerly Granite at  $T_0 = 200^\circ\text{C}$  is gradually cooled down by keeping the crack temperature constant at  $T_c = 0^\circ\text{C}$ . Far field stresses and pore pressure are assumed to be zero thus there are no stress or pressure loading on the crack surface.

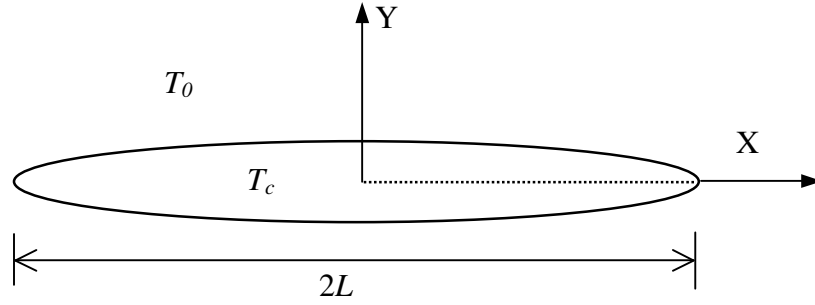


Figure 30. A crack under thermal loading

### *Maximum Crack Opening*

Maximum opening of the crack is plotted as a function of time in Figure 31. It can be seen that the crack gradually opens as time increases and finally tends to reach an asymptotic value in the long run given by:

$$(D_n)_{\max} = -\frac{2\beta_s L(1+\nu)}{3} \Delta T \quad (64)$$

where  $\Delta T = -200^\circ\text{C}$ . Derivation of equation (93) can be found in Appendix B. The crack response can be explained by the contraction of the formation material, due to cooling, pulls the crack surface to opposite directions and gradually opens it up.

The maximum crack opening predicted by this thermo-poroelastic solution is the same with the one calculated by the thermoelastic solution, as shown in Figure 32. This is because although the cooling process induces a pore pressure reduction in the formation, the induced pore pressure reduction is zero at the crack surfaces thus has no impact on the crack opening. That is to say, if no hydraulic loading applied on the boundary, thermo-

poroelastic solution and thermoelastic solution will give the same result on crack width prediction.

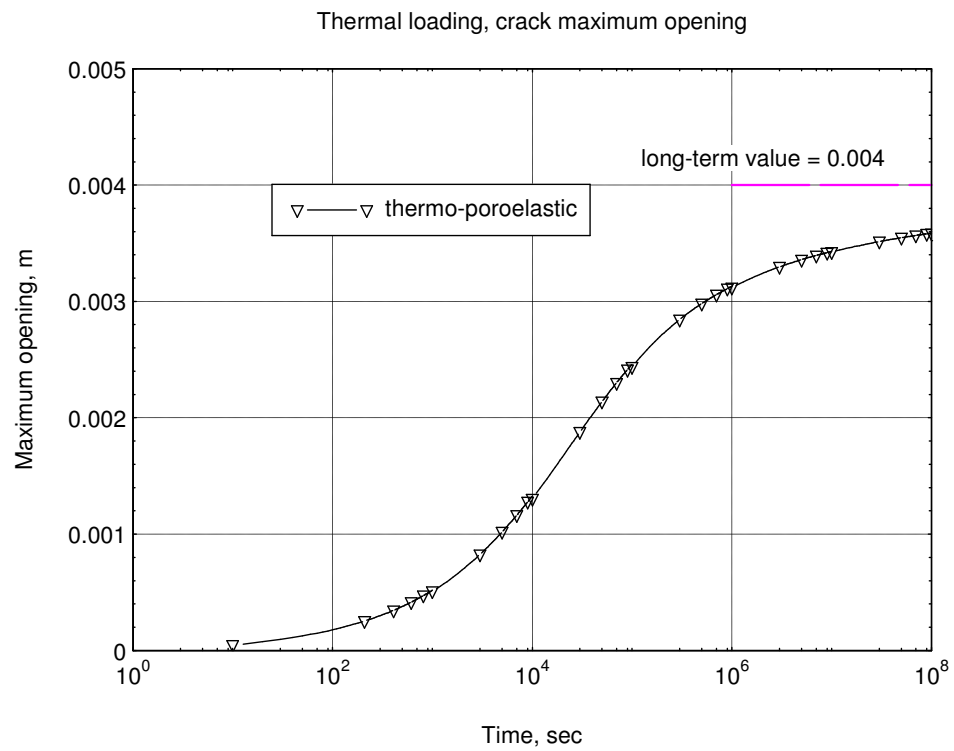


Figure 31. Maximum crack opening under cooling condition, thermo-poroelastic solution

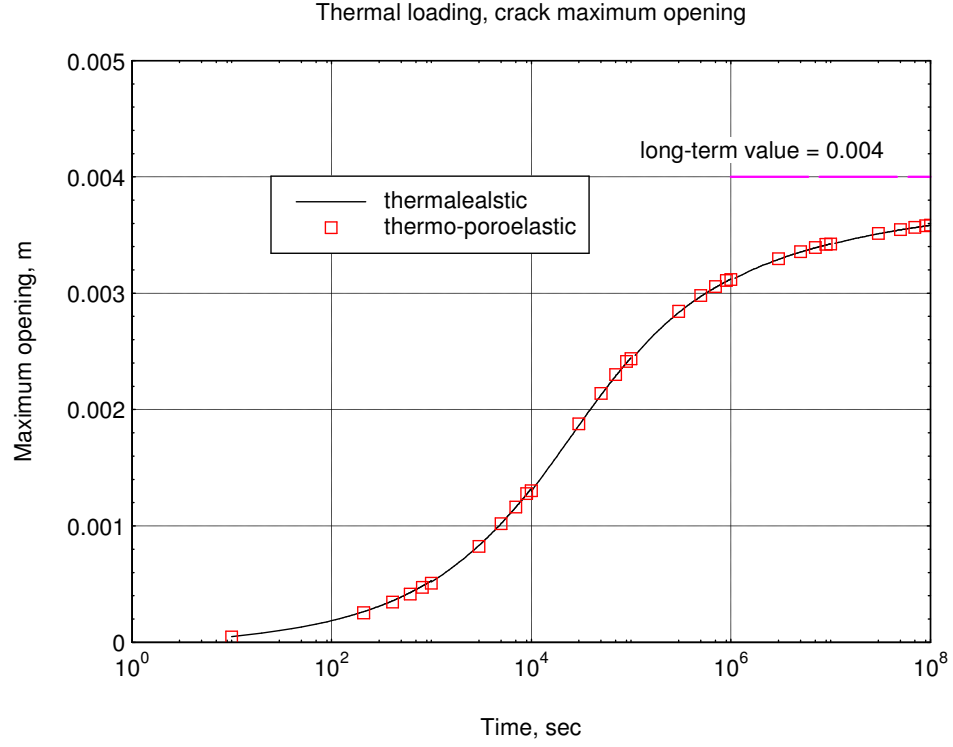


Figure 32. Maximum crack opening under cooling condition, thermo-poroelastic solution and thermoelastic solution

### *Stress Intensity Factor*

The stress intensity factor induced by cooling the crack surfaces is plotted in Figure 33. It indicates that cooling will increase SIF, which means higher potential of fracture propagation is expected. As time increases, the SIF will approach to a steady state value, given by:

$$K_1(\infty) = -\frac{E\beta_s}{6(1-\nu)} \Delta T \sqrt{\pi L} \quad (65)$$

where  $\Delta T = -200^\circ\text{C}$ . Derivation of equation (65) is shown in Appendix B.



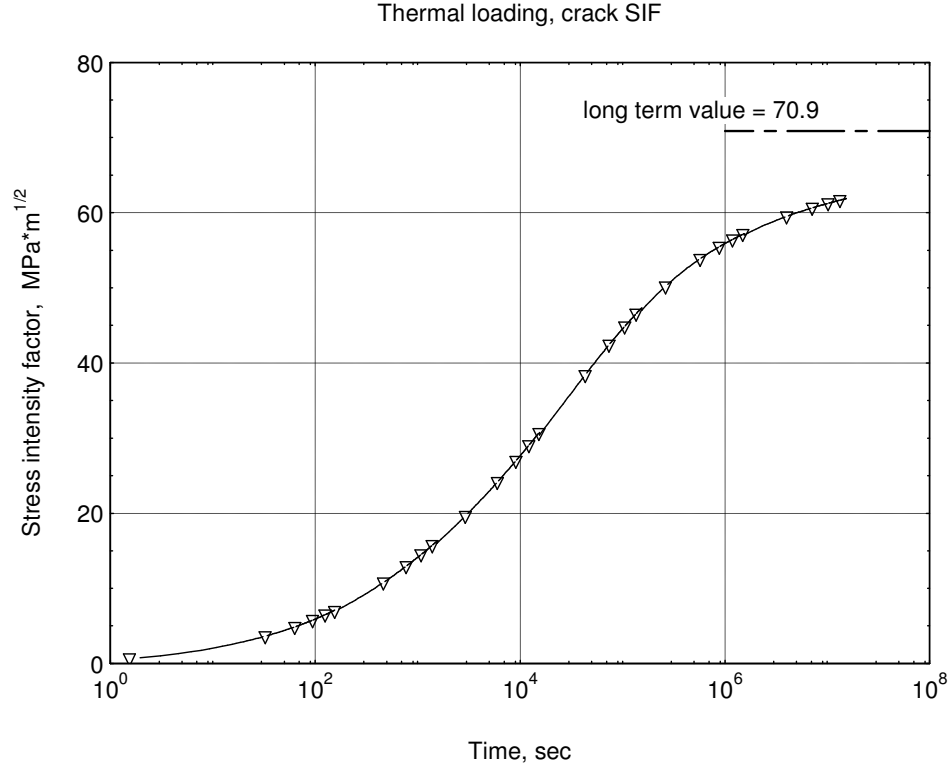


Figure 33. Crack stress intensity factor under cooling condition

By comparing Figure 33 with Figure 26 and 29, one can see that the long-term SIF due to cooling from 200°C to 0°C is much larger than those under mechanical or hydraulic loading of magnitude  $P = G/1000$ . Figure 34 plots the normalized crack SIF under thermal loading. The SIF value is normalized with respect to the initial SIF value under mode 1 loading, which is given by  $K_1(0^+) = \frac{1-\nu_u}{1-\nu} P\sqrt{\pi L} = 23.3 \text{ MPa}\cdot\text{m}^{1/2}$ . It indicates that the long-term value of crack SIF under thermal loading  $\Delta T = -200^\circ\text{C}$  is about 3 times of the instantaneous crack SIF under the pressurization of 15 MPa. Therefore cooling can significantly increase the crack SIF, which means a much higher potential of crack propagation.

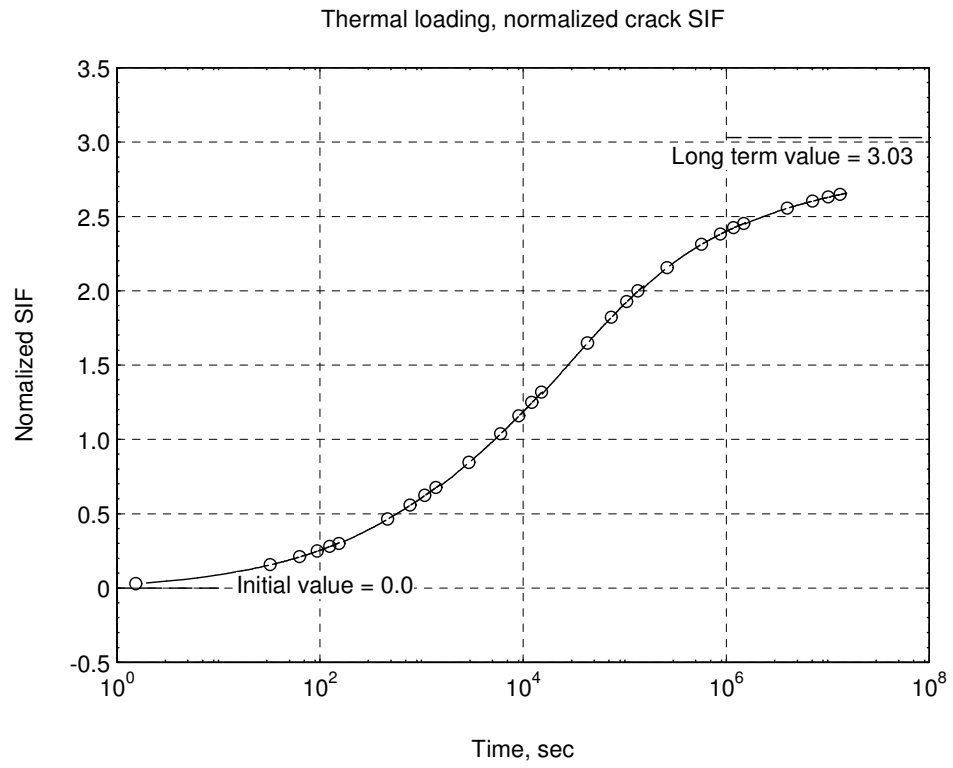


Figure 34. Normalized crack stress intensity factor under cooling condition

## Borehole With Pre-existing Cracks

In order to test the combine FS-DD method, two examples are considered in this section.

### *Tangential Stress Near a Borehole Intersected By a Crack*

As shown in Figure 35, a borehole is intersected by a crack. Both the borehole wall and the crack surfaces are pressurized by  $p$ . The far field stress field is assumed to be zero. The length of the crack  $a$  equals to the well radius  $r$ . This problem is solved using the combined FS-DD model. The borehole boundary is divided by 50 FS element, whereas the crack is divided by 14 DD elements. In Figure 36, distribution of tangential stress (normalized by  $\sigma_{\theta\theta}/p$ ) near the borehole is examined along line AB.

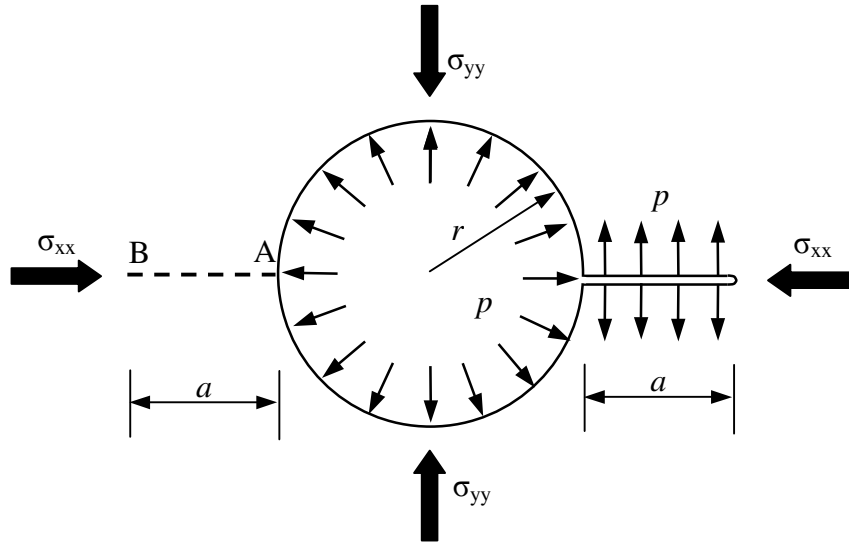


Figure 35. Pressurization of a crack intersecting a borehole

As can be seen in Figure 36, the result predicted by the combined FS-DD model agrees well with the finite element solution obtained by Vijayakumar and Curran (2003). The tangential stress in the area close to the borehole boundary can be calculated with considerable accuracy by the combined FS-DD model. At the point where the distance from the borehole wall is 1/50 of the radius, the difference between the combined FS-DD model and the FEM solution is less than 3%.

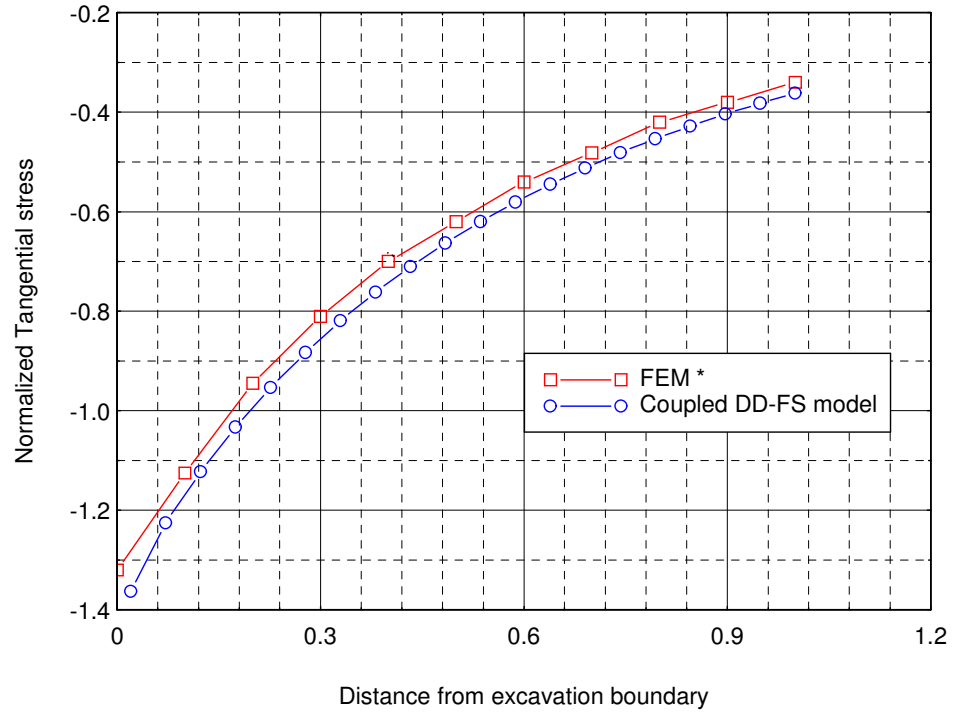


Figure 36. Tangential stress near a borehole intersected by a crack

### *Stress Intensity Factor of Cracks Intersecting with a Borehole*

In order to study the fracture behavior near a borehole, the stress intensity factors need to be analyzed. To test the functionality of the combined FS-DD model for this problem, eight different cases of cracked borehole are studied. As shown in Figure 37-40, borehole radius is  $r$ , crack length is  $a$ .  $\sigma$  is field stress magnitude (hydrostatic stress field is assumed in order to simplify the problems).  $p$  is the pressure applied on boundary. Eight cases are formed from the combination of stress pattern and problem geometries. For each case, the values of the input data are shown in Table 2 together with the SIF computed by the model and the results are compared with the solutions given by Sih (1973).

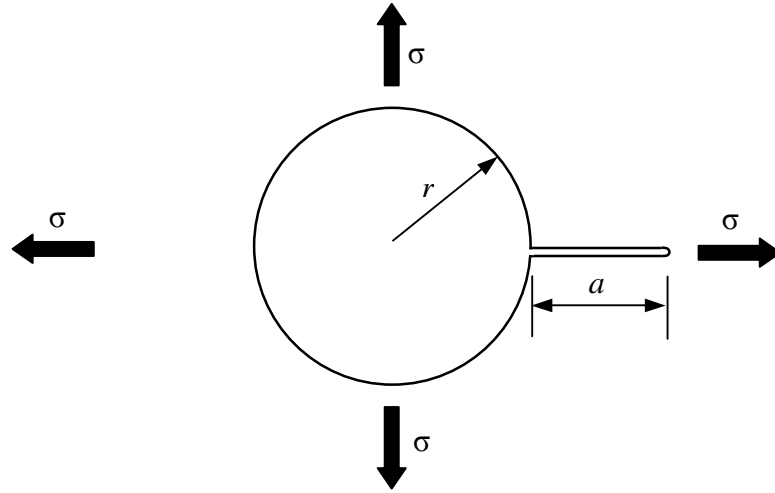


Figure 37. A borehole intersected by a crack, under biaxial tension

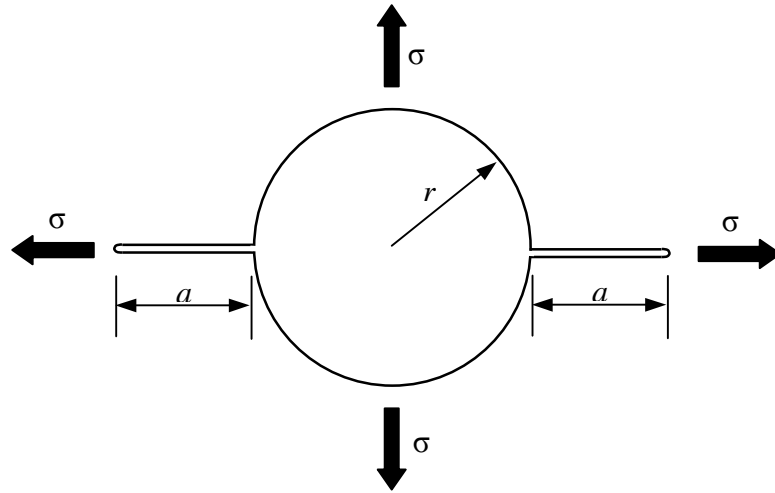


Figure 38. A borehole intersected by two cracks, under biaxial tension

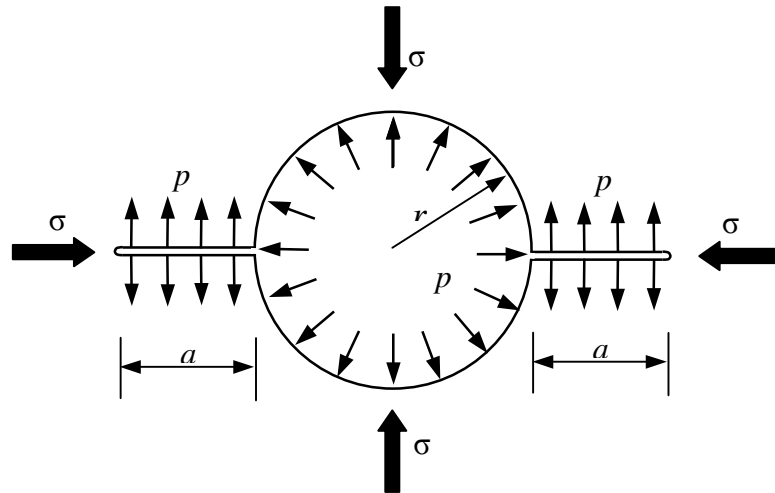


Figure 39. A borehole intersected by two cracks, under internal pressurization on both borehole and crack

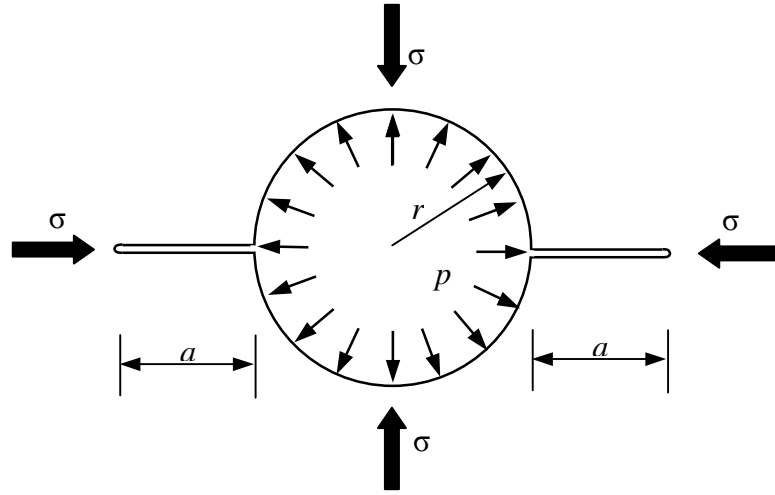


Figure 40. A borehole intersected by two cracks, under internal pressurization on borehole only

From Table 2, it can be seen that the stress intensity factors computed by the combined FS-DD model agree well with the solutions provided by Sih (1973). The largest error generated in these eight cases is an acceptable 3.8%. Therefore, one can assume the model is accurate enough to compute crack SIF near a borehole. Based on the study of the stress/displacement singularity around the crack tip, fracture propagation behaviour can then be further examined using this model.

Table 2. Stress intensity factor of cracks intersecting with a borehole

Case #	Description	Input data	Results of Combine FS-DD model ( $\text{Pa}\cdot\text{m}^{1/2}$ )	Solutions from reference ( $\text{Pa}\cdot\text{m}^{1/2}$ )
1	See Figure 37	$r = 0.1 \text{ m}$ $a = 0.1 \text{ m}$ $\sigma = 30 \text{ MPa}$	2.06822E+07	2.0514E+07
2	See Figure 37	$r = 0.1 \text{ m}$ $a = 0.2 \text{ m}$ $\sigma = 30 \text{ MPa}$	2.45140E+07	2.4018E+07
3	See Figure 38	$r = 0.1 \text{ m}$ $a = 0.1 \text{ m}$ $\sigma = 30 \text{ MPa}$	2.30665E+07	2.3205E+07
4	See Figure 38	$r = 0.1 \text{ m}$ $a = 0.05 \text{ m}$ $\sigma = 30 \text{ MPa}$	1.79650E+07	1.8667E+07
5	See Figure 39	$r = 0.1 \text{ m}$ $a = 0.1 \text{ m}$ $\sigma = 0 \text{ MPa}$ $p = 30 \text{ MPa}$	2.30665E+07	2.2995E+07
6	See Figure 39	$r = 0.1 \text{ m}$ $a = 0.05 \text{ m}$ $\sigma = 0 \text{ MPa}$ $p = 30 \text{ MPa}$	1.79647E+07	1.8594E+07
7	See Figure 40	$r = 0.1 \text{ m}$ $a = 0.1 \text{ m}$ $\sigma = 0 \text{ MPa}$ $p = 30 \text{ MPa}$	6.97829E+06	6.7797E+06
8	See Figure 40	$r = 0.1 \text{ m}$ $a = 0.05 \text{ m}$ $\sigma = 0 \text{ MPa}$ $p = 30 \text{ MPa}$	7.19040E+06	6.9670E+06



## CHAPTER 5

### ROCK MECHANICS APPLICATIONS

In this chapter, the boundary element model is applied to several problems of interest in applied rock mechanics. Pore pressure and stress fields around underground openings are examined under coupled hydro-thermo-mechanical loading. The rock type used in this chapter is Westerly Granite except for the first example in which a Shale is considered.

#### Influence of Borehole Geometry on its Stability

The influence of excavation geometry on borehole stability is considered in this section. The motivation for this problem is the fact that many boreholes tend to become elliptical, i.e.,  $a/b = C \neq 1$  (Figure 41) under the influence of the in-situ stresses (Aadnoy and Angell-Olsen, 1995). The safe density of the mud to be used is affected by the stress concentrations around the borehole. Therefore, mud support calculations based on a circular ( $C=1$ ) geometry may cause problems. Furthermore, future fracturing operations are also affected by the change in the hole geometry.

Rock material used in this example is assumed to be Gulf of Mexico Shale. Input parameters are listed in Table 3 (Data are taken from Cui et al., 1998). Due to symmetry of this problem, only a quarter of the borehole wall is modeled using 10 elements. The magnitude of the in-situ major and minor horizontal stresses and pore pressure is

assumed to be 29, 20, and 10 MPa, respectively. Formation temperature is assumed to be 200°C. Normal stress and mud pressure applied at the borehole wall are both 15 MPa. Mud temperature is 0°C. The elliptical ratio  $a/b$  is assumed to be 1.1.

Figure 42 compares the effective hoop stress for circular and elliptical cases. At  $t = 10^2$  sec, the ellipticity increases the magnitude of the compressive effective tangential stress induced near the x-axis (from 0-20 degrees); and increases the magnitude of the tensile effective tangential stress near the y-axis (from 70-90 degrees). The implication is that at early time, an elliptical borehole will be more likely to fail in tension due to the pressure of the mud column and cooling. Hence a mud with a higher temperature and/or lower density than that for a circular well need be used. The situation is reversed if the ellipticity were to occur in the opposite orientation. At  $t = 10^6$  sec, the ellipticity slightly increases the magnitude of the compressive effective tangential stress near the x-axis (from 0-10 degrees); while it decreases the magnitude of the tensile effective tangential stress near the y-axis (from 75-90 degrees). This means that the ellipticity does not contribute to the tensile failure at long time in this case.

Figure 43 shows the effective hoop stress for circular borehole under poro-mechanical loading. It can be seen that the compressive effective hoop stress increases near the x-axis (from 0 to 35 degrees) while decreases near the y-axis (from 50 to 90 degrees). This effect is caused by the deviatoric stress loading and its impact was apparent in the previous figure and discussion.

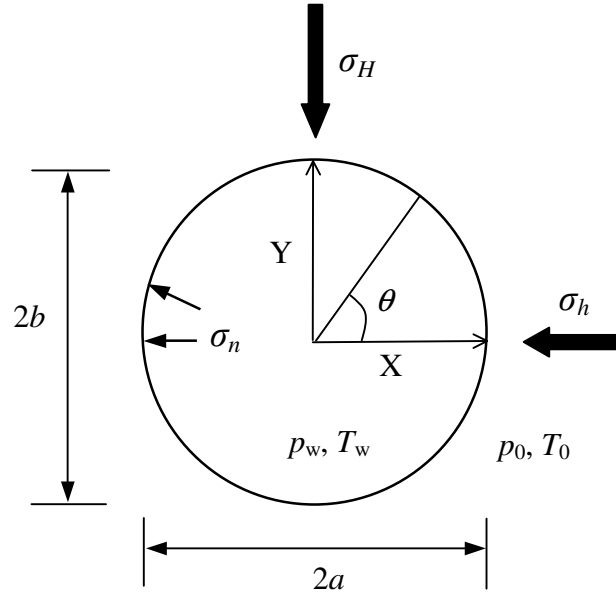


Figure 41. A borehole under combined poro-thermo-mechanical loading

Table 3. Input parameters for Gulf of Mexico Shale

Variable	Physical meaning	Value	Unit
$E$	Modulus of elasticity	$2.06 \times 10^4$	MPa
$\nu$	Poisson's ratio	0.20	-
$\nu_u$	Undrained Poisson's ratio	0.31	-
$K_s$	Solid bulk modulus	$4.8 \times 10^4$	MPa
$K_f$	Fluid bulk modulus	$2.5 \times 10^3$	MPa
$c^T$	Thermal diffusivity	$1.6 \times 10^{-6}$	$M^2/sec$
$C$	Heat capacity	$1.17 \times 10^6$	Joule/(kg·°C)
$\beta_s$	Solid thermal expansion coef.	$1.8 \times 10^{-5}$	1/°C
$\beta_f$	Fluid thermal expansion coef.	$3.0 \times 10^{-4}$	1/°C
$n$	Porosity	0.143	-
$\gamma_f$	Unit weight of fluid	$9.8 \times 10^3$	N/m <sup>3</sup>
$k$	Intrinsic permeability	$7.66 \times 10^{-8}$	Darcy
$B$	Skempton's constant	0.551	-
$\mu$	Fluid viscosity	$3.547 \times 10^{-4}$	kg/(m·sec)

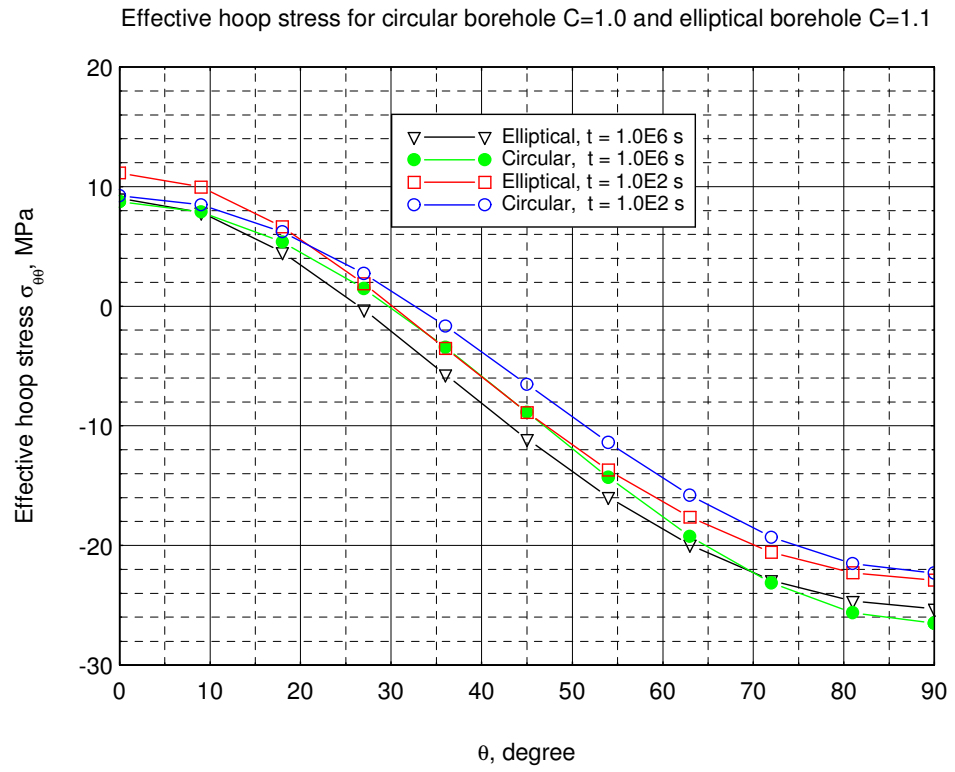


Figure 42. Effective hoop stress around a circular borehole and an elliptical borehole

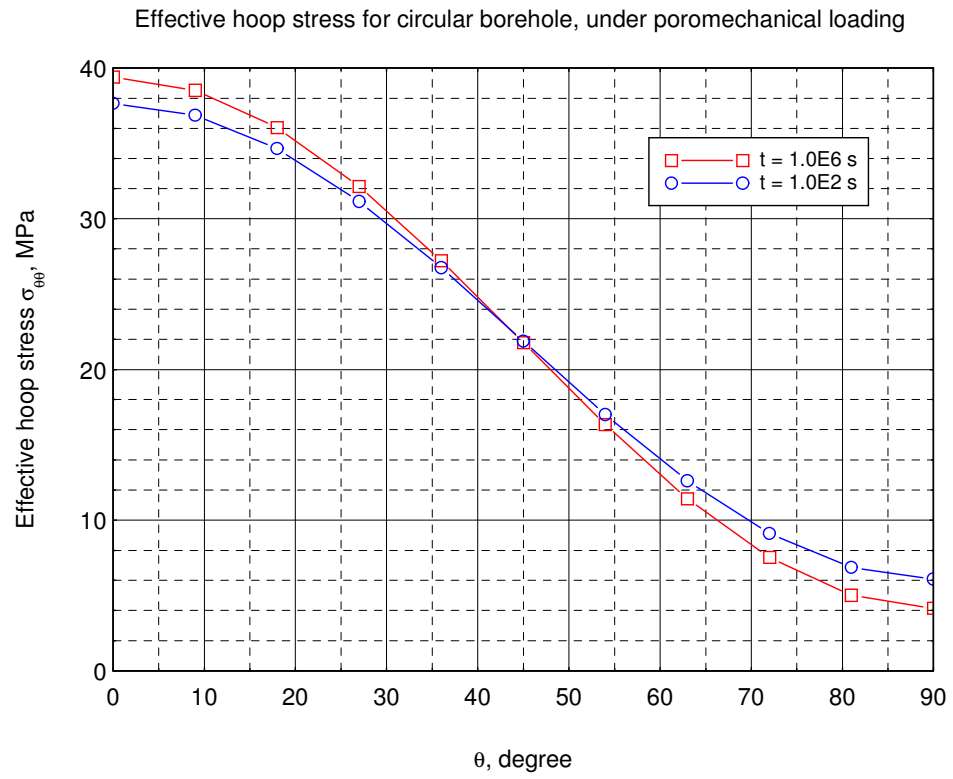


Figure 43. Effective hoop stress around a circular borehole, under poro-mechanical loading

## Drilling-induced Tensile Failure

As shown before, drilling a borehole will change the stress field and pore pressure field dramatically. This section analyzes the conditions of tensile failure induced by borehole drilling. Consider a borehole (Well 38B-9) drilled in Coso geothermal field (Sheridan et al., 2003) at a depth of 7800 ft, as shown in Figure 41. The magnitude of the in-situ major and minor horizontal stresses and pore pressure is assumed to be 67.33, 21.97, and 17.93 MPa, respectively. The formation temperature is 250°C. Normal stress and mud pressure applied at the borehole wall are 25.81 MPa. Mud temperature is 50°C. Considering the problem symmetry, 10 FS elements are used to simulate a quarter of the circular borehole wall.

Figure 44 illustrates the effective hoop stress field at  $t = 10$  hours. One sees that large tensile stresses are induced on the opposite sides of borehole wall at the azimuth of major in-situ stress. In these two areas, tensile fractures are very likely to occur in the borehole wall when the effective hoop stress exceeds the tensile strength of the rock. In fact, a tensile fracture has been observed at this depth. The fracture will initialize on the wall because it is where the tensile stress is the largest. Also note that at the azimuth of the minor in-situ stress, the compressive hoop stress is greatest, which means borehole breakouts will occur when the compressive stress concentration exceeds the rock strength.

Figure 45 shows the effective radial stress field. A tensile stress zone is formed inside the formation, which encourages tensile fracturing in the circumferential direction.

In this example, both excess mud pressure and borehole cooling influence the occurrence of drilling induced tensile fractures because both cause additional tensile stress to the hoop stress acting around the borehole.

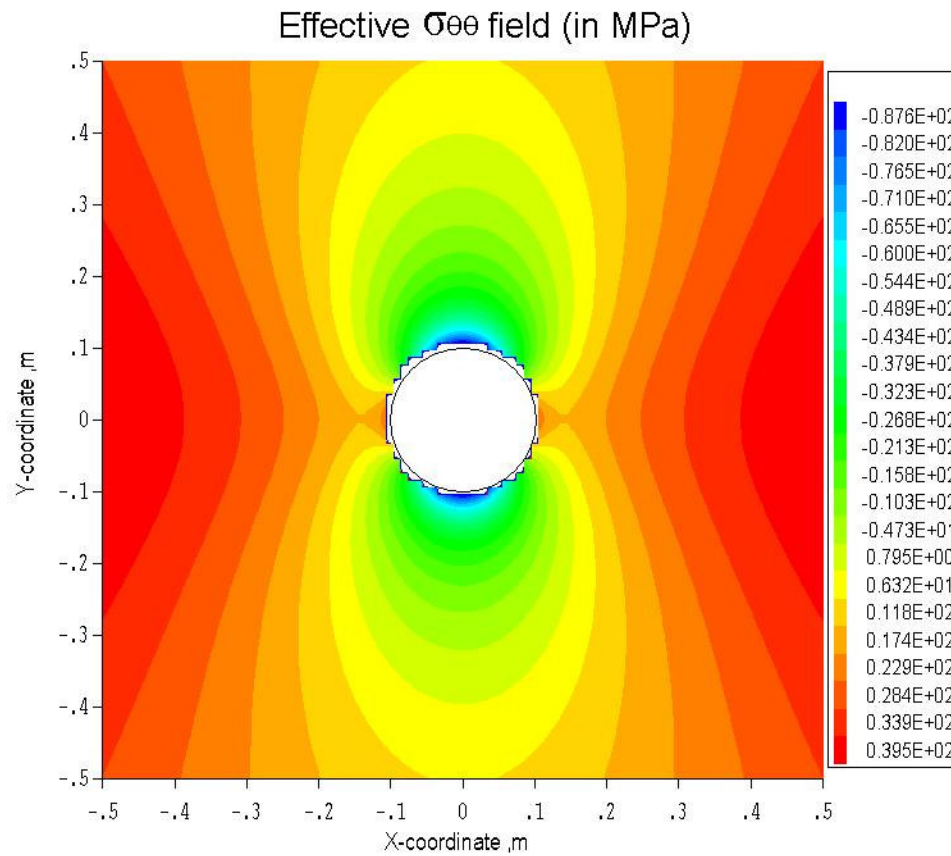


Figure 44. Effective hoop stress field induced by borehole drilling

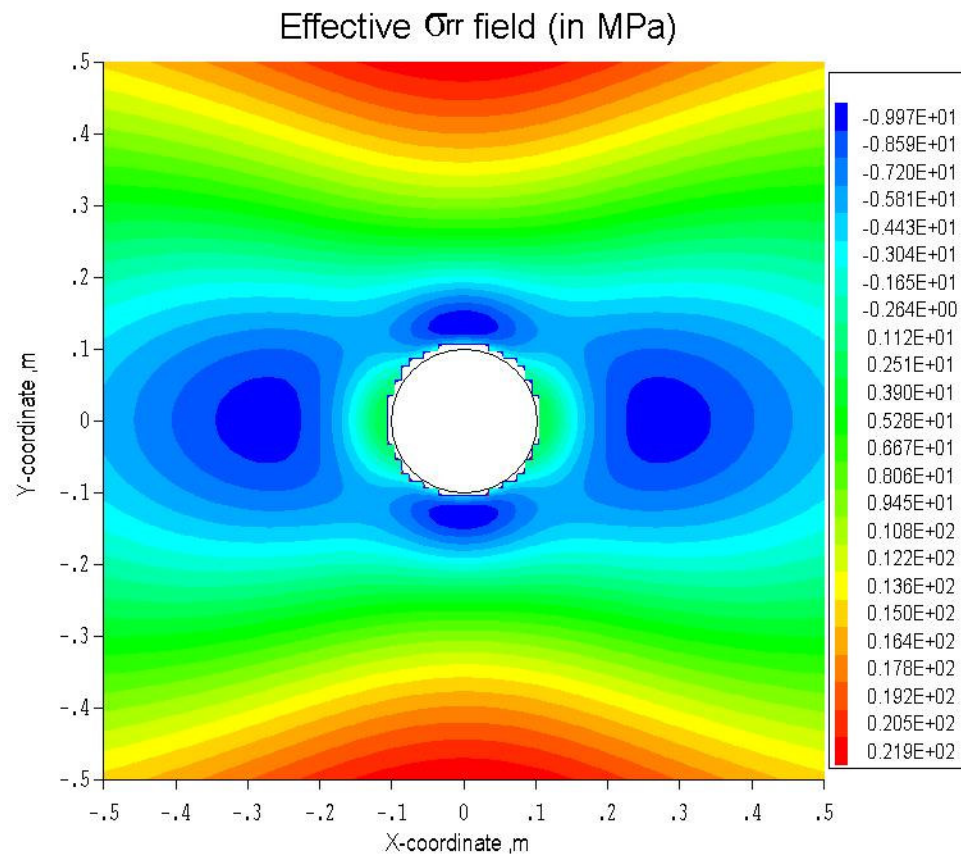


Figure 45. Effective radial stress field induced by borehole drilling



### Influence of Thermal Stress on Injection Well Fracturing

During waterflooding or other recovery processes, fluids such as water are injected into the reservoir through a well. Typically the temperatures of the injected fluids are cooler than the in-situ reservoir temperature (Perkins and Gonzalez, 1985). With time, a zone of cooled rock forms around the injection well. If the injection condition is such that the formation is fractured hydraulically, the cooled zone will also evolve in geometry accordingly. Thermally induced stresses result in an additional tensile stress field around the well and the fractures. As a result, the magnitudes of in-situ stresses in the cooled zone are decreased. Thus the pressure required to fracture the formation is reduced.

When the injection rate is high enough, the effective tangential stress around the well will exceed the tensile strength of the formation, as a result a short fracture perpendicular to the direction of the minor in-situ stress will extend from the well, as shown in Figure 46.

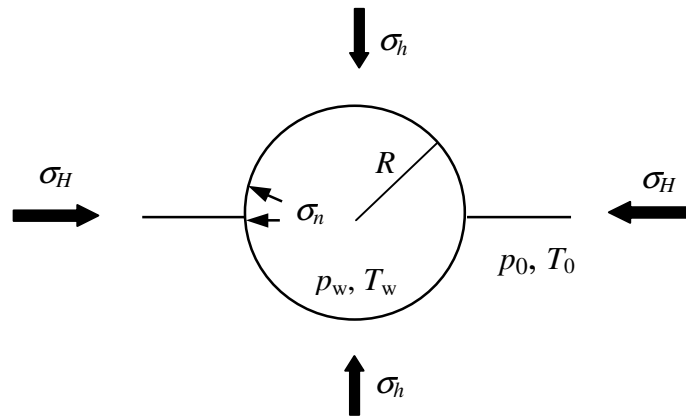


Figure 46. Hydraulic fracturing of an injection well

Consider injecting water of  $0^{\circ}\text{C}$  into a well of radius  $R = 0.1\text{m}$  drilled in a formation at a temperature of  $200^{\circ}\text{C}$ . Assume the current length of the fracture is now  $0.5R$ . In order to examine the impact of the thermally induced stress only, the mechanical and hydraulic loadings are not considered. That is to say, the in-situ stresses and pore pressure are assumed to be zero, so are the stresses and pressure applied on the well boundary and the fracture surface. Figure 47 plots the temperature field at time  $= 10^5$  sec. As shown in Figure 47, the cooled region around the well and the short fracture is nearly circular, although slightly elliptical. Figure 48 shows the difference of major and minor principle stress induced by cooling. One can see the differences of thermally induced stresses in two principle directions are very small in the cooled region illustrated by the dashed ellipse. This leads to the conclusion that the magnitudes of thermally induced stresses (which is also the reduction of the in-situ stresses) are nearly uniform in all directions. Therefore, for actual cases where the in-situ stresses are applied, the direction of the minor in-situ stress remains the same as that initially in the formation. And consequently the orientation of the fracture will also remain the same.

Now, consider another case when the injection rate is much higher, thus the fracture extends a greater distance from the well. In this example, the length of the fracture is supposed to be  $14R$ . The cooled region becomes more elongated in shape, as shown in Figure 49. At time  $= 10^5$  sec, the temperature of the region shown in the dashed ellipse is approximately under  $100^{\circ}\text{C}$ . Figure 50 plots the difference between major and minor principle stress induced by cooling. Mechanical and hydraulic loadings are not considered. The plot indicates that the difference between the magnitudes of thermally

induced stresses parallel and perpendicular to the fracture is much larger in the cooled region than outside. That is to say, in the elliptical cooled region, the thermoelastic reduction of the in-situ stress parallel to the fracture ( $\Delta\sigma_H$ ) is much greater than the thermoelastic stress reduction perpendicular to the fracture ( $\Delta\sigma_h$ ). Let  $a$  to be the length of the long axis of the ellipse in the direction of  $\sigma_H$ , and  $b$  to be the length of the short axis in the direction of  $\sigma_h$ , then the expressions for  $\Delta\sigma_H$  and  $\Delta\sigma_h$  can be given by (Perkins and Gonzalez, 1985):

$$\Delta\sigma_H = -\frac{1}{(1 + b/a)} \cdot \frac{E\beta_s\Delta T}{3(1-\nu)} \quad (66)$$

$$\Delta\sigma_h = -\frac{b/a}{(1 + b/a)} \cdot \frac{E\beta_s\Delta T}{3(1-\nu)} \quad (67)$$

According to equation (66) and (67), at the crack surface where the  $\Delta T$  is  $-200^\circ\text{C}$ , the difference between  $\Delta\sigma_H$  and  $\Delta\sigma_h$  can be 78 MPa for an ellipse with axis ratio of  $b/a = 0.01$ , and 56 MPa for  $b/a = 0.1$ . The value could be lower inside the formation because the temperature change ( $\Delta T$ ) there is not as high as at the crack surface.

The effect of the elongated cooled region is further illustrated by the following example. Let the geometries of the well and the fracture remain the same. Assume the in-situ major and minor stresses and pore pressure are 40 MPa, 10 MPa and 10 MPa, respectively. As mentioned before, the direction of the minor principle stress is perpendicular to the fracture. The normal stress and pressure applied on the well boundary and fracture surfaces are 10 MPa and 10MPa, respectively. Thermal loading remains the same with previous example, which is cooling on the wellbore from  $200^\circ\text{C}$  to  $0^\circ\text{C}$ . Therefore, the temperature field and cooled region at time =  $10^5$  sec is the same as

the one shown in Figure 49. The difference between the total major and minor principle stresses is plotted in Figure 51. One can see that in the cooled region, the difference between the total major and minor principle stresses is reduced greatly. Note that the original difference of the principle stresses is 30 MPa everywhere, and with cooling it is reduced to less than 10 MPa in most areas of the cooled region. Exceptions occur in two cases: when the examined points are in the vicinity of the wellbore, where stresses fields are significantly affected by the mechanical boundary conditions; when the examined points are in the areas near the fracture ends, where stress singularity happens.

When the fracture extends further, a flatter shape of cooled region would form around the whole system. This would cause the stresses parallel to the fracture to become less than those perpendicular to the fracture. As a result, secondary fractures perpendicular to the primary main fracture will open in this situation, as shown in Figure 52 (Perkins and Gonzalez, 1985).

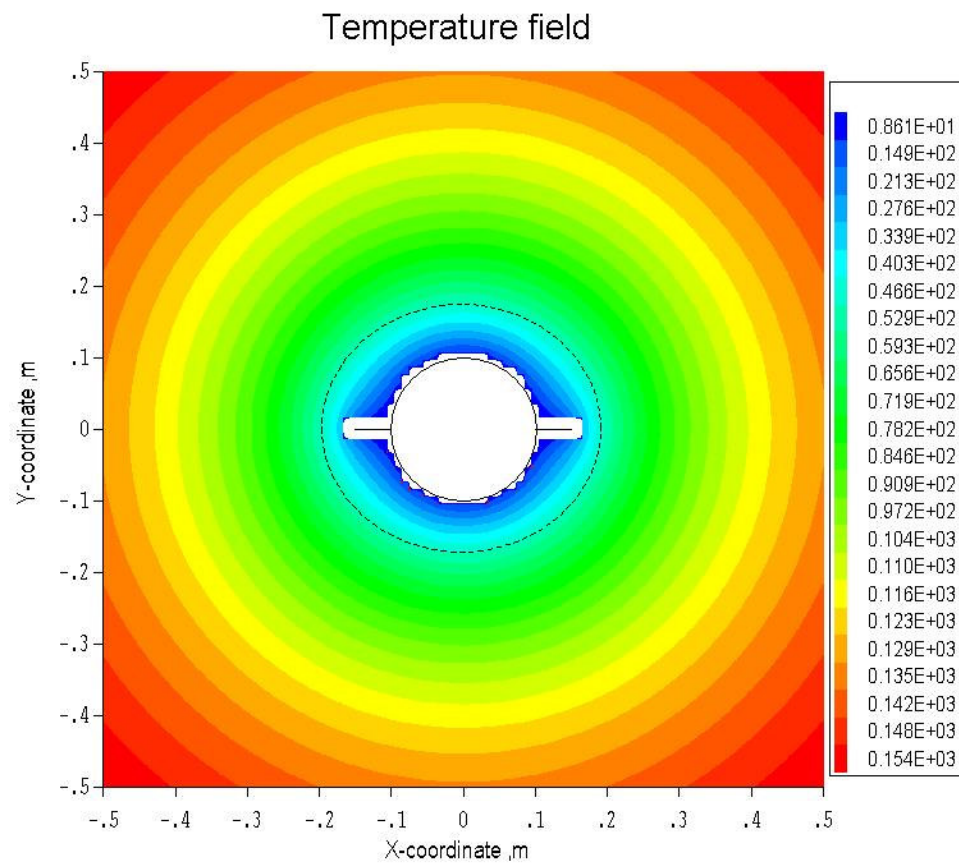


Figure 47. Temperature field around an injection well and a short fracture

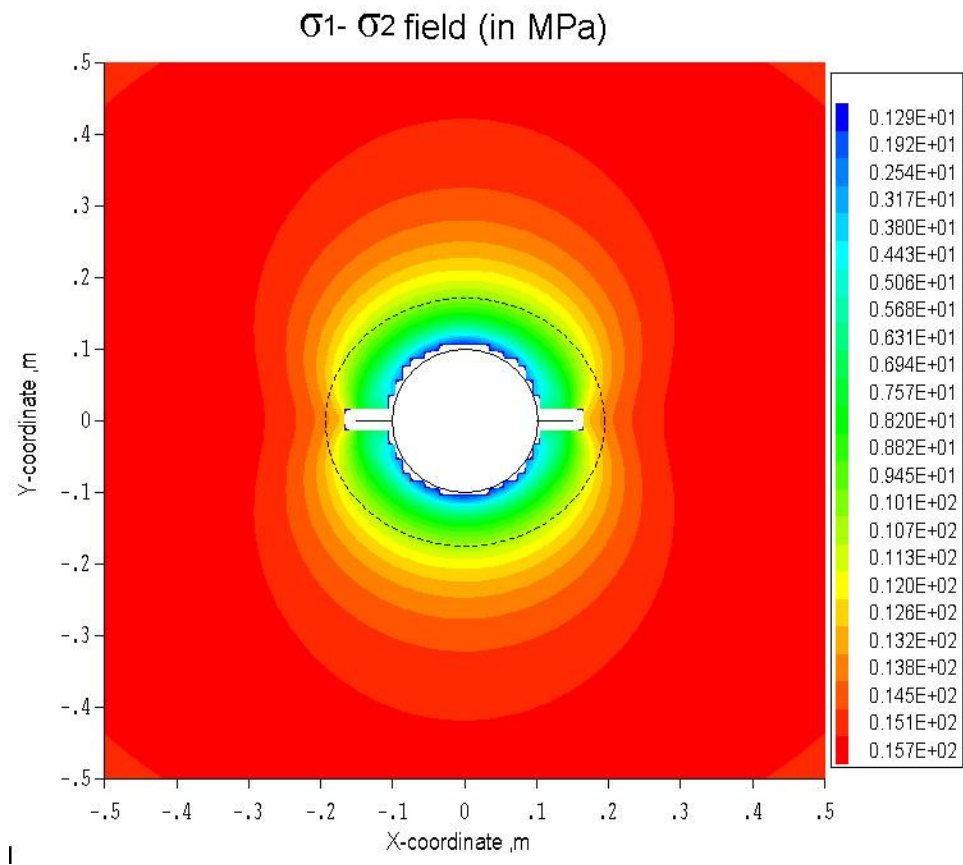


Figure 48. Difference between thermally induced principle stresses around an injection well with a short fracture

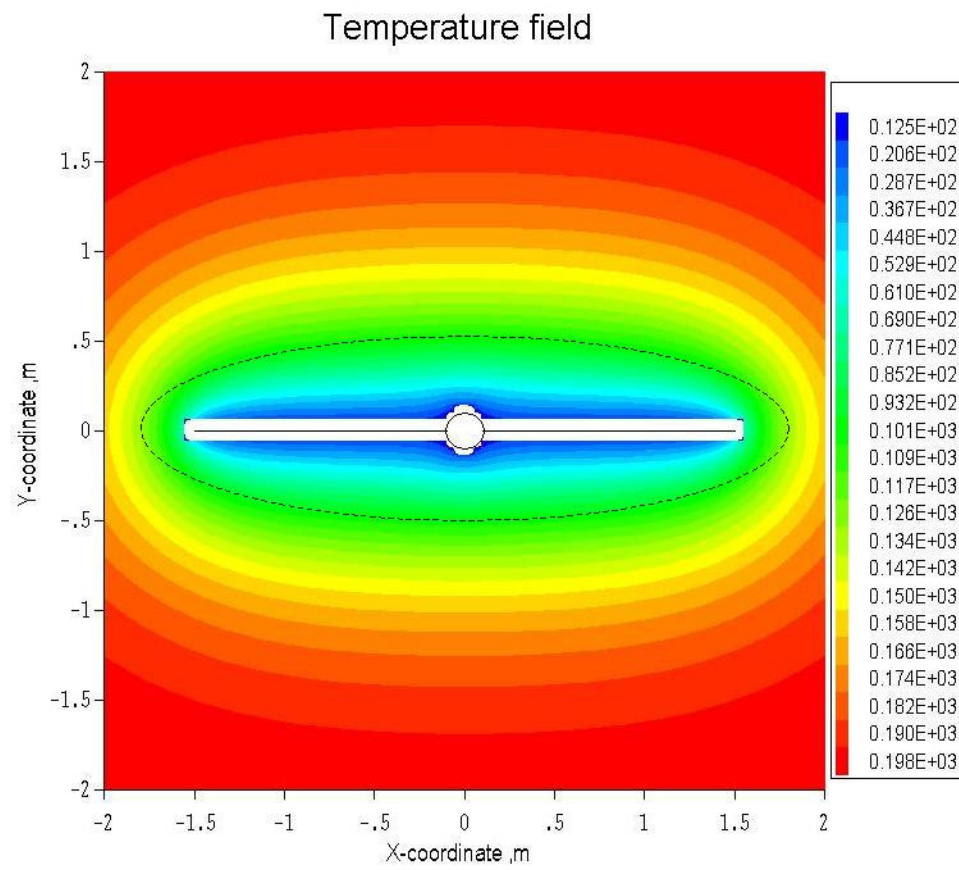


Figure 49. Temperature field around an injection well and a long fracture

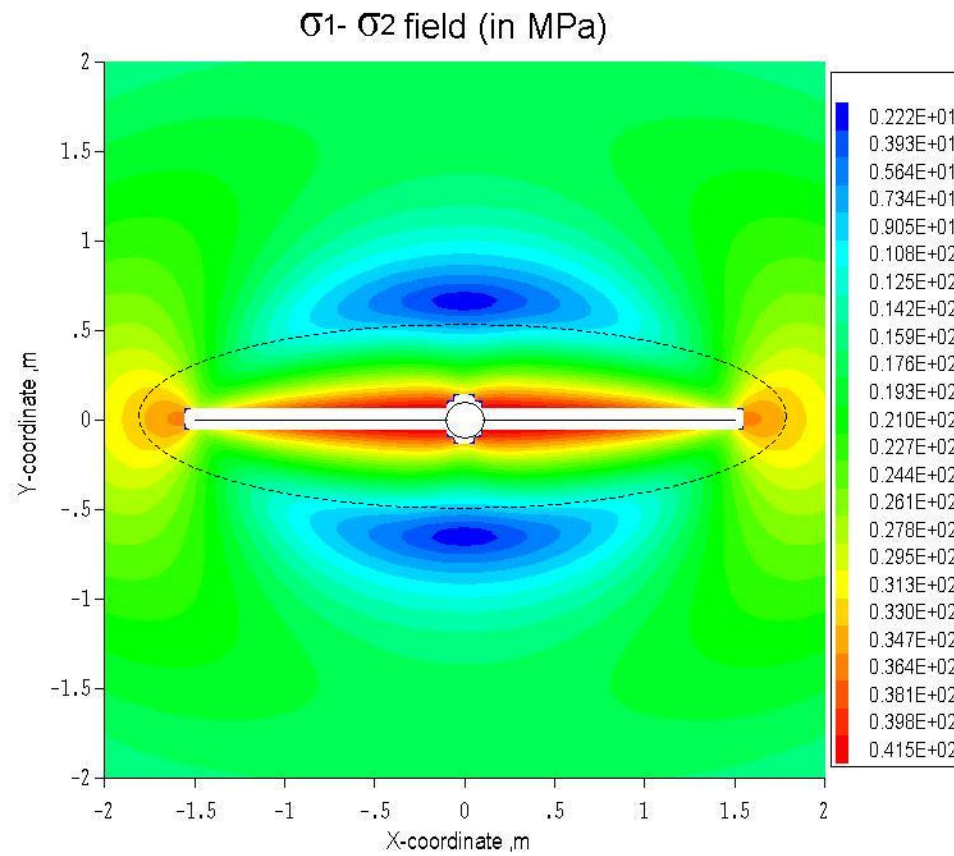


Figure 50. Difference between thermal induced principle stresses around an injection well with a long fracture



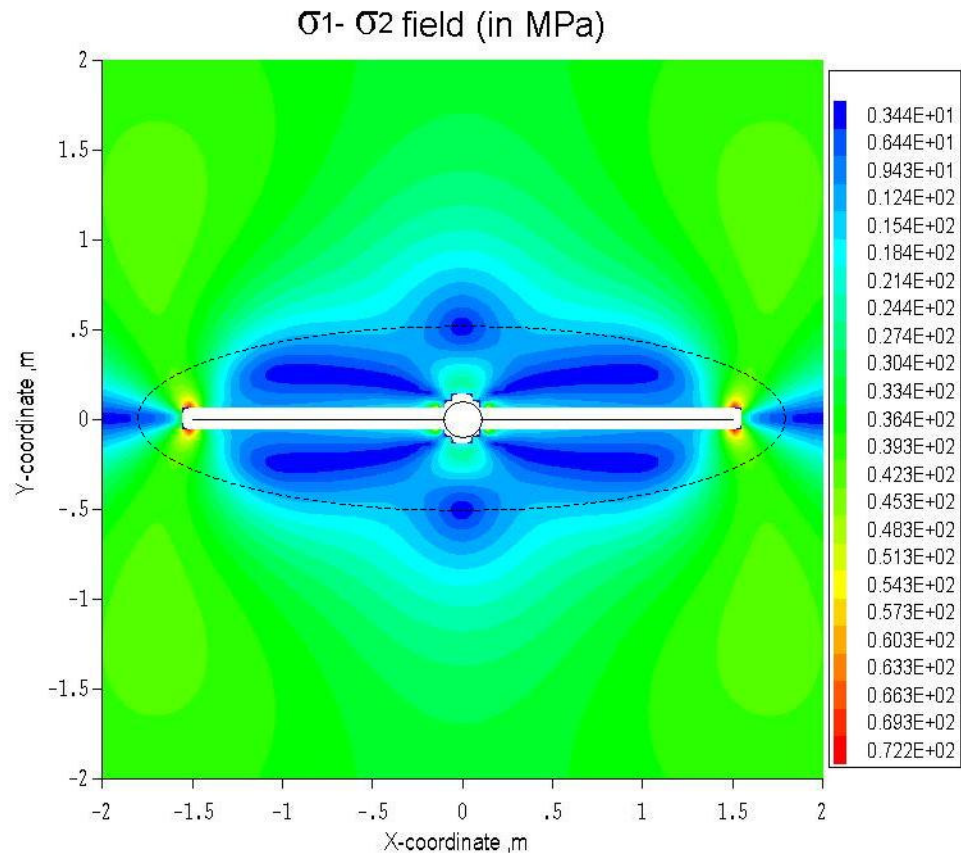


Figure 51. Difference between total principle stresses around an injection well and a short fracture

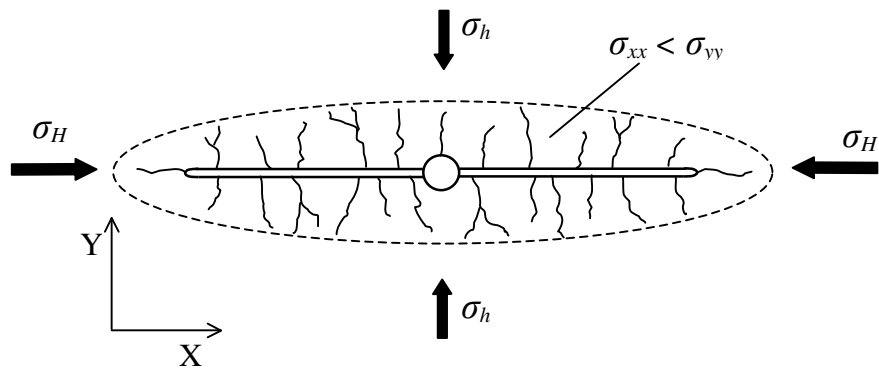


Figure 52. Formation of secondary fractures within cooled region

### Maximum Crack Opening under Poro-thermo-mechanical Loading

The opening of a crack under combined poro-thermo-mechanical loading is considered in this section. To examine the effects of cooling and hydraulic injection, three different solutions are given to this problem, which are thermoelastic, poroelastic and thermo-poroelastic.

Assume crack length is 2.0 m. The in-situ major and minor stresses and pore pressure are 41.4 MPa, 20.7 MPa and 1.7 MPa, respectively. The crack is perpendicular to the direction of the minor principle stress. Normal stress and pressure applied caused by the injection fluid on the crack surface are 19.9 MPa and 19.9 MPa, respectively. Formation temperature is 200°C, while the crack is suddenly cooled to 0°C. The crack is modeled by 39 displacement discontinuity elements.

Figure 53 shows the maximum opening of the crack as time increases. The poroelastic solution predicts the crack will “close” with time under a pore pressure loading, that is the width of the crack opening becomes negative. This is because the diffusion of the injection fluid into the porous formation would increase the pore pressure around the crack; and the increased pore pressure would consequently induce a dilatation of the rock formation. In reality, it’s obvious this “closure” of the crack surfaces is physically impossible. The thermoelastic solution shows the crack will open up gradually as time increases. This is a result of the shrinking of the rock formation caused by cooling. The thermo-poroelastic solution illustrates the combined effects of hydraulic, thermal and mechanical loading. As can be seen, the crack also opens up with time, which implies the thermal effect dominates. Also note at any given time, the opening is

less than the one predicted in thermoelastic solution. The difference between them is caused by the closing effect of the hydraulic loading. This example also shows that the thermo-poroelastic solution will provide the most accurate estimate for crack opening in hydraulic fracturing process.

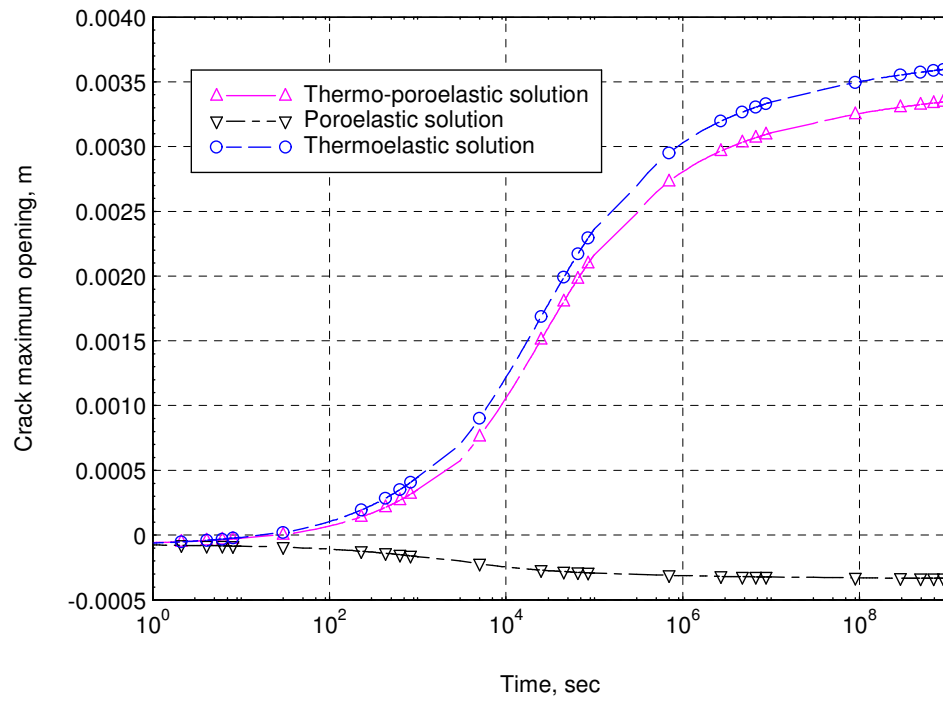


Figure 53. Maximum crack opening under poro-thermo-mechanical loading

## CHAPTER 6

### CONCLUSIONS AND FUTURE WORK

A two-dimensional transient indirect boundary element model has been developed to solve coupled thermo-poroelastic problems. The model is based on the thermo-poroelastic theory, which is developed from the fully coupled poroelastic theory extended to non-isothermal conditions. The model has been tested and verified using a variety of examples that have analytical solutions. A number of applications related to borehole stability and hydraulic fracturing were illustrated in the thesis. Stress and pore pressure fields around the examined borehole or crack were calculated by taking into account the poromechanical loading and thermal loading.

Two sub-formulations of the indirect BEM, both displacement discontinuity (DD) model and fictitious stress (FS) model were developed in order to treat different problems. The two models are combined in a mixed FS-DD model to examine the interactions of underground opening and fractures under thermo-hydro-mechanical loading. A graphic user interface (GUI) with functions like data input and visualization was developed and integrated with the numerical FS-DD model. Contour mapping of temperature field, pore pressure field and stress field in studied area is available.

Borehole under non-hydrostatic stress loading was studied using the fully coupled poroelastic FS model. As expected, the result shows that fluid injection results in a time

dependent compressive stress zone around the borehole, while draining creates a tangential stress zone (total stress). Under deviatoric stress loading, a radial gradient of the pore pressure forms at early times, which is triggered by the rapid drainage. This pressure peak decays with time, and moves away from the borehole wall. It was found that at the instant of drilling, the peak of the tangential stress occurs inside the rock instead of the borehole wall, as predicted by the elastic analysis.

The impact of thermal effect on borehole stability was analyzed using the FS model. It has been shown that cooling reduces pore pressure around the borehole. A tensile stress zone develops because of the shrinkage of the rock material. Cooling increases the potential of fracturing because of the existence of the tangential tensile stress based on a traditional strength approach. The fracture will be initiated from the borehole wall because the maximum tensile stress always occurs there. The tensile stress zone formed inside the formation with time will encourage the time-delayed fracture development. These results agree with analytical solutions.

Crack behaviors under poroelastic loading and thermal loading were studied. Crack openings and stress intensity factors were calculated using the DD model. Cooling the crack will increase the opening and stress intensity factor, which implies higher potential of fracture propagation. Draining in the crack from the formation has the same effect. The results show good agreement with analytical solutions.

Two examples were used to verify the combined FS-DD model in analyzing the interaction of borehole and pre-existing cracks. Tangential stresses for field points around

the hole, and the stress intensity factors for the cracks were calculated for the borehole-crack system. The results also agree very well with other published solutions.

The influence of borehole ellipticity on stability has been examined while considering thermal and hydraulic effects. Effective hoop stresses for circular and elliptical boreholes are compared. It has been found that in certain cases an elliptical borehole will be more likely to fail in tension due to the pressure of the mud column and cooling. Hence a mud with a higher temperature and/or lower density than that for a circular well need be used.

Another example showed how cooling the borehole wall encourages tensile failure when drilling in high temperature formations. The effective tangential stress field around the borehole shows that large tensile stresses are induced on the opposite sides of borehole wall at the azimuth of major in-situ stress. Therefore, tensile fractures are very likely to occur in the borehole wall when the effective tangential stress exceeds the tensile strength of the rock. In addition, a tensile radial stress zone inside the formation encourages tensile fracturing in the circumferential direction.

The effect of thermoelastic stresses on the injection well fracturing was also analyzed. It has been found that cooling can reduce the stresses around the well substantially, causing it to fracture at much lower pressure. A cooled region around the well with an initial short fracture is found to be near circular. As the fracture grows, the cooled region elongates. Thermal induced stresses will reduce the difference of the original in-situ principle stresses presented in the formation. As a result, when the total

stress parallel to the fracture becomes less than the stress cross the fracture, secondary fractures perpendicular to the main fracture could form.

Finally, the maximum opening of a crack under combined poro-thermo-mechanical loading has been examined. It has been shown that the crack is more likely to grow under cooling because of the contraction of the formation; while the pore pressure loading due to injecting water in the crack would have a “closure” effect. This example also shows that the thermo-poroelastic solution will provide the most accurate estimate for crack opening in long-term simulation of geothermal reservoirs.

The applications mentioned above indicate that coupled thermal and poromechanical processes play an important role in borehole stability analysis and hydraulic fracturing in high temperature formations. The stress and pore pressure fields in the formation are significantly altered during borehole drilling or hydraulic fracturing. Thermal effect is found to be much more significant than hydraulic effect in some cases.

The boundary element model presented in this thesis has proven suitable for the coupled thermo-poroelastic problems in borehole drilling and hydraulic fracturing. Interactions between borehole and pre-existing cracks can be analyzed using the combined FS-DD model.

For the future work, it is recommended that the model be improved in the following respects: 1. In the current model, hydraulic boundary condition is limited to known pressures, fluid flux should be added in the boundary condition options to study impermeable boreholes; 2. Heat flux should be considered as a thermal boundary condition in addition to temperature; 3. Tip elements should be added in the DD model in

order to get more accurate results around the crack tips; 4. Joint elements should be added in the DD model to better simulate the behavior of discontinuities; 5. Node-centric method should be adopted in the DD model to better estimate the tangential stresses.



## APPENDICES

## Appendix A

### Two-dimensional Fundamental Solutions for a Continuous Heat Source in Thermo-poroelastic Problems

Fundamental solutions (Green functions) corresponding to a continuous heat source can be derived by the integral transform (e.g. Smith and Booker 1993) technique. Laplace transform with respect to time and Fourier or Hankel transforms with respect to the spatial domain are commonly used. Another approach is based on dimensional analysis and self-similarity, which has more obvious physical meanings. The second approach is used by Berchenko (1998) to derive the fundamental solutions for continuous heat source in thermo-poroelastic media; and is briefly described below.

Suppose  $\Lambda$  is the strength of a continuous heat source in [Watt/m<sup>2</sup>],  $q^T$  is the heat flux in [°C · m/sec]. Relationship of  $\Lambda$  and  $q^T$  is:

$$\Lambda = q^T \rho C \quad (A1)$$

where  $\rho$  is the density and  $C$  is the heat capacity.

The volumetric strain  $\varepsilon$  in thermo-poroelasticity can be obtained:

$$\varepsilon = \frac{3\alpha}{3K + 4G} \left( p + \frac{\beta_s K}{\alpha} T \right) \quad (A2)$$

Substituting the above expression into the diffusion equation for pore pressure in equation (14) results in:

$$c^f \nabla^2 p = \frac{\partial p}{\partial t} - \frac{\beta_0}{S} \frac{\partial T}{\partial t} \quad (\text{A3})$$

where  $c^f$  is fluid diffusivity, given by  $c^f = \frac{k}{\mu S}$ . Parameter  $S$  is a storage coefficient given

by  $S = \frac{1}{M} + \frac{3\alpha^2}{3K + 4G}$ . And  $\beta_0$  is given by  $\beta_0 = \beta_m - \frac{3\alpha\beta_s K}{3K + 4G}$ . Definition of  $\beta_m$  can be

found in Chapter 2.

Equation (20) can be written in cylindrical system of coordinates as:

$$\frac{c^f}{r} \frac{\partial}{\partial r} \left( r \frac{\partial p}{\partial r} \right) = \frac{\partial p}{\partial t} - \frac{\beta_0}{S} \frac{\partial T}{\partial t} \quad (\text{A4})$$

where  $r$  is the distance between the influenced point (the point of interest) and the influencing point (where the singular source located).  $r$  is defined by  $r^2 = x_1^2 + x_2^2$  in two-dimensional co-ordinates system.

Thermal diffusion equation (12) can also be written in cylindrical system as:

$$\frac{c^T}{r} \frac{\partial}{\partial r} \left( r \frac{\partial T}{\partial r} \right) = \frac{\partial T}{\partial t} \quad (\text{A5})$$

Together with the boundary conditions

$$\lim_{r \rightarrow 0} 2\pi r \frac{\partial T}{\partial r} = -\frac{q^T}{K^T}, \quad \lim_{r \rightarrow \infty} T = 0 \quad (\text{A6})$$

$$\lim_{r \rightarrow 0} p \neq \infty, \quad \lim_{r \rightarrow \infty} p = 0 \quad (\text{A7})$$

Then, the solution to (A5) is given by:

$$T = \frac{\Lambda}{\kappa^T} \Phi(\xi^2) \quad (\text{A8})$$

The latter is used in (A4) to find:

$$p = \frac{\beta_0}{S} \frac{\Lambda}{\kappa^T} \Psi(\xi^2; \omega^2) \quad (\text{A9})$$

where  $\xi^2$  is called a self-similar variable written as:

$$\xi^2 = \frac{r^2}{4c^T t} \quad (\text{A10})$$

and  $\omega^2$  is the ratio of hydraulic diffusivity to thermal diffusivity,  $\omega^2 = c^f/c^T$ .

Substituting equation (A8) and (A9) into equation (A4) and (A5) yields:

$$\frac{d}{d\xi^2} \left( \xi^2 \frac{d\Phi}{d\xi^2} \right) = -\xi^2 \frac{d\Phi}{d\xi^2} \quad (\text{A11})$$

$$\omega^2 \frac{d}{d\xi^2} \left( \xi^2 \frac{d\Psi}{d\xi^2} \right) = -\xi^2 \frac{d}{d\xi^2} (\Psi - \Phi) \quad (\text{A12})$$

These two equations can be integrated to get the final expression for singular solutions for the temperature and the pore pressure induced by a continuous point heat source of unit strength:

$$T^{ch} = \frac{T}{\Lambda} = \frac{1}{4\pi\kappa^T} \text{Ei}(\xi^2) \quad (\text{A13})$$

$$p^{ch} = \frac{p}{\Lambda} = \frac{\beta_0}{4\pi\kappa^T S(1-\omega^2)} \left[ \text{Ei}(\xi^2) - \text{Ei}\left(\frac{\xi^2}{\omega^2}\right) \right] \quad \omega^2 \neq 1 \quad (\text{A14})$$

$$p^{ch} = \frac{p}{\Lambda} = \frac{\beta_0}{4\pi\kappa^T S} e^{-\xi^2} \quad \omega^2 = 1 \quad (\text{A15})$$

According to Berchenko (1998), the singular solution for stress field can be obtained from equation (3), (A2), (A13), (A14) and (A15):

$$\sigma_{ij}^{ch} = \frac{\sigma_{ij}}{\Lambda} = \frac{\eta\beta_0}{4\pi\kappa^T S(1-\omega^2)} \left[ \lambda F(x_i, x_j, \xi^2) - F\left(x_i, x_j, \frac{\xi^2}{\omega^2}\right) \right] \quad \omega^2 \neq 1 \quad (\text{A16})$$

$$\sigma_{ij}^{ch} = \frac{\sigma_{ij}}{\Lambda} = \Lambda \frac{\eta\beta_0}{4\pi\kappa^T S} [\lambda_1 F(x_i, x_j, \xi^2) - F_1(x_i, x_j, \xi^2)] \quad \omega^2 = 1 \quad (\text{A17})$$

In the above equations, Ei is exponential integral function, which is defined as:

$$\text{Ei}(u) = \int_u^\infty \frac{e^{-z}}{z} dz \quad (\text{A18})$$

Function F and F<sub>1</sub> are given by:

$$F(x_i, x_j, \xi^2) = \left( \delta_{ij} - \frac{2x_i x_j}{r^2} \right) \left[ \frac{1 - e^{-\xi^2}}{\xi^2} \right] - \delta_{ij} \text{Ei}(\xi^2) \quad (\text{A19})$$

$$F_1(x_i, x_j, \xi^2) = - \left( \delta_{ij} - \frac{2x_i x_j}{r^2} \right) \left[ \frac{1 - e^{-\xi^2}}{\xi^2} \right] - 2 \left( \delta_{ij} - \frac{x_i x_j}{r^2} \right) e^{-\xi^2} \quad (\text{A20})$$

Constants  $\lambda_1$  is given by  $\lambda_1 = \frac{K\beta_s S}{\alpha\beta_0}$ , while  $\lambda = 1 + (1 - \omega^2)\lambda_1$ .

The spatial integration of the fundamental solutions for a continuous point heat source over a straight-line element of length  $2a$  yields:

$$T = \frac{1}{4\pi\kappa^T} \int_{-a}^a \text{Ei}(\xi^2) dx' \quad (\text{A21})$$

For  $\omega^2 \neq 1$

$$p = \frac{\beta_0}{4\pi\kappa^T S(1-\omega^2)} \left[ \int_{-a}^a \text{Ei}(\xi^2) dx' - \int_{-a}^a \text{Ei}(\xi^2 / \omega^2) dx' \right] \quad (\text{A22})$$

$$\begin{aligned}\sigma_{xx} = & C_1 \lambda \left\{ \left[ - (x - x') \frac{(1 - e^{-\xi^2})}{\xi^2} - (x - x') \text{Ei}(\xi^2) \right]_{-a}^a - 2 \int_{-a}^a \text{Ei}(\xi^2) dx' \right\} \\ & - C_1 \left\{ \left[ - (x - x') \frac{(1 - e^{-\xi^2/\omega^2})}{\xi^2/\omega^2} - (x - x') \text{Ei}(\xi^2/\omega^2) \right]_{-a}^a - 2 \int_{-a}^a \text{Ei}(\xi^2/\omega^2) dx' \right\}\end{aligned}\quad (\text{A23})$$

$$\begin{aligned}\sigma_{yy} = & C_1 \lambda \left[ (x - x') \frac{(1 - e^{-\xi^2})}{\xi^2} + (x - x') \text{Ei}(\xi^2) \right]_{-a}^a \\ & - C_1 \left[ (x - x') \frac{(1 - e^{-\xi^2/\omega^2})}{\xi^2/\omega^2} + (x - x') \text{Ei}(\xi^2/\omega^2) \right]_{-a}^a\end{aligned}\quad (\text{A24})$$

$$\begin{aligned}\sigma_{xy} = & -C_1 \lambda y \left[ \frac{(1 - e^{-\xi^2})}{\xi^2} + \text{Ei}(\xi^2) \right]_{-a}^a \\ & + C_1 y \left[ \frac{(1 - e^{-\xi^2/\omega^2})}{\xi^2/\omega^2} + \text{Ei}(\xi^2/\omega^2) \right]_{-a}^a\end{aligned}\quad (\text{A25})$$

For  $\omega^2 = 1$

$$p = \frac{\beta_0}{4\pi\mathbf{K}^T S} \int_{-a}^a \text{Ei}(\xi^2) dx' \quad (\text{A26})$$

$$\begin{aligned}\sigma_{xx} = & -C_2 (\lambda_1 + 1) \left[ (x - x') \frac{(1 - e^{-\xi^2})}{\xi^2} + (x - x') \text{Ei}(\xi^2) \right]_{-a}^a \\ & - C_2 (2\lambda_1 + 1) \int_{-a}^a \text{Ei}(\xi^2) dx' + C_2 y^2 \int_{-a}^a \frac{e^{-\xi^2}}{r^2} dx'\end{aligned}\quad (\text{A27})$$

$$\begin{aligned}
\sigma_{yy} = & C_2(\lambda_1 + 1) \left[ (x - x') \frac{(1 - e^{-\xi^2})}{\xi^2} + (x - x') \text{Ei}(\xi^2) \right]_{-a}^a \\
& + C_2 \int_{-a}^a \text{Ei}(\xi^2) dx' + C_2 \int_{-a}^a \frac{(x - x')^2 e^{-\xi^2}}{r^2} dx'
\end{aligned} \tag{A28}$$

$$\sigma_{xy} = -C_2(\lambda_1 + 1)y \left[ \frac{(1 - e^{-\xi^2})}{\xi^2} + \text{Ei}(\xi^2) \right]_{-a}^a - 2C_2y \int_{-a}^a \frac{(x - x')^2 e^{-\xi^2}}{r^2} dx' \tag{A29}$$

where:

$$C_1 = \frac{\eta\beta_0}{4\pi\kappa^T S(1 - \omega^2)}; \quad C_2 = \frac{\eta\beta_0}{4\pi\kappa^T S}; \quad \eta = \frac{\alpha(1 - 2\nu)}{2(1 - \nu)}$$

$$r^2 = (x - x')^2 + y^2; \quad \xi^2 = \frac{r^2}{4c^T t}$$

## Appendix B

### Derivation of the Long-term Crack Opening and Stress Intensity Factor under Pore Pressure Loading

The long-term effect on the fracture caused by a pore pressure loading has been studied by Detournay and Cheng (1991) using the following approach.

Consider a fracture of length  $2L$  subjected to hydraulic loading  $p$ . At large times, the pore pressure in the region surrounding the fracture reaches a constant value characterized by axial symmetry (Detournay and Cheng, 1991). In the absence of a fracture cut, this pore pressure would have induced an irrotational displacement field (Detournay and Cheng, 1991).

Navier equation for poroelasticity can be given as:

$$G\nabla^2 u_i + \frac{1}{3}(G + 3K)\varepsilon_{,i} = \alpha p_{,i} \quad (\text{B1})$$

Since volumetric strain  $\varepsilon = u_{k,k}$ , equation (B1) can also be written as:

$$G\nabla^2 u_i + \frac{1}{3}(G + 3K)u_{k,ki} = \alpha p_{,i} \quad (\text{B2})$$

Consider now the particular case of an irrotational displacement field. According to the Helmholtz decomposition of a vector field, the displacement can then be expressed as the gradient of a scalar potential  $\Psi$

$$u_i = \Psi_{,i} \quad (\text{B3})$$



Insert (B3) into (B2):

$$\left[ G + \frac{1}{3}(G + 3K) \right] \Psi_{,ikk} = \alpha p_{,i}$$

Considering  $\eta = \frac{\alpha(1-2\nu)}{2(1-\nu)}$ ,

$$\Psi_{,ikk} = \frac{\alpha(1-2\nu)}{2G(1-\nu)} p_{,i} = \frac{\eta}{G} p_{,i} \quad (\text{B4})$$

Integration of this equation yields:

$$u_{i,i} = \varepsilon = \frac{\eta}{G} p + g(t) \quad (\text{B5})$$

where  $g(t)$  is an unknown function of time that has to be determined from boundary conditions. For the infinite/semi-infinite domains,  $g(t)$  remains to be zero.

Now look at the stress-strain equation for poroelasticity:

$$\sigma_{ij} = 2G\varepsilon_{ij} + \frac{1}{3}(3K - 2G)\varepsilon\delta_{ij} - \alpha p\delta_{ij} \quad (\text{B6})$$

Contraction of equation (B6) leads to:

$$\sigma_{kk} = 2G\varepsilon_{kk} + \frac{2}{3}(3K - 2G)\varepsilon - 2\alpha p \quad (\text{B7})$$

Consider  $\varepsilon = \varepsilon_{kk}$ , equation (B7) becomes:

$$\sigma_{kk} = \frac{2G\varepsilon}{(1-2\nu)} - 2\alpha p \quad (\text{B8})$$

Introduce (B5) into equation (B8), and after some manipulation, we get the stress field related to long-term hydraulic loading:

$$\sigma_{kk} = -2\eta p \quad (\text{B9})$$

As  $t \rightarrow \infty$ , a uniform confining stress develops (Detournay and Cheng, 1991):

$$\begin{aligned}\sigma_{xx} + \sigma_{yy} &= -2\eta p \\ \sigma_{xx} &= \sigma_{yy} = -\eta p\end{aligned}\tag{B10}$$

Now consider the fracture ( $-L < x < L$ ) subjected to hydraulic loading on the surfaces, the long-term effect on the fracture opening caused by pore pressure rise  $p$  is equivalent to the application of a tensile stress  $\sigma_{yy} = -\eta p$  (Detournay and Cheng, 1991). The long-term opening can be calculated by the classic Sneddon's solution for pressurized fracture:

$$D_n = -\frac{2p_f L(1-\nu)}{G} \left(1 - \frac{x^2}{L^2}\right)\tag{B11}$$

where  $p_f$  represents the normal stress applied on the fracture surfaces.

Let  $p_f = \sigma_{yy} = -\eta p$ , the crack maximum opening for long-term hydraulic loading is:

$$(D_n)_{\max} = -\frac{2\eta L(1+\nu)}{G} p\tag{B12}$$

The expression of stress intensity factor of a pressurized fracture ( $-L < x < L$ ) can be found in Detournay and Cheng's work (1991):

$$K_1 = p_f \sqrt{\pi L}\tag{B13}$$

Let  $p_f = \sigma_{yy} = -\eta p$ , the crack stress intensity factor for long-term hydraulic loading is:

$$K_1(\infty) = -\eta p \sqrt{\pi L}\tag{B14}$$

## Appendix C

### Derivation of the Long-term Crack Opening and Stress Intensity Factor under Thermal Loading

This appendix considers the long-term effect of temperature change on the fracture width and SIF. The problem of a fracture of length  $2l$  subjected to thermal loading  $T$ , can be studied using the same approach used for poroelasticity. At large times, the temperature in the region surrounding the fracture reaches a constant value characterized by axial symmetry. In the absence of a fracture cut, this temperature would have induced an irrotational displacement field.

Navier equation for thermoelasticity can be obtained by taking off the pore pressure term in thermo-poroelasticity, and then can be given as:

$$G\nabla^2 u_i + \frac{1}{3}(G + 3K)\epsilon_{,i} = K\beta_s T_{,i} \quad (C1)$$

Since volumetric strain  $\epsilon = u_{k,k}$ , equation (C1) can also be written as:

$$G\nabla^2 u_i + \frac{1}{3}(G + 3K)u_{k,ki} = K\beta_s T_{,i} \quad (C2)$$

In the particular case of an irrotational displacement field, according to the Helmholtz decomposition of a vector field, the displacement can then be expressed as the gradient of a scalar potential  $\Psi$  (Detournay and Cheng, 1993)

$$u_i = \Psi_{,i} \quad (C3)$$

Insert (C3) into (C2):

$$\left[ G + \frac{1}{3}(G + 3K) \right] \Psi_{,ikk} = K\beta_s T_{,i}$$

Consider  $G = \frac{E}{2(1+\nu)}$ , and  $K = \frac{E}{3(1-2\nu)}$ , it gives:

$$\Psi_{,ikk} = \frac{(1+\nu)\beta_s}{3(1-\nu)} T_{,i} \quad (C4)$$

Integration of this equation yields:

$$u_{i,i} = \varepsilon = \frac{(1+\nu)\beta_s}{3(1-\nu)} T + h(t) \quad (C5)$$

where  $h(t)$  is an unknown function of time that has to be determined from boundary conditions. For the infinite/semi-infinite domains,  $h(t)$  remains to be zero.

Now look at the stress-strain equation for thermoelasticity:

$$\sigma_{ij} = 2G\varepsilon_{ij} + \frac{1}{3}(3K - 2G)\varepsilon\delta_{ij} - K\beta_s T\delta_{ij} \quad (C6)$$

Contraction of equation (C6) leads to:

$$\sigma_{kk} = 2G\varepsilon_{kk} + \frac{2}{3}(3K - 2G)\varepsilon - 2K\beta_s T \quad (C7)$$

Consider  $\varepsilon = \varepsilon_{kk}$ , equation (C7) becomes:

$$\sigma_{kk} = \frac{2G\varepsilon}{(1-2\nu)} - 2K\beta_s T \quad (C8)$$

Introduce (C5) into equation (C8), and after some manipulation, we get the stress field related to long-term thermal loading:

$$\sigma_{kk} = -\frac{E\beta_s}{3(1-\nu)}T \quad (C9)$$

As  $t \rightarrow \infty$ , a uniform confining stress develops:

$$\begin{aligned} \sigma_{xx} + \sigma_{yy} &= -\frac{E\beta_s}{3(1-\nu)}T \\ \sigma_{xx} = \sigma_{yy} &= -\frac{E\beta_s}{6(1-\nu)}T \end{aligned} \quad (C10)$$

Now consider the fracture ( $-L < x < L$ ) subjected to thermal loading on the surfaces, the long-term effect on the fracture opening caused by temperature change  $T$  is equivalent to the application of a tensile stress  $\sigma_{yy} = -\frac{E\beta_s}{6(1-\nu)}T$ . The long-term opening can be calculated by the classic Sneddon's solution for pressurized fracture:

$$D_n = -\frac{2p_f L(1-\nu)}{G} \left( 1 - \frac{x^2}{L^2} \right) \quad (C11)$$

where  $p_f$  represents the normal stress applied on the fracture surfaces.

Let  $p_f = \sigma_{yy} = -\frac{E\beta_s}{6(1-\nu)}T$ , the crack maximum opening for long-term thermal

loading is:

$$(D_n)_{\max} = -\frac{2\beta_s L(1+\nu)}{3}T \quad (C12)$$

The expression of stress intensity factor of a pressurized fracture ( $-L < x < L$ ) can be found in Detournay and Cheng's work (1991):

$$K_1 = p_f \sqrt{\pi L} \quad (\text{C13})$$

Let  $p_f = \sigma_{yy} = -\frac{E\beta_s}{6(1-\nu)}T$ , the crack stress intensity factor for long-term thermal

loading is:

$$K_1(\infty) = -\frac{E\beta_s}{6(1-\nu)}\Delta T \sqrt{\pi L} \quad (\text{C14})$$

## Appendix D

### Two-dimensional Fundamental Solutions for a Unit Continuous Fluid Source in a Poroelastic Medium

The two-dimensional fundamental solutions for pore pressure and stresses induced by a unit continuous fluid source in poroelasticity are given by (Cheng and Detournay, 1998):

$$p^{cs} = \frac{1}{4\pi c^f} Ei(\xi^2) \quad (D1)$$

$$\sigma_{ij}^{cs} = \frac{\alpha(1-2\nu)}{8\pi c^f(1-\nu)} \left\{ \left( \delta_{ij} - \frac{2x_i x_j}{r^2} \right) \frac{1}{\xi^2} (1 - e^{-\xi^2}) - \delta_{ij} Ei(\xi^2) \right\} \quad (D2)$$

where  $r^2 = x^2 + y^2$ ;  $\xi^2 = \frac{r^2}{4c^f t}$ . It should be noted that in this thesis the strength of the

continuous point fluid source is defined by  $\phi^c = \frac{c^f \mu}{k} \delta(\mathbf{x} - \boldsymbol{\chi}) H(t - \tau)$ , where  $H(x)$  is the

Heaviside function. The fundamental solutions listed in Cheng and Detournay's (1998)

are in different forms because they define the strength of the continuous point source as

$$\phi^c = \delta(\mathbf{x} - \boldsymbol{\chi}) H(t - \tau).$$

The spatial integration of the above fundamental solutions for a continuous point fluid source over a straight-line element of length  $2a$  yields:

$$p = \frac{1}{4\pi c^f} \int_{-a}^a Ei(\xi^2) dx' \quad (D3)$$

$$\sigma_{xx} = \frac{\alpha(1-2\nu)}{8\pi c^f(1-\nu)} \left\{ \left[ - (x-x') \frac{(1-e^{-\xi^2})}{\xi^2} - (x-x') \text{Ei}(\xi^2) \right]_{-a}^a - 2 \int_{-a}^a \text{Ei}(\xi^2) dx' \right\} \quad (\text{D4})$$

$$\sigma_{yy} = \frac{\alpha(1-2\nu)}{8\pi c^f(1-\nu)} \left[ (x-x') \frac{(1-e^{-\xi^2})}{\xi^2} + (x-x') \text{Ei}(\xi^2) \right]_{-a}^a \quad (\text{D5})$$

$$\sigma_{xy} = \frac{\alpha(1-2\nu)}{8\pi c^f(1-\nu)} \left[ -y \frac{(1-e^{-\xi^2})}{\xi^2} - y \text{Ei}(\xi^2) \right]_{-a}^a \quad (\text{D6})$$

where  $r^2 = (x-x')^2 + y^2$ ;  $\xi^2 = \frac{r^2}{4c^f t}$ .



Appendix E  
Two-dimensional Fundamental Solutions for a Unit Continuous Heat Source  
in a Thermoelastic Medium

The two-dimensional fundamental solutions for temperature and stresses induced by a continuous heat source in thermoelasticity are given by (Berchenko, 1998):

$$T^{ch} = \frac{1}{4\pi\kappa^T} \text{Ei}(\xi^2) \quad (\text{E1})$$

$$\sigma_{ij}^{cs} = \frac{G\beta_s(1+\nu)}{12\pi\kappa^T(1-\nu)} \left\{ \left( \delta_{ij} - \frac{2x_i x_j}{r^2} \right) \frac{1}{\xi^2} (1 - e^{-\xi^2}) - \delta_{ij} \text{Ei}(\xi^2) \right\} \quad (\text{E2})$$

where  $r^2 = x^2 + y^2$ ;  $\xi^2 = \frac{r^2}{4c^T t}$ . The strength of the continuous point heat source is defined by  $\varphi^c = \delta(\mathbf{x} - \boldsymbol{\chi})H(t - \tau)$ .

The spatial integration of the above fundamental solutions for a continuous point heat source over a straight-line element of length  $2a$  yields:

$$T = \frac{1}{4\pi\kappa^T} \int_{-a}^a \text{Ei}(\xi^2) dx' \quad (\text{E3})$$

$$\sigma_{xx} = \frac{G\beta_s(1+\nu)}{12\pi\kappa^T(1-\nu)} \left\{ \left[ - (x - x') \frac{(1 - e^{-\xi^2})}{\xi^2} - (x - x') \text{Ei}(\xi^2) \right]_{-a}^a - 2 \int_{-a}^a \text{Ei}(\xi^2) dx' \right\} \quad (\text{E4})$$

$$\sigma_{yy} = \frac{G\beta_s(1+\nu)}{12\pi\kappa^T(1-\nu)} \left[ (x - x') \frac{(1 - e^{-\xi^2})}{\xi^2} + (x - x') \text{Ei}(\xi^2) \right]_{-a}^a \quad (\text{E5})$$

$$\sigma_{xy} = \frac{G\beta_s(1+\nu)}{12\pi\kappa^T(1-\nu)} \left[ -y \frac{(1-e^{-\xi^2})}{\xi^2} - y \operatorname{Ei}(\xi^2) \right]_{-a}^a \quad (\text{E6})$$

where  $r^2 = (x-x')^2 + y^2$ ;  $\xi^2 = \frac{r^2}{4c^T t}$ .

## NOMENCLATURE

$u_i$	[m]	Displacement
$\varepsilon_{ij}$		Solid strain
$\sigma_{ij}$	[MPa]	Total stress
$K_I$	[MPa·m <sup>1/2</sup> ]	Stress intensity factor
$p$	[MPa]	Pore pressure
$q$	[m/sec]	Fluid flux
$T$	[°C]	Temperature
$q^T$	[°C·m/sec]	Heat flux
$\phi$	[Pa·m/sec]	Continuous fluid source strength density
$\varphi$	[Watt·m <sup>2</sup> ]	Continuous heat source strength density
$G$	[MPa]	Shear modulus
$E$	[MPa]	Modulus of elasticity
$M$	[MPa]	Biot modulus
$\nu$		Poisson's ratio
$\nu_u$		Undrained Poisson's ratio
$\zeta$		Fluid content variation per unit volume
$K$	[MPa]	Rock bulk modulus
$K_s$	[MPa]	Solid bulk modulus
$K_f$	[MPa]	Fluid bulk modulus
$c^f$	[m <sup>2</sup> /sec]	Fluid diffusivity
$c^T$	[m <sup>2</sup> /sec]	Thermal diffusivity
$C$	[Joule/(kg·°C)]	Heat capacity
$\alpha$		Biot's coefficient
$\beta_s$	[1/°C]	Solid volumetric thermal expansion coefficient
$\beta_f$	[1/°C]	Fluid volumetric thermal expansion coefficient
$n$		Porosity
$\gamma_f$	[N/m <sup>3</sup> ]	Unit weight of fluid

$\kappa^T$	[Watt/(m·°C)]	Thermal conductivity
$k$	[darcy]	Intrinsic permeability
$B$		Skempton's constant
$\mu$	[Pa·sec]	Fluid dynamic viscosity

## REFERENCES CITED

- Aadnoy, B.S., and Angell-Olsen, F., 1995. "Some Effects of Ellipticity on the Fracturing and Collapse Behavior of a Borehole", *International Journal of Rock Mechanics and Mining Science*, vol. 32, no. 6, pp. 621-627
- Aadnoy, B.S., and Chenevert, M.E., 1987. "Stability of Highly Inclined Boreholes", *SPE/IADC Drilling Conference*, New Orleans, LA, Mar. 15-18, SPE paper no. 16052
- Aadnoy, B.S., and Ong, S., 2003. "Editorial: Introduction to Special Issue on Borehole Stability", *Journal of Petroleum Science and Engineering*, vol. 38, pp. 79-82
- Atkinson, C., and Thiercelin, M., 1995. "The Interaction between the Wellbore and Pre-existing Fractures", *International Journal of Fracture*, vol. 73, pp. 183-200
- Atkinson, C., and Thiercelin, M., 1997. "Pressurization of a Fractured Wellbore", *International Journal of Fracture*, vol. 83, pp. 243-273
- Banerjee, P.K., Butterfield, R., 1981. *Boundary element methods in engineering science*, McGraw-Hill, London, 512p
- Berchenko, I., 1998. "Thermal Loading of Saturated Rock Mass: Field Experiment and Modeling Using Thermoporoelastic Singular Solutions", Ph.D. Dissertation, University of Minnesota
- Biot, M.A., 1941. "General Theory of Three-dimensional Consolidation", *Journal of Applied Physics*, vol. 12, pp. 155-164
- Bradley, W.B., 1979. "Failure of Inclined Boreholes", *ASME Journal of Energy Resources Technology*, vol. 101, pp. 232-239
- Brebbia, C.A., Telles, J.C.F., and Wrobel, L.C., 1984. *Boundary Element Techniques: Theory and Applications in Engineering*, Springer-Verlag, Berlin, 464p
- Carslaw, H.S., and Jaeger, J.C., 1956. *Conduction of Heat in Solids*, 2<sup>nd</sup> edition, Oxford University Press, London, 510p

- Cheng, A.H.-D., 1998. "On Generalized Plane Strain Poroelasticity", *International Journal of Rock Mechanics and Mining Science*, vol. 35, no. 2, pp. 183-193
- Cheng, A.H.-D., and Detournay, E., 1988. "A Direct Boundary Element Method for Plane Strain Poroelasticity", *International Journal for Numerical and Analytical Methods in Geomechanics*, vol. 12, pp. 551-572
- Cheng, A.H.-D., and Detournay, E., 1998. "On Singular Integral Equations and Fundamental Solutions of Poroelasticity", *International Journal of Solids and Structures*, vol. 35, pp. 4521-4555
- Cheng, A.H.-D., Ghassemi, A., and Detournay, E., 2001. "A Two-dimensional Solution for Heat Extraction from a Fracture in Hot Dry Rock", *International Journal for Numerical and Analytical Methods in Geomechanics*, vol. 25, pp. 1327-1338
- Coussy, O., 1991. "Thermoporoelastic response of a borehole", *Transport in Porous Media*, vol. 21, pp. 121-146
- Crouch, S.L., and Starfield, A.M., 1983. *Boundary Element Methods in Solid Mechanics*. George Allen and Unwin, London, 322p
- Cui, L., Abousleiman, Y., Cheng, A.H.-D., Roegiers, J.-C., and Leshchinsky, D., 1995. "Stability Analysis of an Inclined Borehole in an Isotropic Poroelastic Medium", in J.J.K. Daemen and R. Shultz (eds) *Proceeding of the 35th US Symposium on Rock Mechanics*, pp. 307-312
- Cui, L., Cheng, A.H.-D., and Abousleiman, Y., 1997. "Poroelastic Solution of an Inclined Borehole", *ASME Journal of Applied Mechanics*, vol. 64, pp. 32-38
- Cui, L., Ekbote, S., Abousleiman, Y., Zaman, M., and Roegiers, J.-C., 1998. "Borehole Stability Analysis in Fluid Saturated Formations with Impermeable Walls", *International Journal of Rock Mechanics and Mining Science*, vol. 35, no. 4-5, Paper No. 061
- Curran, J.H., Carvalho, J.L., 1987. "A Displacement Discontinuity Model for Fluid-saturated Porous Media", *Proceeding of the 6th Congress of the ISRM*, vol. 1, pp. 73-78
- Delaney, P.T., 1982. "Rapid Intrusion of Magma into Wet Rock: Groundwater Flow Due to Pore Pressure Increases", *Journal of Geophysics Research*, vol. 87, no. B9, pp. 7739-7756

- Detournay, E., and Cheng, A.H.-D., 1988. "Poroelastic Response of a Borehole in a Non-hydrostatic Stress Field", *International Journal of Rock Mechanics and Mining Science and Geomechanics Abstracts*, vol. 25, no. 3., pp. 171–182
- Detournay, E., and Cheng, A.H.-D., 1991. "Plane Strain Analysis of a Stationary Hydraulic Fracture in a Poroelastic Medium", *International Journal of Solids and Structures*, vol. 27, no. 13, pp. 1645–1662
- Detournay, E., and Cheng, A.H.-D., 1993. "Fundamentals of Poroelasticity", in J.A. Hudson (ed) *Comprehensive Rock Engineering: Principles, Practices, and Projects*, vol. 2, pp. 113-171
- Geertsma, J., 1957. "The Effect of Fluid Pressure Decline on the Volumetric Changes of Porous Rocks", *Journal of Applied Mechanics*, vol. 24, pp. 594-601
- Ghassemi, A., Cheng, A.H.-D., Diek, A., and Roegiers, J.-C., 2001. "A Complete Plane-strain Fictitious Stress Boundary Element Method for Poroelastic Media", *Journal of Engineering Analysis with Boundary Elements*, vol. 25, no. 1, pp. 41-48
- Ghassemi, A., and Diek, A., 2002. "Poro-thermoelasticity for Swelling Shales", *Journal of Petroleum Science and Engineering*, vol. 34, pp. 123-135
- Ghassemi, A., and Zhang, Q., 2004. "A Transient Fictitious Stress Boundary Element Method for Poro-thermoelastic Media", *Journal of Engineering Analysis with Boundary Elements* (in press)
- Hsiao, C. 1987. "A Study of Horizontal-Wellbore Failure", 62<sup>nd</sup> *Annual Technical Conference and Exhibition*, SPE, Dallas, TX, Sept. 27-30, *SPE* paper no. 16927
- Jaeger, J. C., and Cook, N.G.W., 1979. *Fundamentals of Rock Mechanics*, 3<sup>rd</sup> edition, Chapman and Hall, New York, 593p
- Kurashige, M., 1989. "A Thermoelastic Theory of Fluid-filled Porous Materials", *International Journal of Solids and Structures*, vol. 25, no. 9, pp. 1039–1052
- Li, X., Cui, L., and Roegiers, J.-C., 1998. "Thermoporoelastic Modeling of Wellbore stability in Non-hydrostatic Stress Field", *International Journal of Rock Mechanics and Mining Science*, vol. 35, nos. 4-5, Paper no. 063
- McTigue, D.F., 1986. "Thermoelastic Response of Fluid-saturated Porous Rock", *Journal Geophysics Research*, vol. 91, no. B9, pp. 9533-9542
- Norris, A.N., 1992. "On the Correspondence Between Poroelasticity and Thermoelasticity", *Journal of Applied Physics*, vol. 71, pp. 1138-1141

- Palciauskas, V.V., and Domenico, P.A., 1982. "Characterization of Drained and Undrained Response of Thermally Loaded Repository Rocks", *Water Resources Research*, vol.18, pp. 281-290
- Perkins, T.K., and Gonzalez, J.A., 1985. "The Effect of Thermoelastic Stresses on Injection Well Fracturing", *SPE Journal*, February, pp. 78-88
- Prasad, N.N.V., Aliabadi, M.H., and Rooke, D.P., 1996. "The Dual Boundary Element Method for Transient Thermoelastic Crack Problem", *International Journal for Solids & Structures*, vol. 33, no. 19, pp.2695-2718
- Rice, J.R., and Cleary, M.P., 1976. "Some Basic Stress-diffusion Solutions for fluid Saturated Elastic Media with Compressible Constituents", *Reviews of Geophysics and Space Physics*, vol. 14, pp. 227-241
- Sheridan J., Kovac K., Rose P., Barton C., McCulloch J., Berard B., Moore J., Petty S., and Spielman. P., 2003. "In Situ Stress, Fracture and Fluid Flow Analysis-East Flank of the Coso Geothermal Field", *28th Stanford Geothermal Workshop*, California
- Sih, G.C., Paris, P.C., and Erdogan, F., 1962. "Crack-tip Stress Intensity Factors for Plane Extension and Plane Bending Problems", *Journal of Applied Mechanics*, vol. 29, pp. 306–312
- Sih, G.C., 1973. *Handbook of Stress Intensity Factors*, Lehigh University, Bethlehem, PA
- Smith, D.W., and Booker, J.R., 1993. "Green's Functions for a Fully Coupled Thermoporoelastic Material", *International Journal for Numerical and Analytical Methods in Geomechanics*, vol. 17, pp. 139-163
- Timoshenko, S., and Goodier, J.N., 1951., *Theory of Elasticity*, 2<sup>nd</sup> edition, McGraw-Hill, New York, 506p
- Vandamme, L., Detournay, E., and Cheng, A.H.-D., 1989. "A Two-dimensional Poroelastic Displacement Discontinuity Method for Hydraulic Fracture Simulation", *International Journal for Numerical and Analytical Methods in Geomechanics*, vol. 13, pp. 215-224
- Vijayakumar, S., Curran, J.H., and Hammah, R.E., 2003. "Developing Start-of-the-art Displacement Discontinuity Code", in P.J. Culligan et.al. (eds) *Proceeding of the 39th US Symposium on Rock Mechanics*, pp.1117-1123



- Wang, Y., and Papamichos, E., 1994. "Conductive Heat Flow and Thermally Induced Fluid Flow around a Well Bore in a Poroelastic Medium", *Water Resources Research*, vol. 30, no. 12, pp. 3375-3384.
- Wolfe, C.A., 2002. "Borehole Stability in Shale", Master's thesis, University of North Dakota